MEMS-based tunable Fabry-Perot filters for multispectral thermal imaging applications

Haifeng Mao

B. Eng. (DUT, China), M. Sc. (HsKA, Germany)

This thesis is presented for the degree of Doctor of Philosophy of
The University of Western Australia

The University of Western Australia

School of Electrical, Electronic and Computer Engineering

2016

Abstract

A highly desirable feature of state-of-the-art infrared imaging systems is multispectral capability, which allows on-pixel information to be collected from multiple discrete wavelength bands. The spectral information can be used to extract spectral signatures of objects, thus allowing discrimination and identification of targets that are indistinguishable using intensity information alone. In conventional multispectral infrared imagers, spectral band selection is realized based on bulk optics, and their size and cost prevent the wide adoption of the technology in many desirable applications. Micro-electromechanical systems (MEMS) based tunable Fabry-Perot filters, on the other hand, provide a miniature optical filter solution. Fabry-Perot filters consist of a top mirror suspended over a fixed bottom mirror, and optical resonance within the cavity enables the transmission of a narrow wavelength band from a broadband incident spectrum. Micro-electromechanical actuators are employed in such devices to move the top mirror and change the optical cavity length, resulting in tunability of the transmitted wavelengths. Conceptually, a large-area MEMS-based Fabry-Perot filter could be hybridized with a two-dimensional imaging focal plane array (FPA) to create the next-generation of compact multispectral infrared imaging systems.

The motivation for this thesis is target identification for both civilian and military applications, including mineral mapping, volatile organic compounds diagnosis, and buried landmine detection. This requires on-pixel spectral information to be collected over the long-wavelength infrared (LWIR) thermal imaging band of 8–12 µm, with a peak transmittance higher than 50%, a spectral pass-band width between 0.5 µm and 1 µm, an out-of-band rejection greater than 10:1, and a pixel-to-pixel transmission peak wavelength variation of less than 4%. Whilst MEMS-based tunable LWIR Fabry-Perot filters have been reported, these published

works concentrate on achieving high spectral resolution (narrow pass-band width) by incorporating highly reflective multilayer Bragg mirrors. Successful development of these filters is technologically challenging due to the stress-mismatch induced bowing of suspended mirrors compounded by the need for significant stress control mechanisms.

This thesis focuses on the design, fabrication and characterization of MEMS-based LWIR Fabry-Perot filters, which rely on a single-layer suspended top mirror to negate stress-mismatch induced mirror deformation. The LWIR Fabry-Perot filters presented in this work consist of a single-layer quarter-wavelength thick Ge top mirror and a four-layer quarter-wave Ge/ZnS/Ge/ZnS bottom mirror on a silicon substrate. Optical modelling indicates that the ideal filters can achieve >80% peak transmittance with a full-width at half-maximum (FWHM) of approximately 500 nm and an out-of-band rejection >40:1 over the entire 8–12 µm wavelength range, all of which exceed the target spectral specifications for multispectral thermal imaging applications.

In this work, we first present a MEMS-based LWIR Fabry-Perot filter with a circular Ge top mirror suspended in the center of four doubly clamped beam actuators by flexible tethers. Due to the stress gradient inherent in the Ge mirror layer, the fabricated 150-µm diameter filter initially exhibited a significant top mirror bowing of 1.5 µm. A SiN_x stress-compensation layer was used to balance the stress gradient in the suspended top mirror for mirror bowing control. Run-to-run processing variations only allowed partial correction of mirror bowing, and the smallest mirror bowing achieved after stress compensation was 550 nm. Optical modelling showed that although this filter can achieve ideal on-pixel transmittance characteristics that exceed the target spectral specifications for multispectral thermal imaging applications, including a peak transmittance higher than 80%, a FWHM of approximately 500 nm, and an out-of-band rejection better than 40:1, it suffers from a significant pixel-to-pixel transmission peak wavelength variation of 6.9% across the entire 150-µm diameter mirror and, thus, for the required <4% peak wavelength variability, has a small usable optical imaging area within the central region of only 46% of the total mirror area. This filter shows promise for use in multispectral thermal imaging applications; however, it presents many challenges for this filter technology to

realize large-area tunable filters that are necessary for hybridizing with FPAs, and processing variations need to be under better control before such a filter technology can be fully realized.

This thesis then presents a MEMS-based tunable LWIR Fabry-Perot filter based on an improved structural design, which employs a self-supporting tensile Ge membrane as both the suspended top mirror and the MEMS actuator support. It has been demonstrated that this filter design is insensitive to mirror layer stress gradients and run-to-run processing variations, and can achieve nanometre-scale as-released top mirror flatness across a large mirror area of millimeter-scale dimensions without any additional stress management. The fabricated filter with a 200-µm dimension mirror demonstrated <100 nm top mirror bowing during actuation and exhibited close-to-design transmittance characteristics (including a peak transmittance between 80–87%, a FWHM of approximately 500 nm, and an out-of-band rejection between 40:1 and 43.5:1) over the entire wavelength tuning range of 8.5–11.46 µm. Moreover, optical modelling showed that this filter can achieve a pixel-to-pixel transmission peak wavelength variation of less than 1.2% across the entire 200 µm × 200 µm optical mirror area. All these spectral parameters exceed the target spectral specifications for multispectral thermal imaging applications. In comparison, the 500-µm and 1000-µm dimension filters developed significant top mirror bowing during actuation and, as a result, despite showing ideal on-pixel transmittance over the entire actuation range, have narrower usable spectral tuning ranges of 9.3-11.4 µm and 10.3-11.3 µm, respectively, for a pixel-to-pixel transmission peak wavelength non-uniformity of <4%. In addition, cryogenic cooling tests showed that the static filters can maintain excellent suspended mirror flatness even after cooling to 77 K. Overall, we anticipate the work presented in this thesis to be a good starting point for the future development of miniature multispectral thermal imaging systems based on a hybridized technology incorporating a large-area MEMS-based tunable LWIR Fabry-Perot filter and a cryogenically cooled 2-D LWIR imaging focal plane array.

Acknowledgements

I would like to express my gratitude to my supervisors Prof. Dilusha Silva, Prof. Mariusz Martyniuk, Prof. Lorenzo Faraone, and Prof. John Dell for providing me with the opportunity to work on this interesting and rewarding project. I am especially indebted to Dilusha, Mariusz and Lorenzo, not only for their academic input and guidance for the project, but also for their encouragement and support throughout my study.

Prof. Jarek Antoszewski, Prof. Adrian Keating, Dr. John Bumgarner and Dr. Gino Putrino, who have been consistently attending group meeting on every Friday morning, deserve great thanks for sharing their knowledge and technical expertise with me, your discussions and suggestions always stimulate me to think deep and wide.

I would like to thank all my fellow postgraduates for making my stay in Australia very pleasurable. I enjoyed working with you and cherish the friendship from you all. I am also grateful to Sabine Betts and Karen Kader for their constant support, patience, and assistance with administrative matters.

I wish to express my thanks to the staff of the Electronic and General Workshops at the School of Electrical, Electronic and Computer Engineering, and in particular to George Voyt and Jonathan Brant. In addition, I would like to thank Australian Research Council (ARC) for funding this project and also the support from the Western Australian Node of the Australian National Fabrication Facility (ANFF) and the Western Australian State Government Office of Science.

I give my greatest gratitude to my parents for their everlasting support during all my time spent at educational institutions. Your contributions are invaluable. Finally to my wife Yihui, your support, understanding and encouragement over the years have given me strength to tackle challenges on my way to chasing my dream, especially during the hard times.

Statement of Originality

The work contained in this thesis is, to the best of the author's knowledge, original and contains no material previously published by another person except where due references are made. The material in this thesis has not been previously submitted, in part or in full, for a degree at this or any other higher education institution.

Haifeng Mao

Contents

List of Figures

List of Tables

Chapter 1

Introduction

This chapter introduces multispectral thermal imaging and its use in target recognition applications, and outlines the practical challenges encountered by conventional multispectral thermal imaging systems based on standard bulk optics. Subsequently, it presents a brief introduction to the micro-electromechanical systems (MEMS) technology and the basic operation of a Fabry-Perot filter, and describes how these technologies can be used to develop miniature optical filters for next-generation compact multispectral thermal imaging systems. The chapter closes by detailing the thesis structure.

1.1 Multispectral thermal imaging technology

Spectral imaging systems produce images in which each pixel contains spectrally discriminated information of the incident light. Generally, multispectral imaging systems resolve a scene into less than 20 spectral bands, with each band being several hundred nanometers to several microns wide, although there is no consensus on exact values. Vivid examples of multispectral imaging systems are human eyes and digital cameras that see objects in three discrete visible bands: red, green and blue. Spectral imaging systems that collect narrower and more numerous bands (at least 100 spectral bands of 10-20 nm width) are referred to as hyperspectral imaging systems, which are not the focus of this thesis.

Multispectral imaging systems are widely used in target recognition applications. This approach introduces the concept of spectral signature, as illustrated in Figure 1.1, where materials reflect or emit electromagnetic radiation with wavelength-dependent features inherent to the physical structure and chemical composition of the materials. If the reflectance or emissivity for a given material is plotted across a range of wavelengths, the resulting curve is referred to as the spectral signature

for that material. Because the spectral signature is indeed unique for each material, it is possible to discriminate between one material and another based on spectral measurements. An airborne or spaceborne multispectral imaging sensor captures site images at a number of discrete wavelength bands and uses the obtained multispectral images to extract reflectance or emissivity spectrum for every pixel in the image of a scene. By comparing the measured reflectance or emissivity spectrum at each pixel with those in a reference library of known material spectra, the specific materials in the observation site can be spectrally identified and spatially mapped.

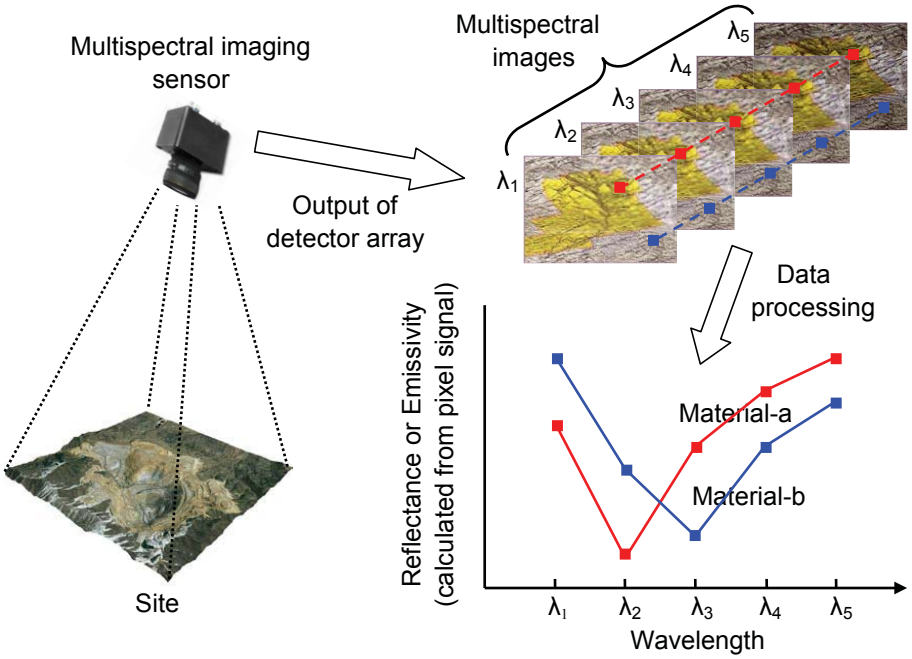

Figure 1.1: The concept of multispectral imaging technology.

Multispectral thermal imaging systems operate in the long-wavelength infrared (LWIR) range between 8 µm and 12 µm. The LWIR band contains electromagnetic radiation emitted from objects at close to room temperature in the form of heat. Therefore, this spectral region is also known as the "thermal imaging region", in which multispectral thermal imaging sensors can obtain completely passive images of objects based on thermal emissions only without requiring external illumination. This region is the spectral region of maximum thermal emission from a body at 300 K; it is also an atmospheric transmission window with no water absorption, and significantly less smoke/fog scattering takes place in this band. Thus, the LWIR band is ideal for remote sensing applications. Because most rock-forming minerals and organic chemical vapors have their strongest spectral emissivity features in the 8-12 µm range, multispectral thermal imaging systems are widely used for rock-forming minerals mapping [1, 2] and organic chemical gas detection [3, 4, 5]. For

example, Kahle et al. [1] employed a multispectral thermal imaging system with six wavelength bands, i.e., 8.2–8.6, 8.6–9.0, 9.0–9.4, 9.4–10.2, 10.2–11.2 and 11.2–12.2 µm, to map the extent of silicate rocks in the California-Nevada border area. Wabomba et al. [3] utilized a multispectral thermal imaging system with a set of 0.5-1 µm wide LWIR spectral bands, to monitor the methanol plume released from a chemical manufacturing facility. In addition, multispectral thermal imaging systems have also found applications in global atmospheric temperature profile monitoring [6, 7] and buried landmine detection [8].

There are many different types of devices for spectral selection [9], such as dispersive grating/prism, Fourier transform spectrometers, circular and linear variable filters, and acousto-optical tunable filters. These filter systems have the advantage of providing very high spectral resolution in the order of several tens of nanometers that fulfills the requirement for hyperspectral imaging, but they are expensive filter solutions for multispectral thermal imaging where such narrow spectral width is not essentially needed. In conventional multispectral thermal imaging systems, spectral band selectivity is usually realized using a motorized filter wheel, where each slot in the wheel is equipped with an optical broadband-pass filter. Although this approach is simple and relatively cheap, it is still characterized by high mechanical complexity, significant size, and poor portability. For example, the thermal infrared multispectral scanner (TIMS) used by Kahle et al. for mapping silicate minerals weighed $\sim$ 200 kg [10]. Moreover, in conventional filter-wheel-based multispectral thermal imaging systems, the number of usable wavelength bands is limited by the number of slots available in the filter wheel, and the slow mechanical switching speed of the filter wheel gives rise to slow spectral switching speed and hence slow imaging rate. All these disadvantages prohibit the widespread use of multispectral thermal imaging technology in many desirable applications. Micro-electromechanical systems (MEMS) technology and Fabry-Perot filter technology provide a path to the realization of compact, low-cost and high-performance multispectral thermal imaging systems for applications beyond the reach of conventional instrumentation.

1.2 Micro-electromechanical systems (MEMS)

A micro-electromechanical system (MEMS) is a miniaturization technology, where techniques adapted from the semiconductor industry are used to fabricate devices on a scale of microns to millimeters that employ electromechanical elements, to sense, control and actuate on the micron scale, and generate effects on the macro scale. MEMS with its batch fabrication techniques enables components and devices

to be manufactured with the obvious advantages of reduced size, weight and cost, potentially making conventional technologies obsolete. MEMS-based gyroscopes [11], for example, have completely replaced all prior technologies for gyro sensors in the automotive industry. With the aid of MEMS miniaturization, conventional technologies have found applications never before envisaged. For example, the gyro sensors that were originally developed for automotive and aerospace applications, when fabricated on the MEMS scale, are now commonplace in consumer electronics, such as in digital cameras for motion stability control. Besides gyro sensors, other fields of technology transformed by MEMS include accelerometers [12], pressure sensors [13], and microphones [14].

In addition, miniaturization afforded by MEMS technology allows the production of devices with improved performance and new functionality that are simply not achievable with conventional macro-scale devices. Figure 1.2 shows an optical MEMS switch demonstrated at Sandia National Laboratories [15], which uses a polysilicon micromirror to steer a light beam by adjusting the mirror's angular displacement with an electrical stimulus. This micromirror has a fast switching speed on the order of several hundred nanoseconds, making it appealing for high-speed telecommunications and quantum computing applications. It is difficult to conceive how this functionality could have been realized without MEMS technology.

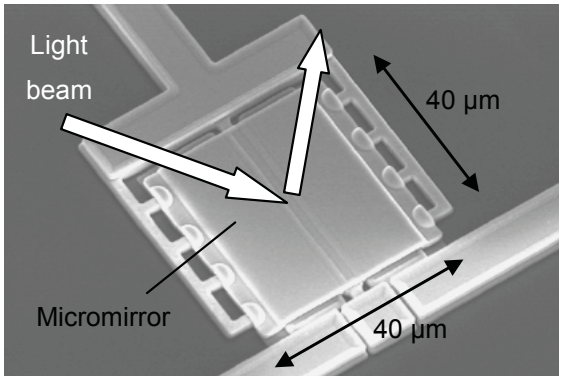

Figure 1.2: Optical MEMS switch developed at Sandia National Laboratories [15], with a fast switching speed of less than one microsecond. The image is taken from Reference [15].

A MEMS-based Fabry-Perot optical filter is an example of a MEMS device that has the potential to both replace existing technology and provide functionality beyond the reach of traditional instrumentation. These devices typically consist of a miniature mirror suspended over a fixed mirror, creating a resonant optical cavity that transmits a range of wavelengths determined by the mirror properties and the cavity length. MEMS actuators are used to move the suspended mirror and

change the optical cavity length, causing the transmitted wavelengths to sweep over a spectral range. MEMS-based Fabry-Perot filters are already being incorporated into commercially available solutions for telecommunications [16] and gas sensing [17]. Currently, these devices are widely replacing traditional spectroscopic systems in applications where cost and portability are of critical importance [18].

MEMS-based Fabry-Perot filters can provide increased performance and functionality that is difficult or expensive to achieve with macro-scale filter systems. One such proposed application for MEMS-based Fabry-Perot filters in multispectral imaging is shown in Figure 1.3, where an array of MEMS-based Fabry-Perot filters is hybridized with an array of HgCdTe (mercury cadmium telluride, MCT) infrared detectors to create a two-dimensional wavelength-tunable imaging focal plane array (FPA) [19]. Detector pixels typically have a pitch size of several tens of micrometers, and individual MEMS filter elements are on the size scale of several hundreds micrometers, covering a sub-array of detector pixels. More preferably, a single large-area multi-millimeter scale MEMS-based Fabry-Perot filter would be hybridized with the entire imaging FPA, rather than employing a filter array. Multispectral imaging systems based on MEMS tunable Fabry-Perot filters are far more compact and less costly than conventional filter-wheel-based systems. In addition, the number of spectral bands in MEMS Fabry-Perot filters based imaging systems is not limited by considerations such as the number of slots available in a filter wheel and, moreover, MEMS filters provide a faster spectral switching speed. These features significantly improve the multispectral data acquisition capability.

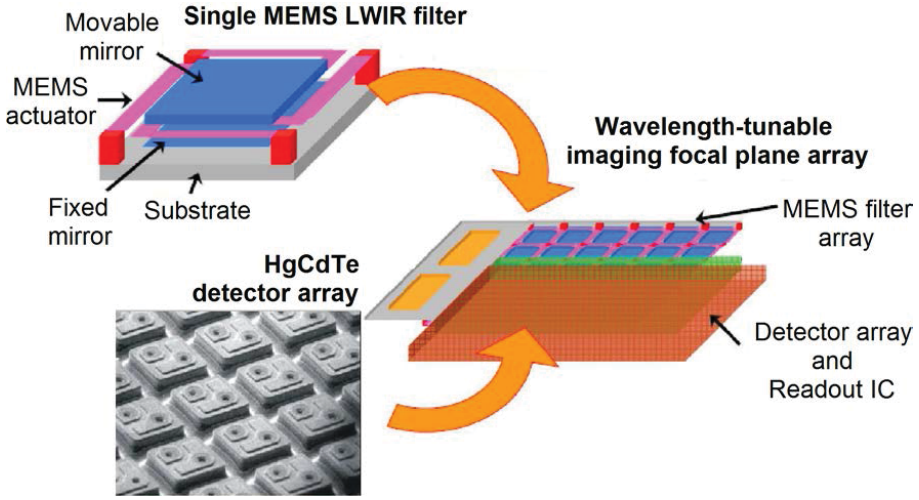

Figure 1.3: Next-generation miniature multispectral thermal imaging systems consist of an array of MEMS-based tunable LWIR Fabry-Perot filters (or a single large-area multi-millimeter scale MEMS-based LWIR Fabry-Perot filter) hybridized with an array of HgCdTe infrared detectors. The image is taken from Reference [19].

1.3 Basic operation of Fabry-Perot filters

Fabry-Perot filters typically consist of a pair of mirrors separated by a distance to form an optical cavity. The mirrors are usually Bragg reflectors composed of multiple layers of materials with alternating high and low refractive index. Ideal mirrors are non-absorbing, completely smooth, perfectly parallel and free of curvature. However, in reality, multi-layer Bragg mirrors may exhibit imperfections which can degrade filter transmission, and will also change the phase of the incident light as it is reflected. These considerations will be left to Chapter 3 when we discuss the optical design of MEMS-based LWIR Fabry-Perot filters. In the absence of mirror imperfections and mirror reflection phase changes, the wavelength dependence of the transmission of a Fabry-Perot filter can be easily visualized, as depicted in Figure 1.4.

Incident light undergoes multiple reflections between the two mirrors, transmitting some of the light for every round trip. Whenever there is zero round-trip phase change between the transmitted light, constructive interference produces a transmission peak. This occurs when the round-trip optical path length is an integral

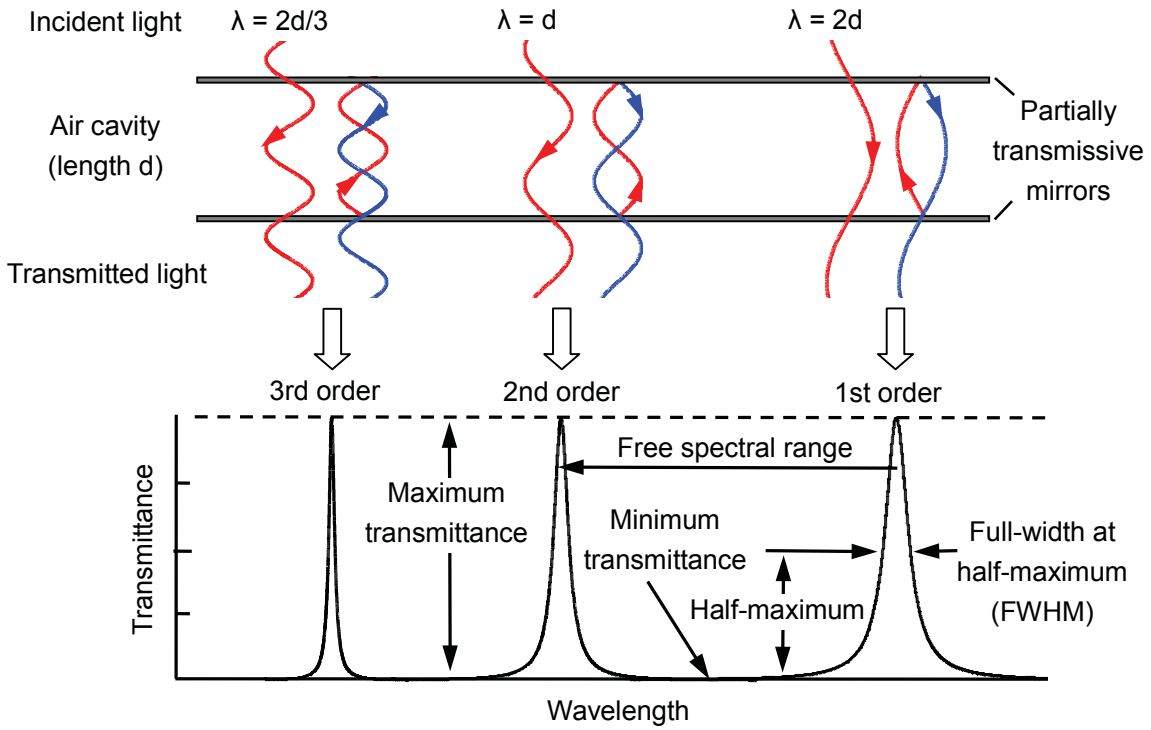

Figure 1.4: Illustration of the transmittance spectrum of an ideal Fabry-Perot filter, showing how wavelengths that resonate within the cavity are transmitted. For convenience of illustration, only the first reflections from the mirrors are drawn (secondary multiple reflections are ignored).

number of wavelengths, i.e., when

$$2d = m\lambda, \tag{1.1}$$

where d is the length of the air cavity, and m is an integer, termed the order of transmission peak. At other wavelengths, transmitted light is out of phase and destructive interference causes the filter transmittance to fall off rapidly away from the peak value, overall creating a spectrally isolated transmission pass-band.

A MEMS actuator can be used to change the mirror separation and hence tune the wavelength of the transmitted light, creating a wavelength tunable filter. For practical operation of a MEMS-based tunable Fabry-Perot filter, only one narrow band of wavelengths should be measured at any one time and unwanted orders must be removed from the detected spectrum. This is typically realized using another fixed bandpass "order-sorting" filter. The consequence of this requirement is that the maximum usable wavelength tuning range of a MEMS-based Fabry-Perot filter is limited to the initial wavelength separation between orders, which is termed the "free spectral range", as illustrated in Figure 1.4. MEMS-based tunable Fabry-Perot filters exhibit an inherent trade-off between the free spectral range and the spectral resolution. A MEMS-based Fabry-Perot filter can achieve a high spectral resolution by operating in a high order, but this reduces the free spectral range and ultimately the wavelength tuning range. A wide wavelength tuning range can potentially be achieved by operating the Fabry-Perot filter in a low order, but the spectral resolution will become inferior. Therefore, filter operating order is one of the most critical design decisions for the optical design of a tunable Fabry-Perot filter. We will come back to this point in Chapter 3 when we discuss the optical design of MEMS-based LWIR Fabry-Perot filters. It is important to acknowledge that operating in low order does not guarantee a wide wavelength tuning range, because with MEMS-based Fabry-Perot filters, the actual wavelength tuning range is limited by the distance over which the MEMS actuator can reliably control the mirror separation.

The critical spectral characteristics of a MEMS-based Fabry-Perot filter are the wavelength tuning range, the peak transmittance, the full-width at half-maximum (FWHM) of the transmission peak, and the out-of-band rejection (ratio of transmittance maximum to minimum). While the general requirement of FWHM for multispectral thermal imaging is application dependent, which ranges from hundreds of nanometers to several micrometers [1, 2, 3, 4, 5], MEMS-based Fabry-Perot filters developed in this work are targeted to achieve FWHM of 0.5–1 µm that is suitable for most multispectral thermal imaging applications. Other target

Table 1.1: Target spectral specifications of MEMS-based tunable LWIR Fabry-Perot filters for multispectral thermal imaging applications.

Parameter	Value	Comment
Wavelength tuning range (within)	8–12 µm	Complete thermal imaging band
Peak transmittance	$> 50\%$	Optical throughput for high signal-to-noise ratio
FWHM	0.5-1 µm	Optical throughput and spectral feature discrimination
Out-of-band rejection	$> 10{:}1$	Wavelength discrimination
Pixel-to-pixel transmission peak wavelength variation across the filter	$< 4\%$	Pixel-to-pixel transmission peak wavelength uniformity across the 2-D FPA

filter spectral characteristics include a wavelength tuning range of 8–12 µm, a peak transmittance higher than 50%, and an out-of-band rejection better than 10:1. The 0.5–1 µm FWHM is required in order to discriminate the LWIR spectral signatures of different targets, and the specifications of $> 50\%$ peak transmission and $> 10{:}1$ out-of-band rejection are based on the requirements of high optical throughput and signal-to-noise ratio for infrared imaging detectors. In addition, 2-D imaging focal plane array applications require the fabricated MEMS-based LWIR Fabry-Perot filters to have a pixel-to-pixel transmission peak wavelength variation of less than 4%. The $< 4\%$ peak wavelength variation requirement is proposed to ensure that, even at 12 µm, the maximum peak wavelength difference between different imaging pixels is less than 480 nm, which is less than the filter spectral resolution of 500 nm. In other words, this ensures that all imaging pixels acquire the same spectral signature at the same time. All these metrics are summarized in Table 1.1.

1.4 Thesis overview

The main objective of the work presented in this thesis is to design, fabricate and demonstrate MEMS-based LWIR Fabry-Perot filters capable of fulfilling the demanding requirements of next-generation miniature multispectral thermal imaging systems. This thesis consists of 7 chapters, including this introductory chapter. A brief overview of the contents of other chapters is given below:

- Chapter 2 will present a comprehensive review of published MEMS-based LWIR Fabry-Perot filter technologies in terms of mirror structures, actuation technologies, technological challenges encounted in the fabrication of these filters, and the achieved spectral characteristics;

- Chapter 3 will discuss the principles of the Fabry-Perot filter, quarter-wave mirror and anti-reflection coating, and will employ the existing theory to guide the optical design of the MEMS-based LWIR Fabry-Perot filters presented in this thesis. In addition, this chapter will describe an optical modelling approach for calculating the transmittance of a Fabry-Perot filter in the presence of mirror imperfections such as bowing and tilt, and subsequently examine the influence of top mirror bowing on the optical performance of the LWIR Fabry-Perot filter design;

- Chapter 4 will present a detailed study of Ge and ZnS thin film materials that were used for the construction of quarter-wave mirrors in MEMS-based LWIR Fabry-Perot filters. After a description of thin film preparation, experimental procedures used for characterization of thin film optical and mechanical properties are described, and the measurement results are reported;

- Chapter 5 will present the initial attempt to fabricate MEMS-based LWIR Fabry-Perot filters. The key steps in the development of the fabrication process for MEMS-based LWIR Fabry-Perot filters are described, including an approach to reduce the bowing of the top suspended mirrors in fabricated devices. Subsequently, this chapter describes the static measurements of the fabricated filters, showing that the key challenge in the successful development of these devices was the uncontrollable large mirror bowing caused by run-to-run processing variations, which prevented fulfilment of the specifications of multispectral thermal imaging applications;

- Chapter 6 will present the fabrication of MEMS-based LWIR Fabry-Perot filters based on an improved structure design. Mechanical and optical characterizations of actuated filters of different sizes are presented, showing that the filters can achieve high-yielding near-perfect mirror flatness after release, and excellent spectral tuning performance which exceeds the target spectral specifications for multispectral themal imaging applications. This chapter will also present the cryogenic cooling tests for the fabricated filters for evaluation of compatibility with longwave infrared FPAs. The preliminary results are reported, showing that the suspended top mirrors can maintain excellent flatness even after cooling to liquid nitrogen temperature of 77 K;

- Chapter 7 will summarize the key results achieved in this work, and layout the future work path towards the realization of practical miniature multispectral thermal imaging systems.

Chapter 2

A review of MEMS-based LWIR Fabry-Perot filters

This chapter presents a comprehensive review of published MEMS-based tunable LWIR Fabry-Perot filter technologies, highlighting the mirror structures, the actuation technologies, the technological challenges faced in the fabrication of these filters, as well as the achieved spectral characteristics.

2.1 Surface-micromachined filters

Whilst MEMS-based IR Fabry-Perot filters have been previously reported, most of them are designed for the near-infrared, short-wavelength and mid-wavelength infrared ranges. A detailed review of these filters can be found in [34]. To date, there are only a few reports on MEMS-based tunable Fabry-Perot filters for long-wavelength infrared. These filters can be classified into two categories according to the manufacturing techniques: surface micromachining and bulk micromachining. Surface micromachining applies subsequent deposition and etch patterning steps of thin film layers on the substrate to build microstructures. At the end of the process, certain layers are removed in a sacrificial etching and the suspended structures are released from the substrate.

There is only one example of surface-micromachined MEMS-based LWIR Fabry-Perot filters identified in the literature. This device, developed by Tuohiniemi et al. [20, 21], is schematically depicted in Figure 2.1a. The mirrors in this filter are three-layer Si/air/Si distributed Bragg reflectors, which are freely suspended in air. The air gaps in the mirrors are incorporated with a matrix of solid anchor structures that connect the two Si layers and fix their distance. Air gaps forming the mirrors and optical cavity are fabricated by wet etching of SiO_2 sacrificial layers, and suspension of the bottom mirror is realized by deep reactive ion etching the substrate

back surface using SiO_2 as the etch stop. The through-substrate opening defines a 800-µm diameter optical aperture. In this filter, all Si layers are initially deposited in amorphous phase and later annealed at 950 °C into polycrystalline form. The crystallization changes the initially compressive film stress into tensile stress, which aids in flattening the suspended mirrors. This filter demonstrates excellent mirror flatness after release, with mirror bowing less than 20 nm over a 800-µm aperture area. A SEM image of the poly-Si/air/poly-Si mirror and an optical microscopic picture of the filter are shown in Figures 2.1b and 2.1c, respectively.

Electrostatic actuation is used to tune the filter. The poly-Si layers, next to the air cavity in both the top and bottom mirrors, are boron-ion implanted for electrical conductivity, and essentially serve as the electrodes. When a voltage is applied between these two layers, an attractive electrostatic force is produced to move the top mirror towards the bottom mirror.

Two different actuating structures (type A and B, in Figure 2.1a) have been demonstrated by Tuohiniemi et al. In type A, the actuation voltage is applied to the whole top poly-Si layer of the bottom mirror. This causes the entire top mirror to be attracted towards the bottom mirror and thus bend over the optical aperture area during actuation. In type B, the top poly-Si layer of the bottom mirror is cut (see G in Figure 2.1a). Only the portion located on the substrate outside the optical path serves as the actuation electrode, while the central portion is connected to the same ground potential as the bottom poly-Si layer of the top mirror via poly-Si vias and the bottom poly-Si layer. By such a configuration, only the edge of the top suspended mirror responds to the electrostatic force and deforms with actuation, while the tensile film stress keeps the center of the top mirror planar.

Filter transmission was measured for both designs at actuation. Type A was reported to have a wavelength tuning range of 7.6-10.1 µm with an actuation voltage of 20 V, and type B was reported to have a comparable wavelength tuning range of 7.2-10.1 µm, but with a higher actuation voltage of 27 V due to the smaller actuator-electrode area. Unactuated filters showed a peak transmittance of 60% and a FWHM bandwidth of 140 nm. For type A, the filter peak transmittance reduced to 40% and FWHM bandwidth increased to 200 nm with actuation as a result of top mirror bowing. In comparison, type B exhibited consistent spectral characteristics, namely a peak transmittance of 60% and a FWHM bandwidth of 140 nm over most of the wavelength tuning range, although an anomaly in transmission was observed between 9.0 µm and 9.5 µm with peak transmittance slightly reduced to 50% and FWHM broadened to 170 nm. In Tuohiniemi et al's work, the fabricated filters were predicted to have a high peak transmittance of 99.4% and a narrow FWHM

of 82 nm. However, such ideal transmission characteristics were not achieved. The origins of the transmission anomaly and non-ideality were speculated but not fully understood.

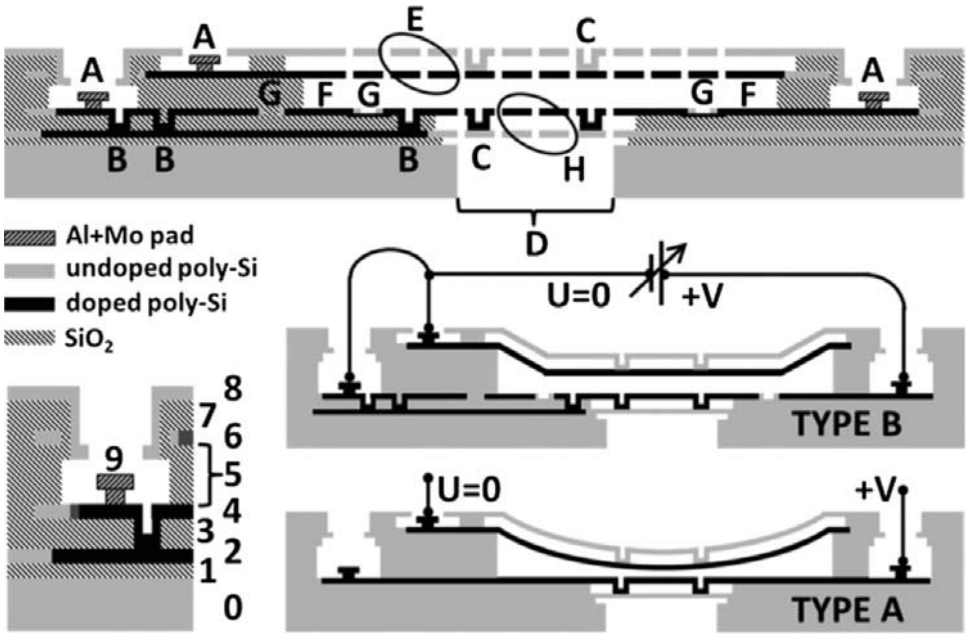

(a)

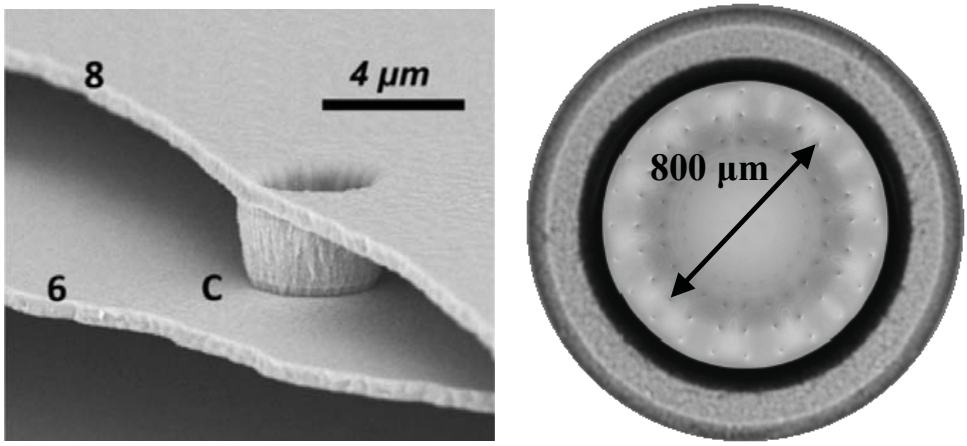

(b) (c)

Figure 2.1: (a) Schematic of a surface-micromachined MEMS-based LWIR Fabry-Perot filter developed by Tuohiniemi et al. [20, 21], showing two different actuator designs, (b) SEM micrograph of the poly-Si/air/poly-Si mirror, and (c) optical microscopic graph of the filter. For (a) and (b): 0, Si substrate; 1, substrate-isolation SiO_2; 2, poly-Si; 3, bottom mirror air-gap sacrificial SiO_2; 4, poly-Si; 5, air-cavity sacrificial SiO_2; 6, poly-Si; 7, top mirror air-gap sacrificial SiO_2; 8, poly-Si; 9, pad-metal; A, contact pads; B, poly-Si vias; C, intramirror anchors; D, aperture opening; E, top mirror; F, actuation electrode; G, isolation between electrode and grounded area; H, bottom mirror. The images are taken from Reference [20].

2.2 Bulk-micromachined filters

Unlike surface micromachining, which uses a succession of thin film deposition and selective etching to build microstructures, bulk micromachining defines structures by selectively etching a substrate. There are three bulk-micromachined MEMS-based LWIR Fabry-Perot filter technologies described in the literature.

Figure 2.2 shows a MEMS-based tunable LWIR Fabry-Perot filter developed by Stupar et al. [22]. This filter is a two-layer structure, comprised of a stationary Si mirror-supporting substrate and a movable Si mirror-supporting thin membrane. This filter is fabricated based on a silicon-on-insulator (SOI) device layer transfer process. Bragg mirrors (materials not disclosed) are separately deposited on a thick Si substrate and a SOI wafer, which are assembled by wafer bonding using a Au-Au thermocompression bond to form the optical cavity. Following the removal of the SOI handle wafer via wafer grinding, the silicon device layer is selectively etched to form the spring suspensions. Mechanical motion of the suspended mirror is achieved via electrostatic actuation by applying a voltage between the stationary and movable silicon mirror supports.

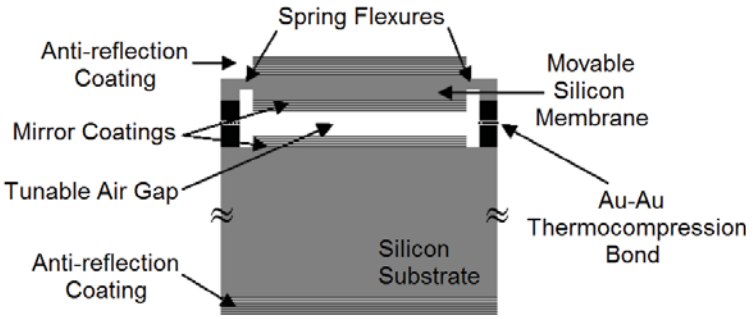

(a)

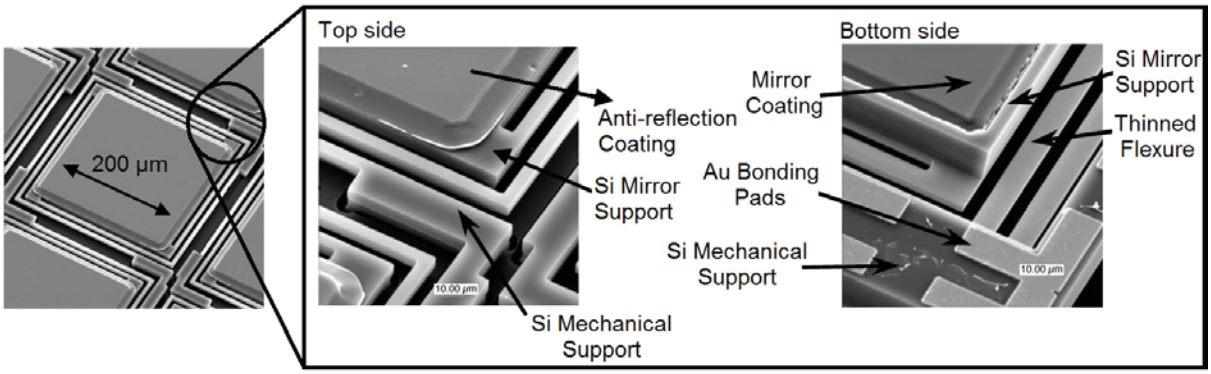

(b)

Figure 2.2: (a) Schematic of a bulk-micromachined MEMS-based LWIR Fabry-Perot filter developed by Stupar et al. [22], and (b) SEM micrograph of the filter. The images are taken from Reference [22].

In this filter, the multi-layer mirror coating is quite thick relative to the silicon device layer of the SOI wafer (13 µm thick coating on a 12 µm silicon membrane), and significant coating stress mismatch between the different mirror layers causes the thin suspended membrane to deform. This is further complicated by the mirror deformation caused by the thermal expansion mismatch between different mirror layers during cyrogenic operation required for long-wavelength infrared focal plane arrays. In order to obtain the desired mirror flatness after cooling to 77 K, the stress level of the multi-layer mirror coating is precisely controlled via tailoring the thin film deposition conditions to compensate for the thermal stress caused by cooling the filter. With the success of stress compensation, the center-to-edge mirror bowing of the filter is less than 10 nm across a 200 µm × 200 µm mirror area. Filter transmission was measured at liquid nitrogen temperature of 77 K. The filter was reported to have a wavelength tuning range of 8-11 µm with a peak transmittance of nearly 100% and a FWHM close to 120 nm.

Figure 2.3 shows another example of a bulk-micromachined MEMS-based tunable LWIR Fabry-Perot filter, which was developed by Ebermann et al. [23, 24]. This device uses 300 µm thick silicon wafers as carriers for both the fixed and movable mirrors, which are bonded together by an intermediate SU-8 layer to form the optical cavity. The mirrors are multi-layer Bragg reflectors made of Ge, ZnS and another material with a medium refractive index (not disclosed). The bottom mirror is located in the center of the substrate surrounded by the driving electrodes, while the top mirror is located in the center of the upper carrier wafer, which is suspended by diagonally arranged T-form springs located in the corners of the outer frame.

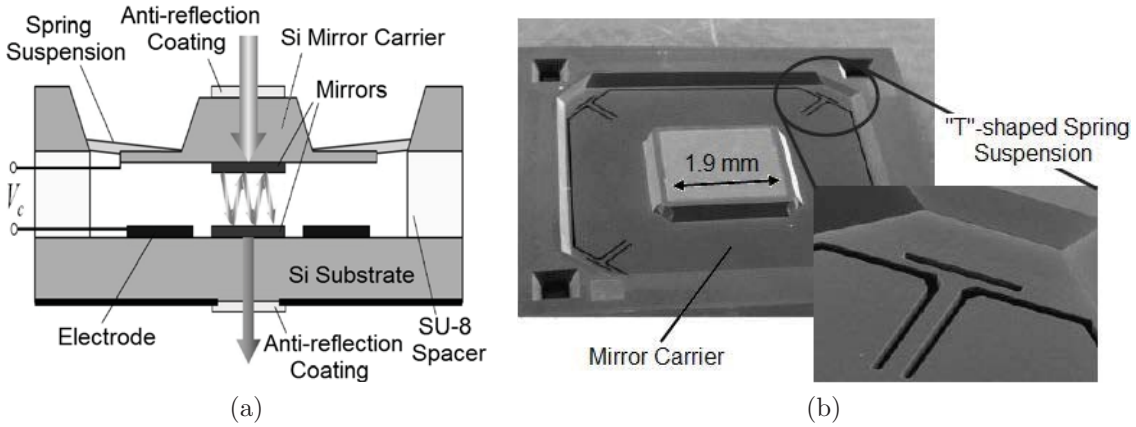

Figure 2.3: (a) Schematic of a bulk-micromachined MEMS-based LWIR Fabry-Perot filter developed by Ebermann et al. [23, 24], and (b) SEM micrograph of the filter. The images are taken from References [24] and [23], respectively.

The outer part of the suspended carrier wafer is used as the movable electrode, and is wet etched to reduce the spring thickness and thus ensure low actuation voltage. The filter is electrostatically actuated by applying a voltage between the bottom electrode and the upper Si carrier wafer.

In their work, thin film deposition conditions were optimized in order to balance the stresses in the suspended mirror and, consequently, outstanding mirror flatness was achieved. The center-to-edge mirror bowing was measured to be less than 15 nm over the entire mirror area of 1.9 mm × 1.9 mm. This filter was reported to have a wavelength tuning range from 10.5 µm down to 8 µm using an actuation voltage of 51 V, exhibiting a peak transmittance of 75-81% and a FWHM bandwidth of 105-200 nm over the entire tuning range. Because of the dual-band design, this filter simultaneously transmits the mid-wavelength infrared (MWIR) in the second interference order. With the actuation voltage of 51 V, the second-order transmission peak can be continuously tuned from 4.8 µm to 3.9 µm with a peak transmittance of 75-90 % and a FWHM bandwidth of less than 80 nm.

In this filter, the movable mirror carrier has significant mass, and acts as a mass-spring-damper system, which exhibits acceleration sensitivity. As a result, transmission peak wavelength can be shifted by external forces resulting from vibration, shock or the gravitational field of the earth. It was reported that for this filter quasi-static acceleration response of the central peak wavelength is between 25 nm/g and 50 nm/g.

In order to overcome this challenge, Meinig et al. [25] from the same research team developed a novel MEMS-based LWIR Fabry-Perot filter based on two spring-suspended mirrors. A schematic cross-section of the filter is shown in Figure 2.4a and an exploded view is given in Figure 2.4b. In this design, both the top and bottom mirror carriers (300 µm thick silicon wafers) are rectangular in shape and suspended by four meander shaped flexures. The top and bottom mirror carriers are wet etched to create cavities for electrodes and mirror coatings, and are assembled perpendicular to each other, forming an overlapping area in the middle and further overlapping parts with the chip frame of the opposite substrate. Mirrors are located in the center of the mirror carriers, while aluminum electrodes are deposited on the overlapping area on the chip frame of each substrate and are electrically isolated from the substrate by silicon dioxide. For actuation, both mirror carriers are connected to the same potential and a potential difference is applied to the aluminum electrodes. Thus, electric forces are generated between the electrodes and the opposite mirror carriers, which drive the two suspended mirror carriers to move towards each other.

Because the two movable mirror carriers are of equal mass, they are equally deflected by acceleration forces and hence the optical cavity length remains unaffected, avoiding the transmission peak wavelength change caused by acceleration forces. This design has a significantly reduced wavelength acceleration sensitivity of 4 nm/g in comparison to 25 nm/g for the design with one spring-suspended mirror.

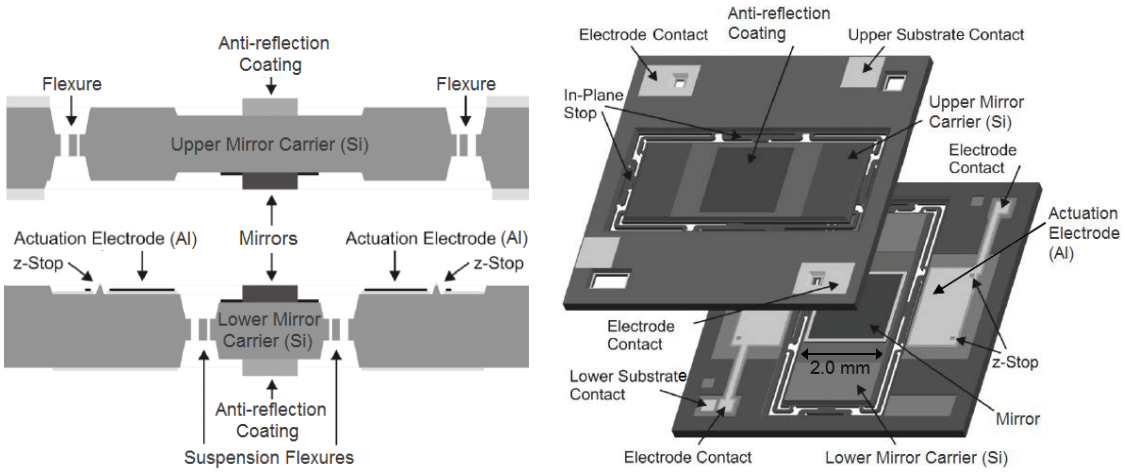

Figure 2.4: (a) Schematic cross-section of a bulk-micromachined MEMS-based LWIR Fabry-Perot filter developed by Meinig et al. [25] based on two spring-suspended mirrors, and (b) an exploded view of the filter. The images are taken from Reference [25].

Because the same mirror coatings are used, this filter shows nearly identical spectral characteristics to the filter in Figure 2.3, including a wavelength tuning range of 8-10.7 µm, a peak transmittance between 75-80%, and a FWHM of 115-200 nm in the first interference order, and a wavelength tuning range of 4.1-4.9 µm, a peak transmittance between 80-90%, and a FWHM of 57-97 nm in the second interference order. However, for such a two spring-suspended mirror design each mirror carrier only needs to travel half the required distance, therefore the maximum actuation voltage for tuning the full wavelength range is significantly reduced to 41 V in comparison to 51 V for the design with one movable mirror carrier.

2.3 Summary of reported MEMS-based longwave infrared Fabry-Perot filters

Table 2.1 summarizes published results on MEMS-based LWIR Fabry-Perot filters. It indicates that Ge/ZnS based Bragg mirrors combined with electrostatic actuators dominate this field, which are also the mirror type and actuator type chosen for the devices presented in this thesis.

Table 2.1: Summary of published results on MEMS-based tunable LWIR Fabry-Perot filters. Note that the filter spectral characteristics shown in (c) were measured at a liquid nitrogen temperature of 77 K.

	(a)	(b)	(c)	(d)	(e)
	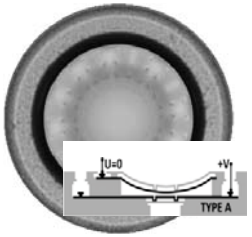	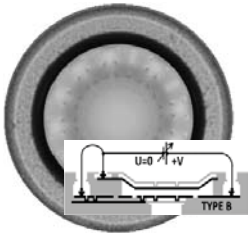	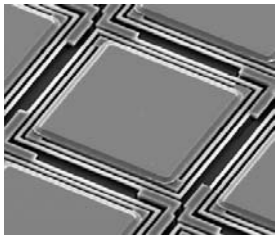	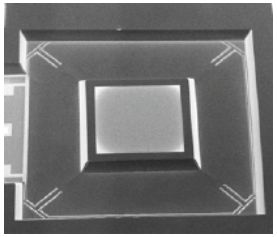	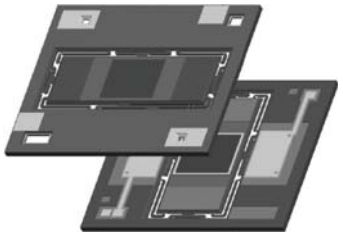
Authors [ref.]	Tuohiniemi et al. [20]	Tuohiniemi et al. [20, 21]	Stupar et al. [22]	Ebermann et al. [23, 24]	Meinig et al. [25]
Manufacturing technique	Surface micromachining	Surface micromachining	Bulk micromachining	Bulk micromachining	Bulk micromachining
Mirror type	Bragg reflector	Bragg reflector	Bragg reflector	Bragg reflector	Bragg reflector
Mirror materials	Si/air	Si/air	Not Disclosed	Ge/ZnS/(third material not disclosed)	Ge/ZnS/(third material not disclosed)
Aperture size	0.8 mm	0.8 mm	0.2 mm	1.9 mm	2 mm
Suspended mirror flatness	< 20 nm	< 20 nm	< 10 nm	< 15 nm	< 15 nm
Actuator type	Electrostatic	Electrostatic	Electrostatic	Electrostatic	Electrostatic
Actuation voltage	20 V	27 V	Not Disclosed	51 V	41 V
Wavelength tuning range	7.6–10.1 µm	7.2–10.1 µm	8–11 µm	8–10.5 µm	8–10.7 µm
Peak transmission	40–60%	50–60%	100%	75–81%	75–80%
FWHM	140–200 nm	140–170 nm	120 nm	105–200 nm	115–200 nm

Chapter 3

Optical design of tunable LWIR Fabry-Perot filters

This chapter gives a detailed discussion of Fabry-Perot theory as it applies to the optical design of tunable LWIR Fabry-Perot filters. The transmittance of an ideal Fabry-Perot filter is derived from the fundamental electromagnetic wave theory, which is followed by a description of important filter transmittance characteristics. Theory of quarter-wave mirrors is then reviewed and used to design LWIR Bragg mirrors. Transmission spectra of the designed tunable LWIR Fabry-Perot filter are modelled, demonstrating that the filter can achieve a spectral performance that exceeds the target specification for multispectral thermal imaging applications. Next, the influence of the thick supporting substrate on the filter transmittance is studied, followed by a detailed discussion of the effect of a single-layer anti-reflection coating on improving the transmittance characteristics of the designed LWIR Fabry-Perot filter. Finally, a viable modelling approach for calculating the transmittance of a Fabry-Perot filter in the presence of mirror imperfections is developed and presented.

3.1 Fabry-Perot cavity

This section starts with a brief introduction to the theory of light propagation within a thin-film assembly. The transmittance of an ideal Fabry-Perot filter is then derived from multiple beam interference, and a set of formulations describing the spectral characteristics of a Fabry-Perot filter are presented. Subsequently, the cavity order and mirror reflectivity requirements of a tunable LWIR Fabry-Perot filter for multispectral thermal imaging applications are determined.

3.1.1 Light propagation at a thin-film assembly

Light, as an electromagnetic wave, consists of electric and magnetic fields which synchronously oscillate perpendicular to each other and perpendicular to the direction of wave propagation. As electric and magnetic fields are defined in terms of each other, only one needs to be considered, and in subsequent discussions only the electric field is used. The electric field $\boldsymbol{E}$ for a light wave propagating along the z axis with time t can be written in a plane harmonic form as [26]

$$\boldsymbol{E}(z,t) = \xi \exp\left(-\frac{2\pi k}{\lambda} z\right) \exp\left[\mathrm{i}\left(wt - \frac{2\pi n}{\lambda} z\right)\right] \hat{\boldsymbol{x}}, \tag{3.1}$$

where ξ is the scalar magnitude of the electric field at position $z = 0$, n and k are the refractive index and extinction coefficient of the medium, respectively, w and λ are the angular frequency and wavelength of the propagating wave, respectively, and $\hat{\boldsymbol{x}}$ is a unit vector orthogonal to the propagation axis z.

When light strikes an assembly of thin films separating two bulk media, as illustrated in Figure 3.1, the incident light wave will be split into a reflected wave and a transmitted wave. For clarity of discussion, we denote the optical terms associated with the incident, reflected and transmitted waves by the subscripts i, r and t, respectively. If we limit our discussion to the normal incidence case, then for a given incident electric field $\boldsymbol{E}_i$, the reflected field $\boldsymbol{E}_r$ and transmitted field $\boldsymbol{E}_t$ can be written as

$$\boldsymbol{E}_r = \boldsymbol{\rho}\boldsymbol{E}_i = \rho \mathrm{e}^{-\mathrm{i}\varphi_r} \boldsymbol{E}_i, \tag{3.2}$$

and

$$\boldsymbol{E}_t = \boldsymbol{\tau}\boldsymbol{E}_i = \tau \mathrm{e}^{-\mathrm{i}\varphi_t} \boldsymbol{E}_i, \tag{3.3}$$

where $\boldsymbol{\rho}$ and $\boldsymbol{\tau}$ are defined as the reflection coefficient and transmission coefficient of the thin-film assembly, respectively. While the terms ρ and τ represent the scalar magnitude changes of the reflected and transmitted fields relative to the incident field, the terms φ_r and φ_t represent the relative phase changes.

Despite the wave nature of light, it is the energy associated with light that is detected by the detector. The irradiance vector $\boldsymbol{I}$ (or intensity vector) is the most practically used energy quantity, and is defined as [26]

$$\boldsymbol{I} = \frac{1}{2} n \sqrt{\frac{\varepsilon_0}{\mu_0}} \boldsymbol{E}\boldsymbol{E}^* \hat{\boldsymbol{z}}, \tag{3.4}$$

where $\varepsilon_0 = 8.854 \times 10^{-12}\,\mathrm{Fm}^{-1}$ and $\mu_0 = 4\pi \times 10^{-7}\,\mathrm{Hm}^{-1}$ are the permittivity and permeability of free space, respectively, and $\hat{\boldsymbol{z}}$ is a unit vector in the direction of

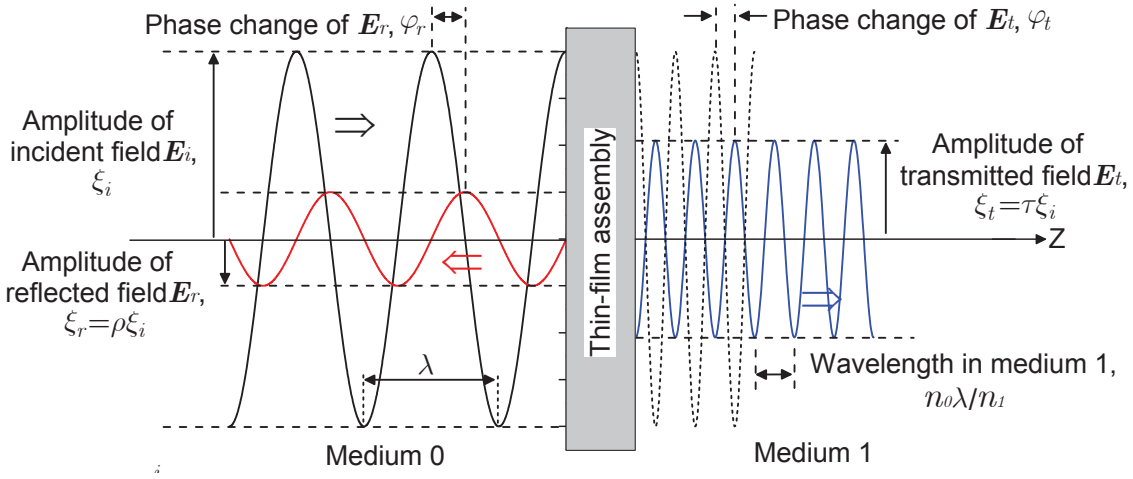

Figure 3.1: Illustration of the reflected and transmitted light waves generated from an incident wave striking a thin-film assembly which separates two lossless media. In the figure, an imaginary transmitted wave (dashed line) which inherits the phase from the incident wave is depicted for the purpose of illustrating the concept of transmission phase change φ_t.

light propagation. Substituting Equation (3.1) for $\boldsymbol{E}$ in Equation (3.4), the scalar irradiance can be written as

$$I = \frac{1}{2} n \sqrt{\frac{\varepsilon_0}{\mu_0}} \xi^2 \exp\left(-\frac{4\pi k}{\lambda} z\right). \tag{3.5}$$

Equation (3.5) implies that the irradiance of light propagating in a lossy medium ($k \neq 0$) falls off exponentially and drops to 1/e of its initial value at a distance $z = \lambda/4\pi k$, while remaining constant in a lossless medium ($k = 0$). In terms of the definition of the reflectance and transmittance of a thin-film assembly, there is no need to consider how the reflected and transmitted light waves propagate in the media, since only the relative changes of irradiance at the incident and exiting interfaces of the thin-film assembly are of concern. Therefore, we can neglect the propagation-related exponential term in Equation (3.5), and the scalar irradiance is further simplified as

$$I \sim n\xi^2. \tag{3.6}$$

The reflectance R and transmittance T of the thin-film assembly can be calculated as [26]

$$R = \frac{I_r}{I_i} = \frac{n_0 {\xi_r}^2}{n_0 {\xi_i}^2} = \rho^2, \tag{3.7}$$

and

$$T = \frac{I_t}{I_i} = \frac{n_1 {\xi_t}^2}{n_0 {\xi_i}^2} = \frac{n_1}{n_0}\tau^2, \tag{3.8}$$

where n_0 and n_1 represent the refractive indices of the incident and exiting media, respectively.

The refractive index terms in Equation (3.8) for T arise from the definition of $\boldsymbol{I}$, and should always be included in the calculation if the media in which the incident and transmitted light waves propagate are different. These terms cancel out for R simply because the incident and reflected light waves propagate in the same medium. The optical terms presented in this section are of significant importance for the derivation of the transmittance of a Fabry-Perot filter in the following section.

3.1.2 Transmittance of an ideal Fabry-Perot filter

This section derives the transmittance of an ideal Fabry-Perot filter from the electric field vectors and field reflection and transmission coefficients. The heart of the tunable LWIR filter under discussion in this thesis is a Fabry-Perot etalon, which consists of two mirrors spaced by a distance d, as depicted in Figure 3.2a. While the bottom mirror sits on a substrate which has a refractive index n_S, the top mirror is suspended in free space with refractive index $n = 1$. The structure and properties of these mirrors will be considered in detail in Section 3.2, but at the current stage of discussion, the mirrors are modelled as two arbitrary thin-film assemblies. The electric field reflection and transmission coefficients are defined separately for each mirror and for different light propagating directions as shown in Figure 3.2a, where the subscript (1 or 2) denotes the mirror, and coefficients for light travelling in the opposite direction to the incident light are denoted by a superscript '-'.

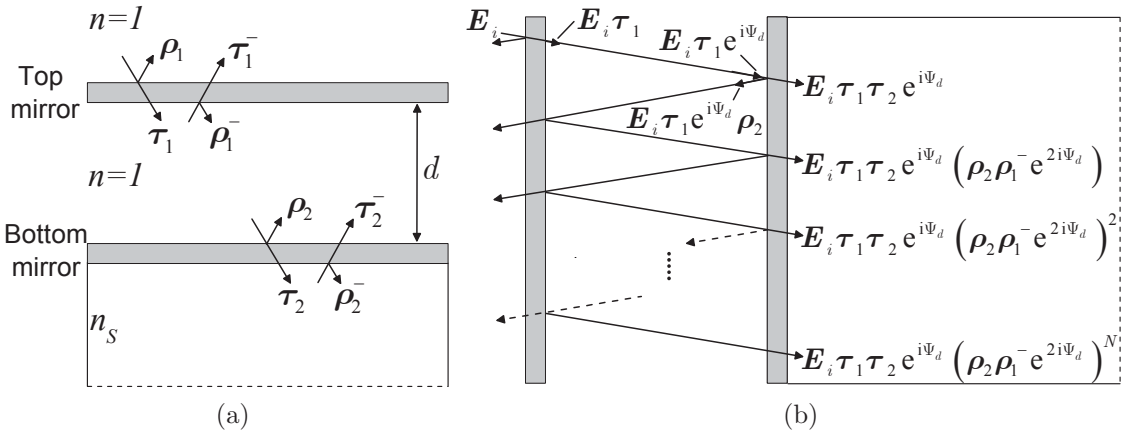

Figure 3.2: (a) Convention defining the reflection and transmission coefficients for each mirror and for each direction of light propagation. (b) Multiple reflections and transmissions of an electromagnetic wave between the two mirrors of a Fabry-Perot etalon. Only the normal incidence case is considered in this thesis; angled light paths are shown for clarity only.

Upon incidence, the light wave undergoes multiple (theoretically infinite) reflections and transmissions between the mirrors, as depicted in Figure 3.2b. The electric field of the propagating light wave immediately after the incident wave $\boldsymbol{E}_i$ has passed the top mirror is $\boldsymbol{E}_i\boldsymbol{\tau}_1$. After this light wave has traversed the cavity and is incident on the bottom mirror, a phase change of $\Psi_d = 2\pi d/\lambda$ occurs and the electric field becomes $\boldsymbol{E}_i\boldsymbol{\tau}_1 \mathrm{e}^{\mathrm{i}\Psi_d}$. The electric field $\boldsymbol{E}_{t1}$ of the light wave after the first transmission through the bottom mirror is

$$\boldsymbol{E}_{t1} = \boldsymbol{E}_i\boldsymbol{\tau}_1\boldsymbol{\tau}_2 \mathrm{e}^{\mathrm{i}\Psi_d}. \tag{3.9}$$

Part of the light incident on the bottom mirror is reflected back to the top mirror, with an electric field $\boldsymbol{E}_i\boldsymbol{\tau}_1 \mathrm{e}^{\mathrm{i}\Psi_d}\boldsymbol{\rho}_2$. After another reflection from the top mirror and the second transmission through the bottom mirror, the electric field $\boldsymbol{E}_{t2}$ becomes

$$\boldsymbol{E}_{t2} = \boldsymbol{E}_i\boldsymbol{\tau}_1\boldsymbol{\tau}_2 \mathrm{e}^{\mathrm{i}\Psi_d} \left(\boldsymbol{\rho}_2\boldsymbol{\rho}_1^- \mathrm{e}^{2\mathrm{i}\Psi_d}\right). \tag{3.10}$$

Based on Equations (3.9) and (3.10), the law for the partial light waves being transmitted can be derived: after each round trip the field amplitude has to be multiplied by a factor of $\boldsymbol{\rho}_2\boldsymbol{\rho}_1^- \mathrm{e}^{2\mathrm{i}\Psi_d}$. Therefore, the electric field $\boldsymbol{E}_{tN}$ of the light wave after N transmission events through the bottom mirror can be written as

$$\boldsymbol{E}_{tN} = \boldsymbol{E}_i\boldsymbol{\tau}_1\boldsymbol{\tau}_2 \mathrm{e}^{\mathrm{i}\Psi_d} \left(\boldsymbol{\rho}_2\boldsymbol{\rho}_1^- \mathrm{e}^{2\mathrm{i}\Psi_d}\right)^{N-1}. \tag{3.11}$$

All the partial light (theoretically infinite) transmitted through the bottom mirror superimposes to yield a total electric field

$$\boldsymbol{E}_t = \sum_{N=0}^{\infty} \boldsymbol{E}_i\boldsymbol{\tau}_1\boldsymbol{\tau}_2 \mathrm{e}^{\mathrm{i}\Psi_d} \left(\boldsymbol{\rho}_2\boldsymbol{\rho}_1^- \mathrm{e}^{2\mathrm{i}\Psi_d}\right)^{N}. \tag{3.12}$$

This sum is a geometric series and can be expressed in a closed form as

$$\boldsymbol{E}_t = \frac{\boldsymbol{E}_i\boldsymbol{\tau}_1\boldsymbol{\tau}_2 e^{\mathrm{i}\Psi_d}}{1 - \boldsymbol{\rho}_2\boldsymbol{\rho}_1^- e^{2\mathrm{i}\Psi_d}}. \tag{3.13}$$

According to Equation (3.4), the transmittance T_{FP} of the Fabry-Perot etalon can be calculated as

$$T_{FP} = \frac{I_t}{I_i} = \frac{n_S}{1}\frac{\boldsymbol{E}_t\boldsymbol{E}_t^*}{\boldsymbol{E}_i\boldsymbol{E}_i^*} = \frac{n_S}{1}\left[\frac{\boldsymbol{\tau}_1\boldsymbol{\tau}_2 e^{\mathrm{i}\Psi_d}}{1 - \boldsymbol{\rho}_2\boldsymbol{\rho}_1^- e^{2\mathrm{i}\Psi_d}}\right]\left[\frac{\boldsymbol{\tau}_1\boldsymbol{\tau}_2 e^{\mathrm{i}\Psi_d}}{1 - \boldsymbol{\rho}_2\boldsymbol{\rho}_1^- e^{2\mathrm{i}\Psi_d}}\right]^*. \tag{3.14}$$

While all phase terms in the numerator will cancel out in the complex conjugation operation, the phase terms in the denominator can be incorporated into a single parameter Ψ, yielding

$$T_{FP} = \frac{n_S}{1}\left[\frac{\tau_1\tau_2}{1 - \rho_2\rho_1^- e^{\mathrm{i}\Psi}}\right]\left[\frac{\tau_1\tau_2}{1 - \rho_2\rho_1^- e^{-\mathrm{i}\Psi}}\right], \tag{3.15}$$

where

$$\Psi = 2\Psi_d - \varphi_{r1}^{-} - \varphi_{r2} = \frac{4\pi d}{\lambda} - \varphi_{r1}^{-} - \varphi_{r2} \tag{3.16}$$

is the total phase change experienced on a round-trip of the cavity between the two mirrors, including the reflection phase changes at the top and bottom mirrors, φ_{r1}^{-} and φ_{r2}. Equation (3.15) can also be expressed in another form as

$$T_{FP} = \left(\frac{\frac{1}{1}\tau_1^2 \frac{n_S}{1}\tau_2^2}{1 + \rho_2^2\left(\rho_1^{-}\right)^2 - 2\rho_2\rho_1^{-}\cos\Psi} \right), \tag{3.17}$$

and relating these terms to the reflectance, R_1^{-} and R_2, and transmittance, T_1 and T_2, of the two mirrors yields

$$T_{FP} = \frac{T_1 T_2}{1 + R_2 R_1^{-} - 2\sqrt{R_2 R_1^{-}}\cos\Psi}. \tag{3.18}$$

The notation for the mirror reflectance and transmittance in Equation (3.18) is consistent with that for electric field reflection and transmission coefficients as shown in Figure 3.2a. Equation (3.18) is well known as the transmittance of an ideal Fabry-Perot filter. In this thesis, an ideal Fabry-Perot filter refers to a filter whose mirrors are perfectly flat, parallel and smooth. Section 3.4 will describe how the transmittance is affected when these conditions are not met.

3.1.3 Transmittance characteristics of an ideal Fabry-Perot filter

While the transmittance of an ideal Fabry-Perot filter was derived from first principles in Section 3.1.2, this section will use an alternative form of Equation (3.18) to present the transmittance characteristics of an ideal Fabry-Perot filter. The new equation uses the variables as defined in Figure 3.3, many of which have already been introduced. The cavity medium is free space ($n = 1$) in all calculations.

Using the relationship $cos\Psi = 1 - 2sin^2(\Psi/2)$, the transmittance T_{FP} of an ideal Fabry-Perot filter, Equation (3.18), can be alternatively expressed as

$$T_{FP} = \frac{T_{pk}}{1 + (4F_R^2/\pi^2)\sin^2\left(\frac{\Psi}{2}\right)}, \tag{3.19}$$

where T_{pk} is the peak transmittance, given by

$$T_{pk} = \frac{T^2}{(1-R)^2}, \tag{3.20}$$

F_R is the reflectance finesse of the filter, given by

$$F_R = \frac{\pi\sqrt{R}}{1-R}, \tag{3.21}$$

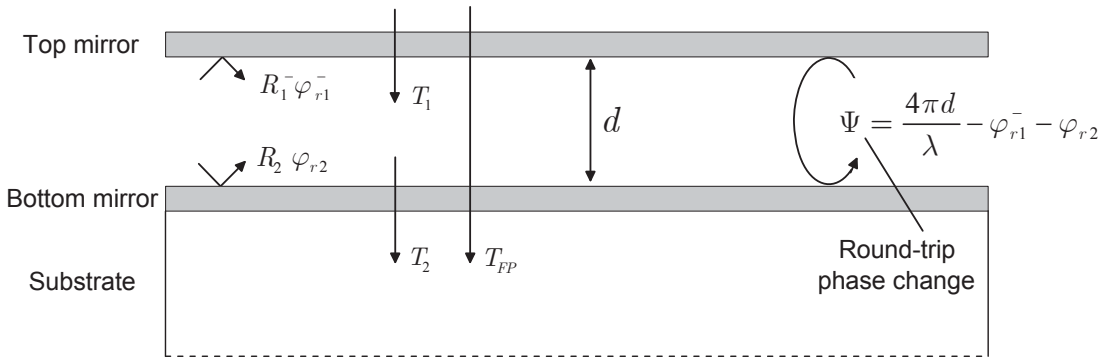

Figure 3.3: Definition of terms used in the text for an ideal Fabry-Perot filter. Only normal incidence light is considered in this thesis. The reflection is drawn at an angle for clarity only.

and $R = \sqrt{R_1^- R_2}$ and $T = \sqrt{T_1 T_2}$. The round-trip phase change Ψ in Equation (3.19) is given by

$$\Psi = 2\Psi_d - \varphi = \frac{4\pi d}{\lambda} - \varphi, \tag{3.22}$$

where $\varphi = \varphi_{r1}^- + \varphi_{r2}$ is the sum of the reflection phase changes from the top and bottom mirrors. Transmission peaks in Equation (3.19) occur when

$$\Psi = 2\pi m, \tag{3.23}$$

where m is an integer and termed the order of the transmission peak. The condition for transmittance minima is

$$\Psi = 2\pi \left(m + \frac{1}{2} \right), \tag{3.24}$$

and at this condition the sinusoidal term in Equation (3.19) is equal to 1. The minimum transmittance, T_{min}, can be calculated as

$$T_{min} = \frac{T_{pk}}{1 + 4F_R^2/\pi^2}. \tag{3.25}$$

According to Equation (3.25), out-of-band rejection, $\Re$, which is defined as the ratio of peak transmittance to minimum transmittance, can be expressed as

$$\Re = 1 + \frac{4F_R^2}{\pi^2}. \tag{3.26}$$

The full-width at half-maximum (FWHM) or the spectral bandwidth of a Fabry-Perot filter is the wavelength interval over which the transmittance is equal to or greater than half the peak transmittance. This FWHM characteristic, $\delta\lambda$, has been reported by Atherton et al. [27] as

$$\delta\lambda = \frac{\lambda}{F_R \left(m + \frac{\varphi}{2\pi} + \frac{\lambda}{2\pi} \frac{\partial \varphi}{\partial \lambda} \right)}. \tag{3.27}$$

The free spectral range, $\Delta\lambda$, defined as the wavelength separation between the m-order transmission peak and the $(m+1)$-order transmission peak, has been reported as

$$\Delta\lambda = \frac{\lambda}{\left(m + 1 + \frac{\varphi}{2\pi} + \frac{\lambda}{2\pi}\frac{\partial\varphi}{\partial\lambda}\right)}. \tag{3.28}$$

As implied by Equations (3.27) and (3.28), the finesse of a filter, F_R, is actually the ratio of the free spectral range $\Delta\lambda$ to the spectral bandwidth $\delta\lambda$ or, in other words, the number of spectral bands that are resolvable within the free spectral range.

3.1.4 LWIR Fabry-Perot cavity design

The transmittance of an ideal Fabry-Perot filter, T_{FP}, namely Equation (3.19), is plotted in Figure 3.4 as a function of λ (represented by cavity length d) for various mirror reflectivities. In these plots, the effect of mirror reflection phase changes is not included, but it will be examined in detail in Section 3.2.6. Transmission peaks periodically occur at the wavelengths obeying Equation (3.23), representing different cavity orders. If by electromechanical actuation the cavity length d is decreased, the transmitted spectral peaks will shift to shorter wavelengths, realizing a tunable filter. A bandpass "order-sorting" filter is conjunctively used to block the unwanted orders and to define the transmission window of the tunable filter.

The primary consideration in the design of a tunable LWIR Fabry-Perot filter is the choice of cavity order. As can be seen in Figure 3.4, a higher order cavity features a narrower FWHM, however, it does not necessarily mean that we can use a higher order cavity for our LWIR tunable Fabry-Perot filters, since this reduces the

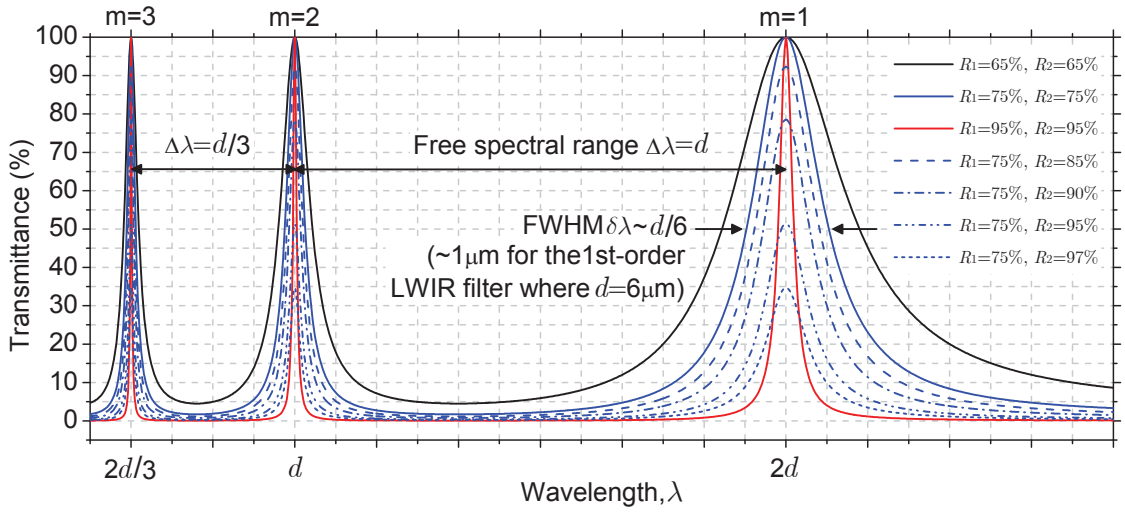

Figure 3.4: Transmittance of an ideal Fabry-Perot filter for various mirror reflectivities.

free spectral range. Free spectral range associated with the chosen cavity order has to be larger than the designed wavelength tuning range of 8-12 µm, otherwise higher order spectral peaks would simultaneously appear in the transmission window and be detected, causing wavelength ambiguity. As implied by Figure 3.4, the 1st-order cavity design requires a cavity length of $d = 6$ µm, while the 2nd-order cavity design requires a cavity length of $d = 12$ µm. Taking into account the effect of mirror reflection phase changes on narrowing the free spectral range of a filter (see Section 3.2.6), we can see that only the 1st-order cavity is capable of providing sufficient free spectral range to avoid the order ambiguity within the range of 8-12 µm, and therefore is the chosen cavity order for the LWIR tunable Fabry-Perot filters presented in this thesis.

As can be seen from Figure 3.4, the spectral characteristics of a Fabry-Perot filter, such as peak transmittance and FWHM, also depend on the finesse of the optical cavity which, in turn, depends on the reflectivity of the mirrors. As mirror reflectivity increases, the transmission spectrum pattern becomes sharper, resulting in narrower FWHM. As evident from Figure 3.4, in order for the 1st-order LWIR Fabry-Perot filter ($d = 6$ µm) to achieve a FWHM less than 1 µm, which meets the wavelength discrimination requirement for multispectral thermal imaging applications, the reflectivity of the two mirrors needs to be higher than 75%. It can also be noted from Figure 3.4 that high mirror reflectivity may also be a disadvantage for achieving high filter transmittance unless the reflectivity of the two mirrors is matched. While identical reflectivity for both mirrors leads to a unity peak transmittance, any difference in reflectivity between the mirrors significantly reduces the peak transmittance of a filter. For example, filters with one mirror having 75% reflectivity and the other mirror having 95% or even higher reflectivity exhibit a peak transmittance below 50%. This finding implies that the difference in reflectivity between the top and bottom mirrors of a Fabry-Perot filter needs to be less than 20% in order to achieve the targeted filter peak transmission of $> 50\%$ as listed in Table 1.1.

The mirror reflectivity requirements described here will be used in the following section to guide the design of the quarter-wave mirrors for our LWIR tunable Fabry-Perot filters.

3.2 Quarter-wave mirrors (QWMs)

Quarter-wave mirrors are by far the most commonly used mirror type in MEMS-based Fabry-Perot filters, and are the chosen mirror type for the devices presented

in this thesis. This section discusses the basis of quarter-wave mirrors, and uses the existing theory to design LWIR quarter-wave mirrors according to the mirror reflectivity requirements described in Section 3.1.4. Tuning spectra of the resulting LWIR Fabry-Perot filter design are modelled, and the influence of reflection phase changes of the quarter-wave mirrors on the spectral characteristics of the designed LWIR tunable Fabry-Perot filter is also examined.

3.2.1 Maximum reflectivity

Quarter-wave mirrors (QWMs) are a subset of distributed Bragg reflectors that use layers with thicknesses of $\lambda_C/4n$ (first order) or an odd multiple of $\lambda_C/4n$ (higher order), where n is the refractive index of the layer material and λ_C is the free-space central wavelength for which the mirror is designed to have a maximum reflectivity. In this thesis, we limit our discussion to first-order mirrors. More detailed knowledge related to higher-order mirrors can be found in Ref. [26]. In the most common implementation of QWMs, successive layers alternate between one material with a high refractive index n_H and another material with a low refractive index n_L. For convenience of discussion, the QWM consisting of N high-index low-index layer pairs is denoted as having N periods. If the QWM has an unpaired layer, the QWM is denoted as having $N + 1/2$ periods.

Figure 3.5 illustrates a 3-period QWM and explains the physics of QWMs using interference concepts. Upon incident, light undergoes successive reflections and transmissions at the layer interfaces within the QWM. To simplify discussion, only primary reflections are considered, while secondary multiple reflections are not taken into account. Light reflected at the low-to-high index interface has a phase shift of π, while no such phase shift occurs for transmitted light or light that is reflected at the high-to-low index interface [26]. Light with a wavelength of λ_C also experiences a phase change of $\pi/2$ as it traverses each quarter-wave layer. Overall, the various components of the incident light ($\lambda = \lambda_C$) produced by reflection at successive layer interfaces throughout the mirror will appear at the front surface all in phase and recombine constructively, resulting in a maximum reflectivity if material absorption of the QWM is negligible.

As previously discussed in Section 3.1.4, high-performance Fabry-Perot filters typically require high reflectivity mirrors. The highest reflectivity for a given N or $N + 1/2$ period QWM is always achieved when the first layer has a high refractive index [26, 28], for light incident from free space and propagating towards the

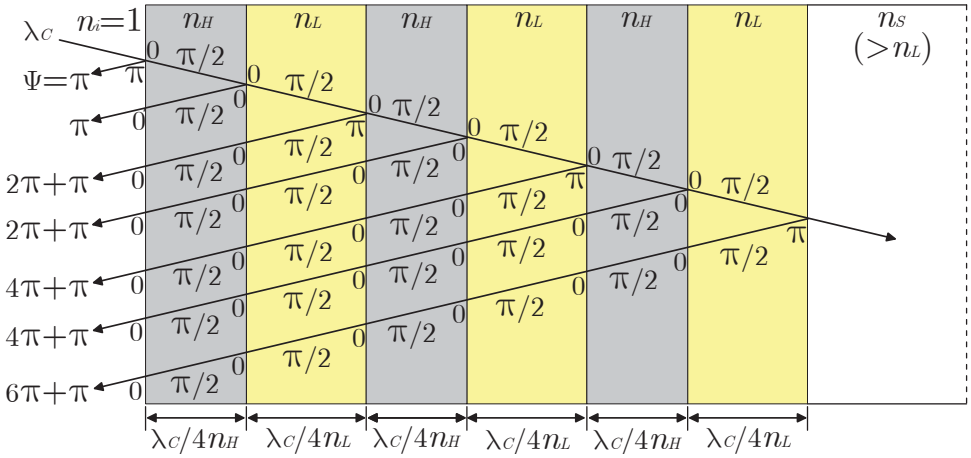

Figure 3.5: Schematic of a 3-period QWM, where the incident medium is free space ($n_i = 1$) and the exiting medium is a substrate with its refractive index (n_S) greater than that (n_L) of the low index material. Constructive interference of all reflections from successive layer interfaces leads to a maximum reflectivity at the design wavelength λ_C. Normal incidence light is considered in this thesis; angled light paths are shown for clarity only. For simplicity of discussion, only primary reflections are considered, and secondary multiple reflections are not taken into account.

substrate. For a lossless N-period QWM with a high-index first layer, the mirror reflectivity at the central design wavelength λ_C, $R(N)$, is given by [28]

$$R(N) = \left(\frac{n_S (n_H/n_L)^{2N} - 1}{n_S (n_H/n_L)^{2N} + 1} \right)^2, \tag{3.29}$$

and for a $N + 1/2$-period QWM,

$$R(N + 1/2) = \left(\frac{(n_H^2/n_S)\,(n_H/n_L)^{2N} - 1}{(n_H^2/n_S)\,(n_H/n_L)^{2N} + 1} \right)^2, \tag{3.30}$$

where n_H, n_L and n_S are the refractive indices of the high-index material, the low-index material and the substrate, respectively.

For MEMS-based Fabry-Perot filters, the top mirror is usually suspended in air. Let $n_S = 1$ in Equations (3.29) and (3.30) and also consider the monotonically increasing nature of the function $(x-1)/(x+1)$ when $x > 1$, we can get $R(N+1/2) > R(N+1)$ and $R(N+1/2) > R(N)$. This implies that, for the top suspended QWM, the highest reflectivity is always achieved with a mirror that has an unpaired layer. The bottom QWM may not necessarily follow the $N + 1/2$ period design when a substrate is present. It can be shown analytically from Equations (3.29) and (3.30) that $R(N+1) > R(N+1/2)$ when $n_S > n_L$. This implies that, for the bottom QWM

on a high-refractive-index substrate, the highest reflectivity is always obtained with a mirror having an even number of layers. Note that in both cases, the QWM has a high-index top layer.

3.2.2 QWM high-reflectivity bandwidth

For quarter-wave mirrors, the reflections from successive layer interfaces are in phase and add constructively to produce a maximum reflectivity at the design wavelength of λ_C. As the wavelength moves away from this central wavelength, the phase mismatch grows and destructive interference develops, resulting in a decrease in the mirror reflectivity. However, as long as the wavelength is sufficiently near the central wavelength λ_C, the mirror reflectivity still remains high, although not as high as that at λ_C. Macleod [26] defines the high-reflectivity bandwidth of a QWM as the range of wavelengths over which the mirror reflectivity approaches 100% as the mirror period N becomes large. This definition of high-reflectivity bandwidth is based on a very large N. However, even when N is small, this definition of bandwidth gives a good rule-of-thumb approximation of the range of wavelengths over which a QWM is suitable for use in a Fabry-Perot filter.

From Macleod [26], the high-reflectivity bandwidth of a QWM extends from a short wavelength, λ_{SB}, to a long wavelength, λ_{LB}, according to

$$\frac{\lambda_C}{\lambda_{SB}} - \frac{\lambda_C}{\lambda_{LB}} = \frac{4}{\pi} sin^{-1}\left(\frac{n_H - n_L}{n_H + n_L}\right). \tag{3.31}$$

Neglecting refractive index dispersion, the reflectivity spectrum is even-symmetric with $1/\lambda_C$ and, as a consequence, λ_C is related to λ_{SB} and λ_{LB} by

$$\frac{1}{\lambda_C} = \frac{1}{2}\left(\frac{1}{\lambda_{SB}} + \frac{1}{\lambda_{LB}}\right). \tag{3.32}$$

Equation (3.31) shows that the high-reflectivity bandwidth of a QWM depends on the ratio of the refractive indices of the two materials used for the construction of the QWM. Considering the monotonically increasing nature of $sin^{-1}\left[(x-1)/(x+1)\right]$ when $x > 1$, it can be shown analytically with Equations (3.31) and (3.32) that as the refractive index ratio becomes larger, the high-reflectivity bandwidth becomes wider.

3.2.3 Optical matrix model

Provided that the layer materials used for QWMs are lossless, Equations (3.29) and (3.30) in Section 3.2.1 can be employed to calculate the reflectivity of QWMs,

but only at the central design wavelength of λ_C. This section presents the optical matrix model for calculating the reflectivity of QWMs over the entire spectrum for the general case of absorbing layer materials. This thesis will also make considerable use of this method for modelling the transmittance of Fabry-Perot filters. Macleod [26] gives a complete derivation of the optical matrix model for the general case of oblique incidence and a weakly absorbing substrate. In this thesis only normal incidence light is considered and the substrate is assumed to be lossless.

A QWM or a Fabry-Perot filter can both be considered as a thin-film assembly, as depicted in Figure 3.6, with each individual thin-film layer f having a thickness d_f, a refractive index n_f and an extinction coefficient k_f. The incident medium is free space with an admittance of $\eta_0 = \sqrt{\varepsilon_0/\mu_0} = 2.65 \times 10^{-3}\ \Omega^{-1}$, and the exit medium is a lossless substrate with a refractive index of n_S. The optical characteristic matrix of layer f is then given by

$$[M_f] = \begin{bmatrix} \cos\delta_f & (\mathrm{i}/\eta_f\ )\sin\delta_f \\ \mathrm{i}\eta_f \sin\delta_f & \cos\delta_f \end{bmatrix}, \tag{3.33}$$

where η_f is the optical admittance of layer f, given by

$$\eta_f = \eta_0\,(n_f - \mathrm{i}k_f)\,, \tag{3.34}$$

and δ_f is the optical phase advance on a single traversal of layer f, given by

$$\delta_f = 2\pi d_f\,(n_f - \mathrm{i}k_f)/\lambda. \tag{3.35}$$

The characteristic matrix for the entire thin-film assembly is simply the product of the characteristic matrices of all layers taken in the correct order, given by

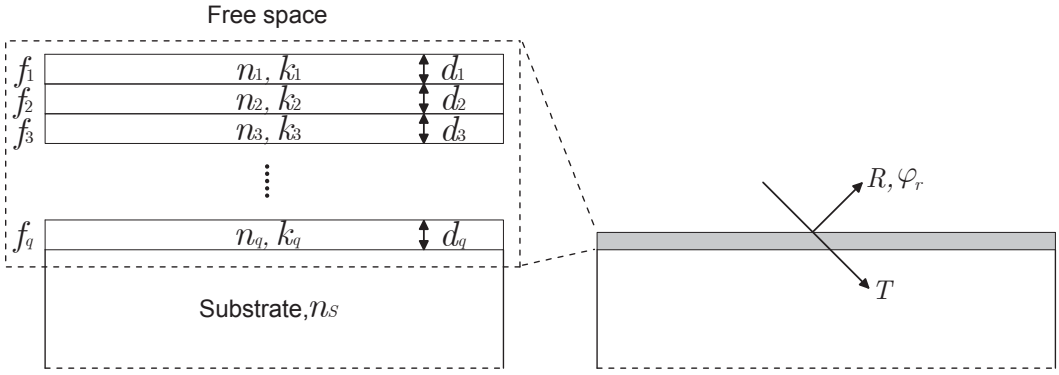

Figure 3.6: A QWM or a Fabry-Perot filter can both be considered as an assembly of thin-film layers. Normal incidence light is considered and angled light paths are shown for clarity only.

$$\begin{bmatrix} B \\ C \end{bmatrix} = \left\{ \prod_{f=1}^{q} \begin{bmatrix} \cos\delta_f & (\mathrm{i}/\eta_f)\sin\delta_f \\ \mathrm{i}\eta_f \sin\delta_f & \cos\delta_f \end{bmatrix} \right\} \begin{bmatrix} 1 \\ \eta_0 n_S \end{bmatrix}. \tag{3.36}$$

Based on Equation (3.36), the reflectance R and transmittance T of the stack can be calculated via

$$R = \left(\frac{\eta_0 B - C}{\eta_0 B + C}\right)\left(\frac{\eta_0 B - C}{\eta_0 B + C}\right)^* = \left|\frac{\eta_0 B - C}{\eta_0 B + C}\right|^2 \tag{3.37}$$

and

$$T = \frac{4\eta_0^2 n_S}{(\eta_0 B + C)(\eta_0 B + C)^*} = \frac{4\eta_0^2 n_S}{|\eta_0 B + C|^2}, \tag{3.38}$$

respectively.

Another important quantity that can be computed from Equation (3.36) is the phase change associated with reflection, φ_r, which is calculated via

$$\varphi_r = \arctan\left(\frac{-2b\eta_0}{\eta_0^2 - a^2 - b^2}\right), \tag{3.39}$$

where a and b are the real and imaginary components of C/B, respectively. Equation (3.39) must be interpreted on the basis of the phase quadrants convention following Macleod [26]. It is important to preserve separately the signs of the numerator and denominator in Equation (3.39) as shown in Table 3.1, otherwise the quadrant (and thus the reflection) phase change cannot be uniquely determined.

Table 3.1: Quadrants convention for reflection phase change.

Numerator	+	+	−	−
Denominator	+	−	−	+
φ_r	$(0 - \pi/2)$	$(\pi/2 - \pi)$	$(\pi - 3\pi/2)$	$(3\pi/2 - 2\pi)$

3.2.4 Ge/ZnS based LWIR QWMs

LWIR optical transparency and high refractive index contrast are the primary criteria for the selection of materials used for building LWIR QWMs. High optical transparency ensures high mirror reflectivity and thus high filter transmittance. As suggested by Equations (3.29) and (3.30) in Section 3.2.1, high refractive index contrast is advantageous for achieving high mirror reflectivity with a small number of mirror layer periods. In addition, high refractive index contrast is also advantageous for achieving a broad high-reflectivity bandwidth for QWMs, as suggested by Equations (3.31) and (3.32) in Section 3.2.2.

There exist relatively few materials that transmit LWIR light [29], which are listed in Table 3.2. Among all these materials, Ge has the highest refractive index ($n = 4.0$) and is transparent over the entire 8-12 µm wavelength band, making it an ideal high-index material for LWIR QWMs. For the selection of the low-index material, although CaF_2 has the lowest refractive index available, it absorbs significantly for wavelengths longer than 10 µm, and therefore is not suitable for use in LWIR QWMs. Instead, ZnS has the next lowest refractive index ($n = 2.2$), and exhibits wideband transparency extending to wavelengths as long as 20 µm. Therefore, ZnS was chosen as the low-index material for LWIR QWMs. An additional benefit of using ZnS as the low-index material is that because the refractive index ($n = 2.2$) of ZnS is close to the square root of that of the silicon substrate ($n = 3.4$), a quarter-wavelength thick ZnS single layer can be used as an adequate anti-reflection coating, thus negating the need of a third material. Further discussion related to the ZnS single-layer anti-reflection coating is presented in Section 3.3. For the above reasons, Ge and ZnS are by far the most commonly used mirror materials in the reported MEMS-based LWIR Fabry-Perot filters (see Chapter 2), and also the chosen mirror materials for the devices presented in this thesis.

Table 3.2: The usable spectral bands and refractive indices (at 10 µm) of common LWIR optical materials [29].

Material	Spectral range (µm)	Refractive index (at 10 µm)
Ge	2-17	4.0
Si	1.2-70	3.4
GaAs	0.9-16	3.28
CdTe	2-25	2.65
AMTIR-1	0.7-14	2.5
AMTIR-3	1-14	2.6
AMTIR-4	1-14	2.64
GASIR1	1-14	2.49
GASIR2	1-14	2.58
ZnSe	0.55-20	2.41
ZnS	0.37-20	2.2
CaF_2	0.13-10	1.3

The central design wavelength λ_C of the Ge/ZnS based LWIR QWMs needs to be properly chosen in order to let the mirror high-reflectivity bandwidth lie within the 8-12 µm wavelength range. Employing a trial-and-error search for the optimal λ_C using Equations (3.31) and (3.32), the optimal central design wavelength λ_C was chosen to be 9.7 µm. As a consequence, this yields a mirror bandwidth extending from a short wavelength of $\lambda_{SB} = 8.1$ µm to a long wavelength of $\lambda_{LB} = 11.9$ µm,

which is only slightly less than the LWIR range of 8-12 µm. It will become evident in Section 3.2.5 that this bandwidth narrowing is so small that it exerts no influence on the filter transmittance spectra within the 8-12 µm range. At $\lambda_C = 9.7$ µm, the quarter-wave thicknesses of the Ge and ZnS mirror layers were calculated to be 606 nm and 1102 nm, respectively.

Figure 3.7a and Figure 3.7b depict the reflectivity spectra of Ge/ZnS QWMs with 0.5, 1.5, 2.5 and 3.5 periods suspended in air and Ge/ZnS QWMs with 1, 2, 3 and 4 periods on a silicon substrate, respectively, calculated using the optical matrix model; i.e., Equation (3.37). The optical constants of the Ge and ZnS used

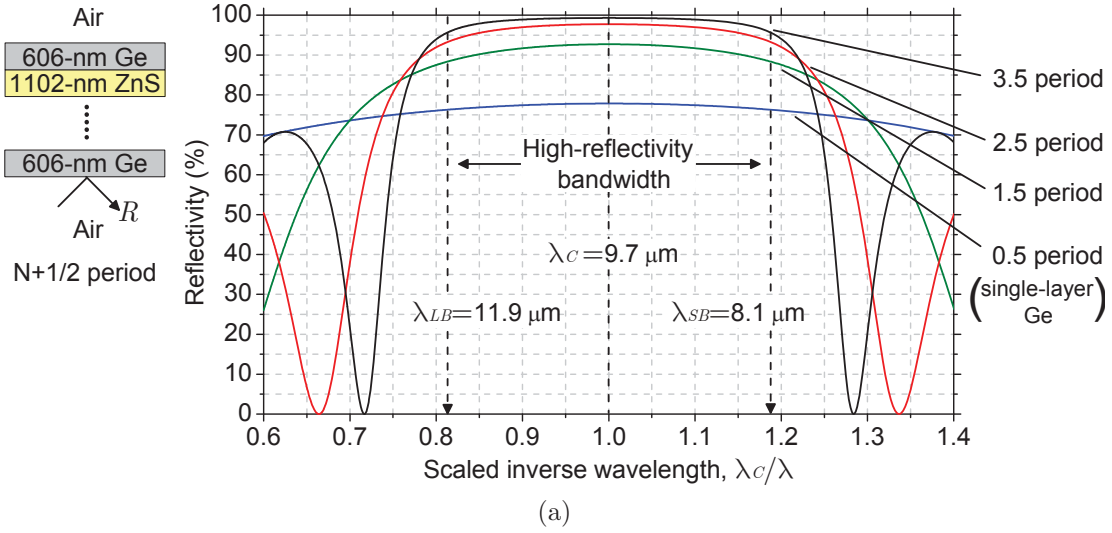

(a)

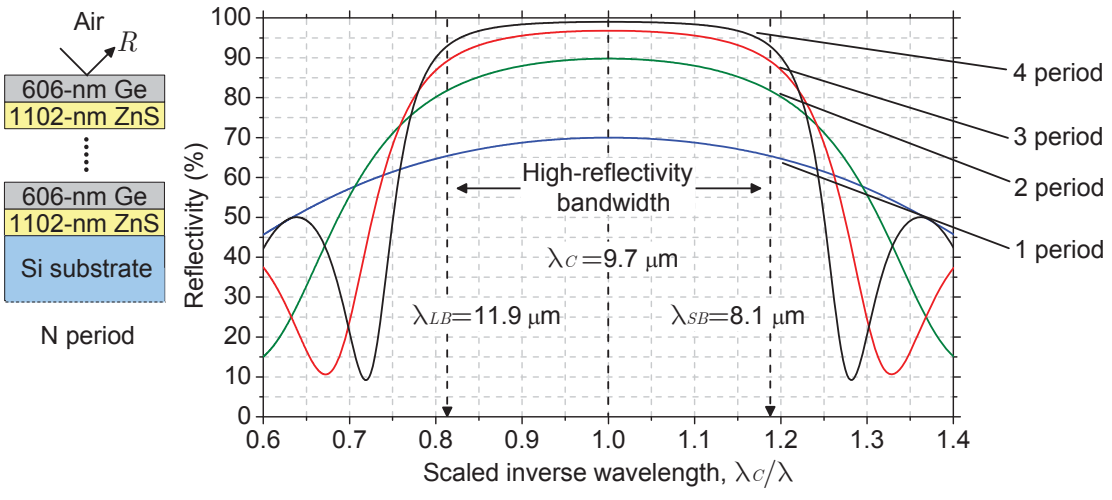

(b)

Figure 3.7: Modelled reflectivity spectra of (a) $N + 1/2$-period Ge/ZnS QWMs suspended in air and (b) N-period Ge/ZnS QWMs on a silicon substrate. Only normal incidence light is considered in this thesis and angled light paths are shown for clarity only.

in the calculation were experimental values, namely $n_{Ge} = 4.0, k_{Ge} = 2 \times 10^{-5}$ and $n_{ZnS} = 2.2, k_{ZnS} = 2 \times 10^{-3}$ (see Chapter 4). The reflectivity curves are plotted against λ_C/λ in order to highlight the even symmetry of QWM reflectivity with inverse wavelength about λ_C (see Equation (3.32)). As evident in Figure 3.7, the mirror reflectivity remains high over the design wavelength range of 8.1-11.9 µm, and approaches unity as the number of Ge/ZnS periods becomes larger.

3.2.5 Design of tunable LWIR FP filters with Ge/ZnS based QWMs

In the design of a tunable LWIR Fabry-Perot filter that employs Ge/ZnS based QWMs, one of the most critical decisions is the number of Ge/ZnS periods to be used in the QWMs. A large number of layer periods is generally considered advantageous because it gives a high mirror reflectivity and thus results in desirable spectral features for the filter, such as high peak transmittance and narrow FWHM. However, for the freely suspended top mirror, a large number of Ge/ZnS periods can also be a disadvantage, since it will result in a relatively thick mirror structure on the order of tens of micrometers. Stress mismatch between the constituent layers in such a thick mirror is particularly common and significant. The imbalanced layer stresses, along with the thermal stresses caused by any thermal expansion mismatch between the different mirror layers during cryogenic cooling of LWIR photodetector arrays, can severely deform the suspended mirror and thus degrade the transmittance of the filter and, in particular, cause pixel-to-pixel transmission peak wavelength non-uniformity across a 2-D imaging FPA. To negate this issue, the top suspended mirror of our tunable LWIR Fabry-Perot filter has been designed to consist of a single quarter-wavelength thick Ge layer. As evident from Figure 3.7a in Section 3.2.4, a single-layer Ge mirror has a high mirror reflectivity of 75-78% over the entire wavelength range of 8-12 µm, because of the high refractive index of Ge. This value exceeds the minimum mirror reflectivity requirement (75%, see Section 3.1.4) for achieving the target FWHM of <1 µm for multispectral thermal imaging applications.

Once the design of the top mirror has been established, mirror reflectivity matching criterion can be applied to establish a design for the bottom mirror. According to this criterion (see Section 3.1.4), the reflectivity of the bottom mirror needs to be larger than 75%, but must not exceed that of the top mirror by more than 20%, in order to preserve a >50% peak transmittance required by multispectral thermal imaging applications. As can be seen in Figure 3.7b, a 2-period Ge/ZnS QWM on

a silicon substrate has a reflectivity of 80-90% over the entire 8-12 µm wavelength range, which satisfies the design criterion and therefore is chosen as the bottom mirror for our tunable LWIR Fabry-Perot filter design.

The complete structure of the tunable LWIR Fabry-Perot filter design is shown schematically in Figure 3.8a. This filter is structurally asymmetric and consists of a single quarter-wavelength thick Ge layer as the top suspended mirror and a four-layer quarter-wave Ge/ZnS/Ge/ZnS stack on a silicon substrate as the bottom mirror. The quarter-wavelength thick Ge and ZnS mirror layers are designed for a central wavelength $\lambda_C = 9.7$ µm and have thicknesses of 606 nm and 1102 nm, respectively. Ideal filter transmittance spectra were calculated using the optical matrix model (Equation (3.38)) for various optical cavity lengths and are presented in

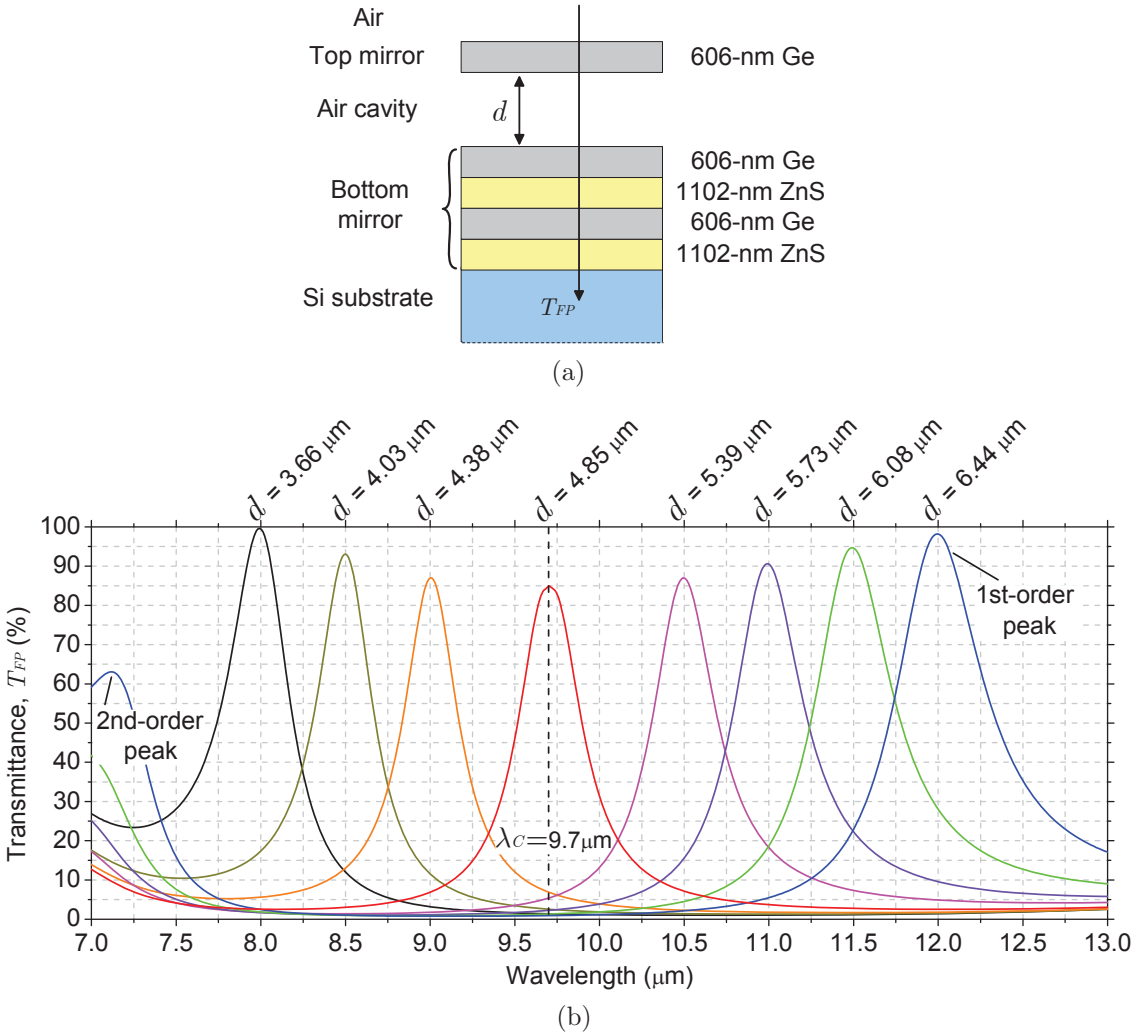

Figure 3.8: (a) Optical layer structure of the tunable LWIR Fabry-Perot filter, and (b) ideal transmittance spectra of the tunable LWIR Fabry-Perot filter for various optical cavity lengths, which were calculated using the optical matrix model; i.e., Equation (3.38).

Figure 3.8b. The optical modelling results indicate that the proposed filter design can achieve a peak transmittance greater than 80% and a FWHM of approximately 500 nm over the entire 8-12 µm wavelength range. Moreover, the filter design features an out-of-band light transmission of approximately 2%, which corresponds to an out-of-band rejection better than 40:1. As can be seen in Table 3.3, these spectral figures exceed the target spectral specifications for multispectral thermal imaging applications, and demonstrate that the proposed LWIR Fabry-Perot filter design is a viable solution, provided that the flatness of the suspended mirror results in a uniform optical cavity that can meet the transmission peak wavelength uniformity requirement. Any flatness deviation of the suspended mirror will affect the optical performance of the designed LWIR Fabry-Perot filter, which will be discussed in Section 3.4.

Table 3.3: Comparison between the spectral characteristics of the proposed LWIR Fabry-Perot filter design shown in Figure 3.8 and the target specifications for multispectral thermal imaging applications.

Parameter	Target	Design
Peak transmittance	$> 50\%$	$> 80\%$
FWHM	0.5-1 µm	$\sim$500 nm
Out-of-band rejection	$> 10{:}1$	$> 40{:}1$

3.2.6 Effect of reflection phase changes of Ge/ZnS QWMs on the optical performance of tunable LWIR Fabry-Perot filters

An important characteristic feature of QWMs is that the phase of the incident light can change significantly upon reflection, as discussed for general dielectric stacks in Section 3.1.1. The reflection phase changes of the Ge/ZnS QWMs have a significant impact on the optical performance of the designed tunable LWIR Fabry-Perot filter, and this will be discussed in detail in this section.

In general, for quarter-wave mirrors, the reflection phase change φ is odd symmetric with inverse wavelength, and is approximately linear with inverse wavelength near the central design wavelength of λ_C [28]. For QWMs with a high-index top layer, either $N + 1/2$-period QWMs suspended in air or N-period QWMs on a substrate whose refractive index is larger than that of the low-index material (layer configurations of the top and bottom QWMs in our LWIR filter design), the reflection phase change φ is π at the central design wavelength λ_C (see Figure 3.5

in Section 3.2.1), and is a monotonically decreasing function of inverse wavelength near λ_C [26].

Based on these initial conditions, the reflection phase change φ near λ_C can be approximated by a linear function

$$\varphi = \left(\frac{1}{\lambda_C} - \frac{1}{\lambda}\right) \frac{\partial \varphi}{\partial\,(1/\lambda)} + \pi, \tag{3.40}$$

or in an alternative form,

$$\varphi = \frac{\pi}{2}\left(1 - \frac{\lambda_C}{\lambda}\right) \frac{\partial \varphi}{\partial \vartheta} + \pi, \tag{3.41}$$

where $\vartheta = \pi\lambda_C/2\lambda$. The analytical form of $\partial\varphi/\partial\vartheta$ was given by Garmire [28] as a function of n_H, n_L, n_S and N. For large N or large n_H/n_L, $\partial\varphi/\partial\vartheta$ simply reduces to

$$\frac{\partial \varphi}{\partial \vartheta} = \frac{2}{n_H - n_L}. \tag{3.42}$$

Substituting Equation (3.42) for $\partial\varphi/\partial\vartheta$ in Equation (3.41), the linear approximation of reflection phase change φ near λ_C can be given as

$$\varphi = \left(1 - \frac{\lambda_C}{\lambda}\right) \frac{\pi}{n_H - n_L} + \pi. \tag{3.43}$$

According to Equation (3.43), the reflection phase change φ_{TM} of the single-layer Ge top mirror in our LWIR Fabry-Perot filter design can be approximated by (air is the low-index material, $n_L = 1$)

$$\varphi_{TM} = \left(1 - \frac{\lambda_C}{\lambda}\right) \frac{\pi}{n_{Ge} - 1} + \pi, \tag{3.44}$$

and the reflection phase change φ_{BM} of the Ge/ZnS/Ge/ZnS bottom mirror can be approximated by

$$\varphi_{BM} = \left(1 - \frac{\lambda_C}{\lambda}\right) \frac{\pi}{n_{Ge} - n_{ZnS}} + \pi, \tag{3.45}$$

where $\lambda_C = 9.7$ µm, $n_{Ge} = 4.0$ and $n_{Ge} = 2.2$, respectively. Figure 3.9 depicts the reflection phase changes of the Ge top mirror and the Ge/ZnS/Ge/ZnS bottom mirror, and compares the linear approximations calculated using Equations (3.44) and (3.45) with the exact values calculated using the optical matrix model; i.e., Equation (3.39). As can be seen in the figure, Equations (3.44) and (3.45) are a good estimate of the reflection phase changes over the entire 8-12 µm wavelength range, and only diverge from the true values by a maximum of 0.02π.

For our LWIR Fabry-Perot filter design, the round-trip reflection phase change within the cavity is the sum of the reflection phase changes of the Ge top mirror

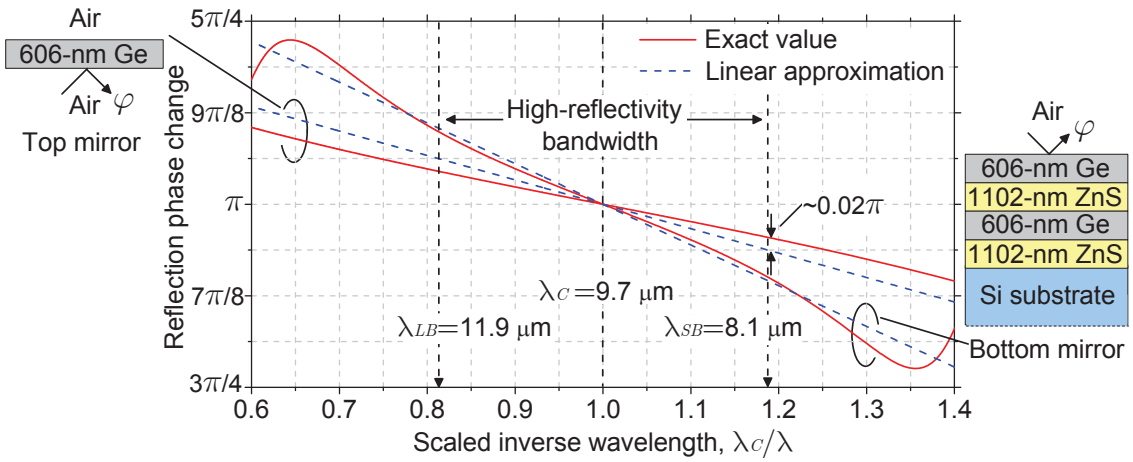

Figure 3.9: Reflection phase changes of the single-layer Ge top mirror and Ge/ZnS/Ge/ZnS bottom mirror on a silicon substrate for the designed LWIR Fabry-Perot filter. The solid lines represent the exact values calculated using Equation (3.39), and the dashed lines represent the linear approximations calculated using Equations (3.44) and (3.45). Only normal incidence light is considered in this thesis; angled light paths are shown for clarity only.

and Ge/ZnS/Ge/ZnS bottom mirror. According to Equations (3.44) and (3.45), the round-trip reflection phase change φ is given by

$$\varphi = \left(1 - \frac{\lambda_C}{\lambda}\right)\left(\frac{\pi}{n_{Ge} - 1} + \frac{\pi}{n_{Ge} - n_{ZnS}}\right) + 2\pi. \tag{3.46}$$

Substituting Equation (3.46) for φ in Equations (3.27), (3.22) and (3.28) in Section 3.1.3 yields

$$\delta\lambda = \frac{\lambda}{F_R\left(m + \frac{1}{2(n_{Ge}-1)} + \frac{1}{2(n_{Ge}-n_{ZnS})}\right)}, \tag{3.47}$$

$$d = \frac{\lambda}{2}m + \frac{1}{2}(\lambda - \lambda_C)\left(\frac{1}{2(n_{Ge} - 1)} + \frac{1}{2(n_{Ge} - n_{ZnS})}\right), \tag{3.48}$$

and

$$\Delta\lambda = \frac{\lambda}{\left(m + 1 + \frac{1}{2(n_{Ge}-1)} + \frac{1}{2(n_{Ge}-n_{ZnS})}\right)}, \tag{3.49}$$

where $\lambda_C = 9.7$ μm, $n_{Ge} = 4.0$, $n_{Ge} = 2.2$, and $m = 1$ for the case of a 1st-order LWIR Fabry-Perot filter design. Equations (3.47), (3.48) and (3.49) describe the influence of the reflection phase changes of Ge/ZnS QWMs on the FWHM, transmission peak position and free spectral range of the designed LWIR Fabry-Perot filter.

For the examination of how the reflection phase changes of Ge/ZnS QWMs affect the FWHM of the designed LWIR Fabry-Perot filter, Figure 3.10 compares the filter

transmittance spectra at the peak wavelength of 9.7 µm, both with and without the inclusion of reflection phase changes, denoted as T_{FP} and T'_{FP}, respectively. T_{FP} was calculated directly from the optical matrix model; i.e., Equation (3.38). T'_{FP} was calculated using the following procedure: the absolute reflectance and transmittance of the Ge top mirror and Ge/ZnS/Ge/ZnS bottom mirror were calculated using the optical matrix model; i.e., Equations (3.37) and (3.38). This allows calculation of T'_{FP} using the general transmission function of a Fabry-Perot filter (i.e., Equation (3.19)), by setting the reflection phase change in Equation (3.19) to zero. The FWHMs associated with T_{FP} and T'_{FP} are given in the figure, and are denoted as $\delta\lambda$ and $\delta\lambda'$, respectively. The extracted value of $\delta\lambda = 450$ nm is smaller than $\delta\lambda' = 560$ nm, indicating that reflection phase changes cause a decrease in the FWHM of the filter. This effect can be understood from Equation (3.47). For the transmission peak in Figure 3.10, Equation (3.47) yields $\delta\lambda = 445$ nm and $\delta\lambda' = 553$ nm, which agree closely with the extracted values.

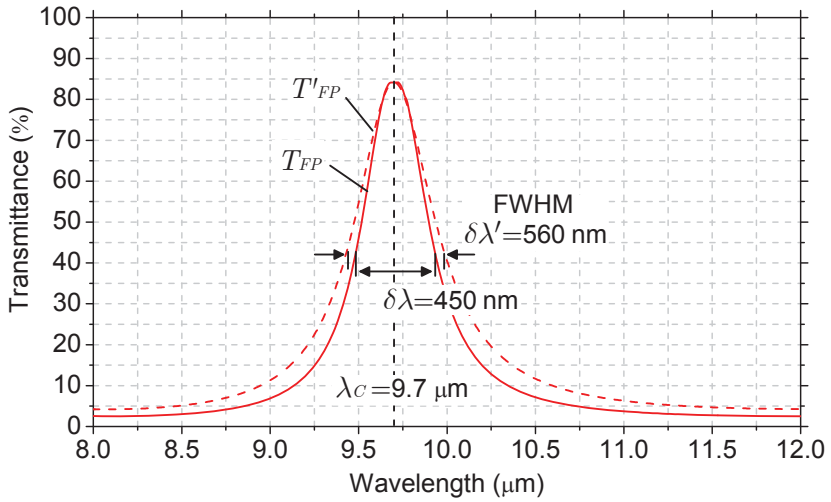

Figure 3.10: Modelled transmittance spectra of the designed LWIR Fabry-Perot filter centered at 9.7 µm. The solid and dashed lines correspond to the spectra with and without the inclusion of mirror reflection phase changes, respectively.

The reflection phase changes of Ge/ZnS QWMs can also shift the transmission peak position of the designed LWIR Fabry-Perot filter. Figure 3.11 shows the transmission peak wavelength of the designed LWIR Fabry-Perot filter as a function of optical cavity length using solid data points. These results were extracted from the modelled transmission tuning spectra in Figure 3.8b and have incorporated the effect of reflection phase changes. For comparison, Figure 3.11 also depicts a plot of $\lambda = 2d$, which represents the expected peak wavelength position of the LWIR Fabry-Perot filter without including the effect of reflection phase changes. As can be seen

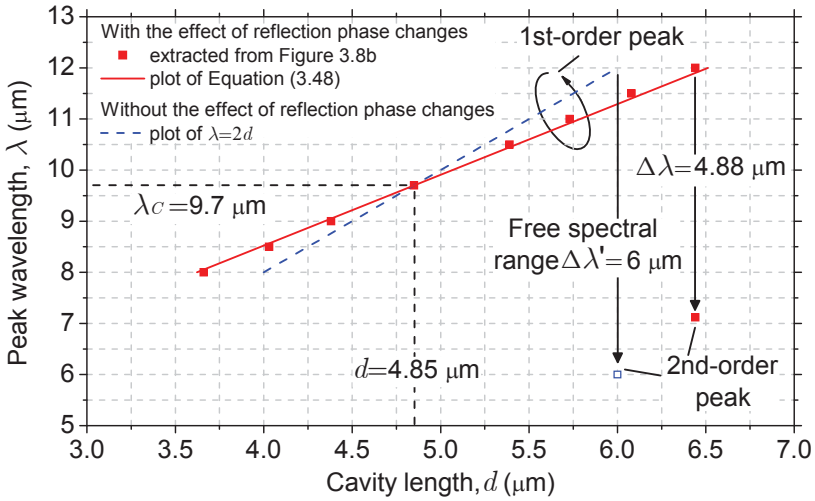

Figure 3.11: Transmission peak wavelength as a function of optical cavity length.

in the figure, when the effect of reflection phase changes is neglected, the 1st-order transmission peak occurs at a wavelength that is exactly double that of the optical cavity length. In comparison, when the effect of reflection phase changes is taken into account, such a transmission peak position is only observed for the wavelength of 9.7 μm, which is the central design wavelength (λ_C) of the Ge/ZnS QWMs. This is because at this particular wavelength, the round-trip reflection phase change within the cavity is 2π (see Equation (3.46)) and it exerts no influence on the cavity resonance conditions. For $\lambda > \lambda_C$, the peak wavelength is shorter than double the cavity length, while for $\lambda < \lambda_C$, the peak wavelength is longer than double the cavity length, due to the different signs of the round-trip reflection phase change in these two regimes. This relationship between the transmission peak wavelength and the optical cavity length can be understood from Equation (3.48). A plot of Equation (3.48) is depicted in Figure 3.11, and a close fit to the extracted data points is demonstrated. Moreover, as can be seen in Figure 3.11, for the case of no reflection phase changes, scanning the peak wavelength from 12 μm to 8 μm requires scanning the cavity spacing from 6 μm to 4 μm. In contrast, the cavity length needs to change from 6.44 μm to 3.66 μm in order to tune the peak wavelength from 12 μm to 8 μm when reflection phase changes are taken into account, which is a 780 nm increase in the required scanning distance.

As shown in Figure 3.11, the designed LWIR Fabry-Perot filter with a 1st-order transmission peak at $\lambda = 12$ μm (corresponding to an optical cavity length of 6.44 μm) has its 2nd-order transmission peak at $\lambda = 7.12$ μm, resulting in a free spectral range of $\Delta\lambda = 4.88$ μm. In comparison, when the effect of reflection phase changes is neglected, the 2nd-order transmission peak is expected to be at $\lambda = 6$ μm, resulting

in a free spectral range of $\Delta\lambda' = 6$ µm. This observation indicates that reflection phase changes reduce the free spectral range of the filter, and can be understood from Equation (3.49). For the 1st-order transmission peak at 12 µm, this equation yields $\Delta\lambda = 4.9$ µm and $\Delta\lambda' = 6$ µm, which agree closely with the extracted values. Despite the appearance of the 2nd-order peak at $\lambda = 7.12$ µm being closer to the LWIR design band, it can still be blocked by an 8-12 µm bandpass "order-sorting" filter, and therefore will not affect the operation of the proposed LWIR Fabry-Perot filter.

3.3 Anti-reflection coating

MEMS-based Fabry-Perot filters are usually fabricated on a thick substrate, and incoherent multiple reflections within the substrate have a significant impact on the transmittance of the filters. This section describes how multiple reflections within the substrate can degrade the transmittance of the designed LWIR Fabry-Perot filter. This section also describes the properties of a ZnS single-layer anti-reflection coating and how such a coating can improve the transmittance of the designed LWIR Fabry-Perot filter on a thick substrate.

3.3.1 Transmittance of a filter-substrate system

In the previous calculation of the transmittance of the designed LWIR Fabry-Perot filter (Figure 3.8b), we assumed an infinitely thick silicon substrate and ignored the effect of multiple reflections within the substrate. However, for a practical evaluation of the design, this effect needs to be taken into account.

Figure 3.12 depicts the designed LWIR Fabry-Perot filter on a substrate of finite thickness. The entire thin-film assembly of the filter is reduced to a single effective interface, characterized by a substrate-side reflectance R^- and transmittance T_{FP}. Similarly, the total filter-substrate system is reduced to a single effective interface with a transmittance of T_{FPS}. Light transmitted through the filter undergoes multiple reflections within the substrate, and the total transmittance of the filter-substrate system T_{FPS} differs from the single-pass value T_{FP}. T_{FPS} can be calculated in a similar manner to Equation (3.18) in Section 3.1.2. By repeating the analysis in Figure 3.2 with I, R and T replacing $\boldsymbol{E}$, $\boldsymbol{\rho}$ and $\boldsymbol{\tau}$, T_{FPS} can be obtained as

$$T_{FPS} = \frac{T_S T_{FP}}{1 - R_S R^-}, \tag{3.50}$$

where R_S and T_S are the surface reflectance and transmittance at the substrate-air interface, given by [26]

$$R_S = \left(\frac{n_S - 1}{n_S + 1}\right)^2 \tag{3.51}$$

and

$$T_S = 1 - R_S, \tag{3.52}$$

respectively, where n_S is the substrate refractive index. Calculation of Equation (3.50) ignores phase. The substrates on which the filters are fabricated usually have thicknesses on the order of several hundred micrometres, which is much greater than the coherence length of the LWIR light in consideration, so that the phase relationships between the multiple reflections within the substrate are not maintained and can be essentially ignored.

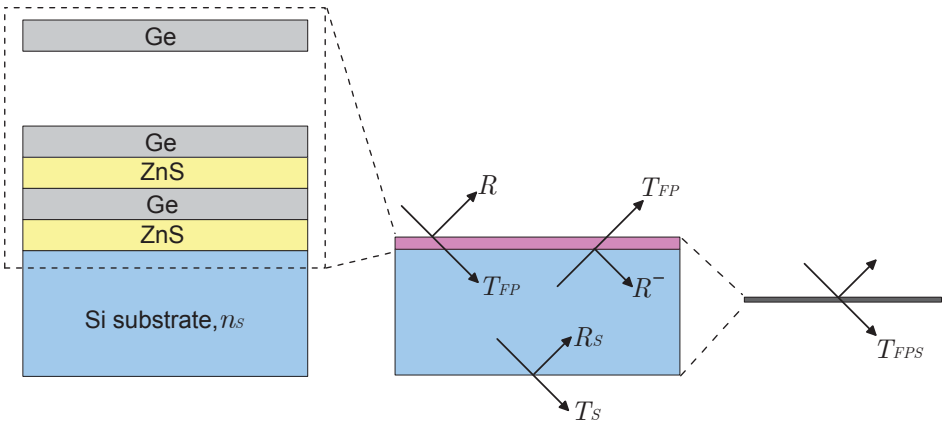

Figure 3.12: For a filter on an optically thick substrate, light transmitted through the filter undergoes multiple reflections within the substrate, and the total transmittance of the filter-substrate system T_{FPS} differs from the single-pass value T_{FP}. Only normal incidence light is considered in this thesis, and angled light paths are shown for clarity only.

The total transmittance through the filter-substrate system, T_{FPS}, can be given in another form by approximating the substrate-side reflectance R^- as $(1 - T_{FP})$, yielding

$$T_{FPS} \approx \frac{T_S T_{FP}}{1 - R_S\,(1 - T_{FP})}. \tag{3.53}$$

This approximation is exact for filters with lossless mirrors [26], and is still a very good approximation for filters with slightly absorbing mirrors, such as the designed LWIR Fabry-Perot filter that employs Ge/ZnS based QWMs. Equation (3.53) implies that the total transmittance through the filter-substrate system is lower than

the transmittance of the filter alone due to multiple reflections within the substrate. In order to reduce the transmission loss associated with reflections within the substrate, an anti-reflection coating is usually employed at the rear surface of the substrate.

3.3.2 Design of a tunable LWIR Fabry-Perot filter with a ZnS single-layer anti-reflection coating

An anti-reflection coating is similar in structure to the QWM presented in Section 3.2.1, and is essentially a thin-film multilayer stack coated onto a thick substrate. However, in contrast to a QWM, an anti-reflection coating relies for its operation on the destructive interference of the light reflected from successive layer interfaces in the stack, and therefore it minimizes rather than maximizes reflectance. The simplest anti-reflection coating consists of a single quarter-wavelength thick layer of transparent material whose refractive index n_f is equal to the square root of the substrate refractive index n_S [26]; i.e.,

$$n_f = \sqrt{n_S}. \tag{3.54}$$

Single-layer anti-reflection coatings give zero reflectance at the central design wavelength and low reflectance for wavelengths in a broad band around the center wavelength.

Solving Equation (3.54) with $n_S = 3.4$ gives $n_f = 1.84$. This indicates that an ideal material for a single-layer anti-reflection coating on silicon should have a refractive index of 1.84. Unfortunately, as can be seen in Table 3.2 in Section 3.2.4, there are no LWIR materials available with exactly this refractive index. However, ZnS is a good compromise because it has the closest refractive index of 2.2 and also has wideband optical transparency over the entire 8-12 µm wavelength range. Therefore, ZnS was chosen as the material for single-layer anti-reflection coating on silicon.

The ZnS single-layer anti-reflection coating is designed for the central wavelength of $\lambda_C = 9.7$ µm and has a quarter-wave thickness of 1102 nm. Figure 3.13 compares the surface reflectance of a silicon substrate with and without a ZnS anti-reflection coating, denoted as R_{ARC} and R_S, respectively. R_{ARC} was calculated using the optical matrix model (Equation (3.37)), and R_S was calculated using Equation (3.51). As can be seen in Figure 3.13, at normal incidence the bare silicon surface reflects 30% of the incident light, while a ZnS anti-reflection coating can reduce this value below 7.5%.

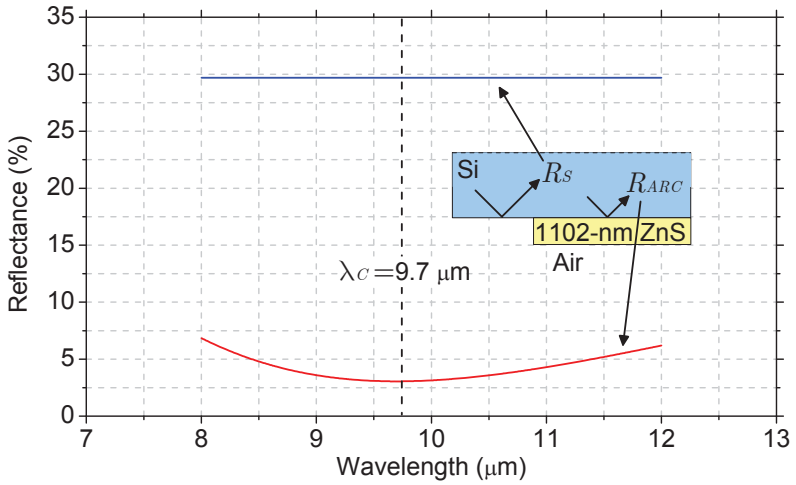

Figure 3.13: Comparison between the surface reflectance of a silicon substrate with and without a ZnS single-layer anti-reflection coating. Only normal incidence light is considered in this thesis and angled light paths are shown for clarity only.

Figure 3.14 shows a comparison between the transmission tuning spectra of the designed LWIR Fabry-Perot filter alone and the filter-substrate system with and without a ZnS anti-reflection coating, denoted as T_{FP}, T_{FPARC} and T_{FPS}, respectively. T_{FP} was calculated directly from the optical matrix model (i.e., Equation (3.38)), allowing the calculation of T_{FPS} using Equation (3.53). T_{FPARC} was calculated in a similar manner to T_{FPS} by replacing R_S in Equation (3.53) with R_{ARC}. By comparing T_{FPS} with T_{FP}, it can be concluded that multiple reflections within the silicon substrate can reduce the peak transmittance of the designed LWIR Fabry-Perot filter by 20-30%. Figure 3.14 also depicts the FWHM associated with T_{FPS} and T_{FP} at the peak wavelength of 9.7 μm, denoted as $\delta\lambda_{FPS}$ and $\delta\lambda_{FP}$, respectively. By comparing $\delta\lambda_{FPS}$ with $\delta\lambda_{FP}$, it can be concluded that multiple reflections within the silicon substrate can also cause a 65 nm increase in the FWHM of the filter. Overall, spectral degradation due to multiple reflections within the silicon substrate is not excessively large, and the resulting transmittance characteristics can still meet the target spectral specifications for LWIR multispectral imaging applications. However, the effect is nonetheless significant, especially for applications where peak transmittance is a critical design parameter. An anti-reflection coating is very useful for achieving optimal spectral performance for a Fabry-Perot filter on a thick substrate. As can be seen in Figure 3.14, a ZnS single-layer anti-reflection coating on the backside of the silicon substrate can significantly improve the transmittance of the LWIR Fabry-Perot filter, resulting in close-to-design spectral characteristics. Therefore, ZnS single-layer anti-reflection coatings were implemented in the MEMS-based LWIR Fabry-Perot filters presented in this thesis.

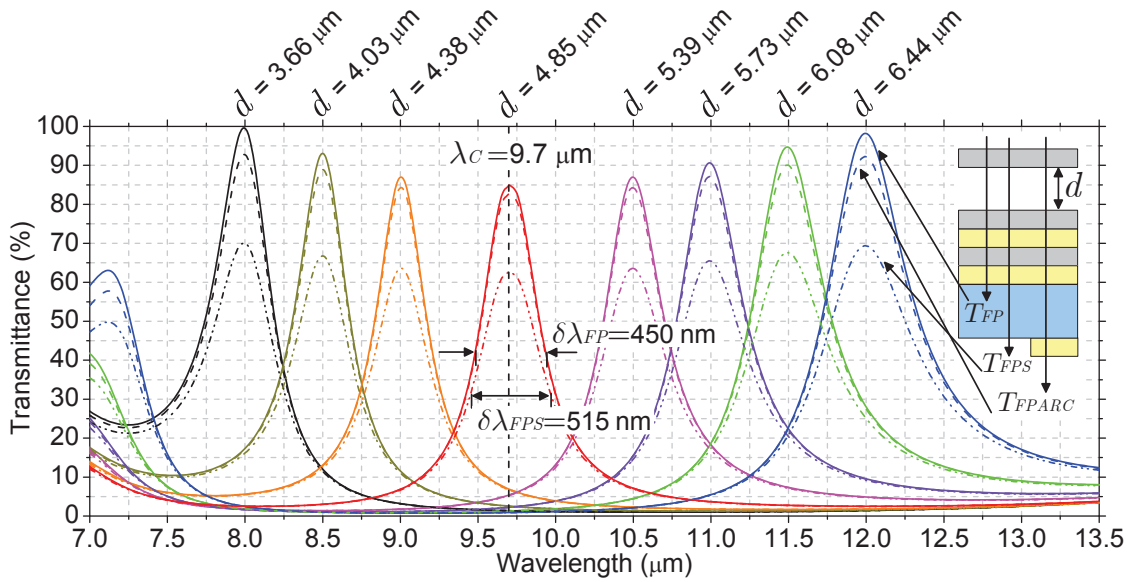

Figure 3.14: Comparison between the modelled transmission tuning spectra of the designed LWIR Fabry-Perot filter alone, and the filter-substrate system both with and without a ZnS anti-reflection coating.

3.4 Effect of top mirror imperfections on the optical performance of a Fabry-Perot filter

So far in our examination of the proposed LWIR Fabry-Perot filter design, we have assumed that the top suspended mirror is ideally flat and also parallel to the bottom fixed mirror. However, in practice, the top suspended mirror may exhibit imperfections such as bowing and tilt. This section presents a general optical modelling approach for calculating the transmittance of a Fabry-Perot filter with top mirror imperfections. This section also examines, in particular, the effect of top mirror bowing on the optical performance of the designed LWIR Fabry-Perot filter.

The transmittance of a Fabry-Perot filter with mirror imperfections can be approximated by segmenting the non-ideal filter into a set of smaller ideal filter elements and summing the transmittance from each ideal filter element [30, 31, 32]. The transmittance of each ideal filter element is weighted by its area relative to the total filter area. As the number of segments approaches infinity, the summation becomes an integration and the calculated transmittance is exact. Figure 3.15 illustrates this concept with the segmentation of a circular-aperture filter with a bowing imperfection in the top mirror. Different filter segments have different cavity lengths and give transmittance spectra at different peak wavelength positions, causing a line broadening of the transmission curve. This indicates that mirror imperfections can reduce the peak transmittance and increase the FWHM of a filter.

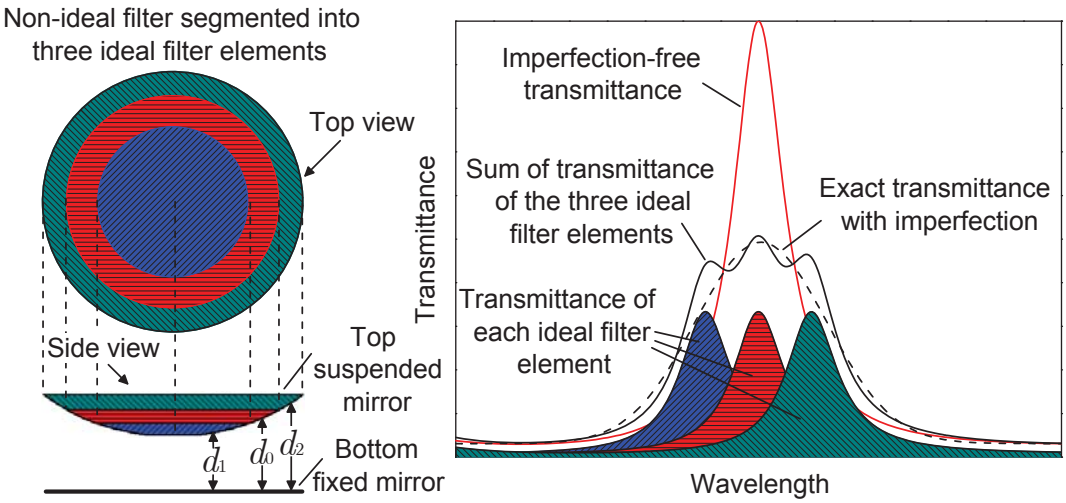

Figure 3.15: Illustration of line broadening of filter transmission curve due to bowing in the top suspended mirror. The overall filter transmittance is approximated by segmenting the non-ideal filter into three ideal filter elements and summing their transmittance, with each transmittance multiplied by one third to account for the area of the individual ideal filter elements.

Figure 3.16 shows how the above concept can be used with the developed optical equations to model the transmittance of a Fabry-Perot filter with arbitrary mirror imperfections. This algorithm was implemented in Labview VIs by Jorge Silva Castillo, a PhD student in our research group. This Labview program is named "*StackSim*" in this thesis for convenience of reference. In addition, "*StackSim*" has an advanced function to import the surface profile image of a filter measured from an optical surface profilometer (Zygo NewView 6K) and automatically execute pixel-level segmentation. Due to the extremely high imaging resolution (in excess of twenty thousand pixels) of the profilometer, the number of pixel segments is more than sufficient to allow accurate modelling of the transmittance of fabricated MEMS-based Fabry-Perot filters. Another significant advantage of this function is that since it uses the actual measured mirror imperfection profile, it simultaneously takes into account all types of imperfections present in the mirror in calculating the transmittance of the filter. The extensive use of this advanced function of "*StackSim*" can be found in Chapter 5 and Chapter 6.

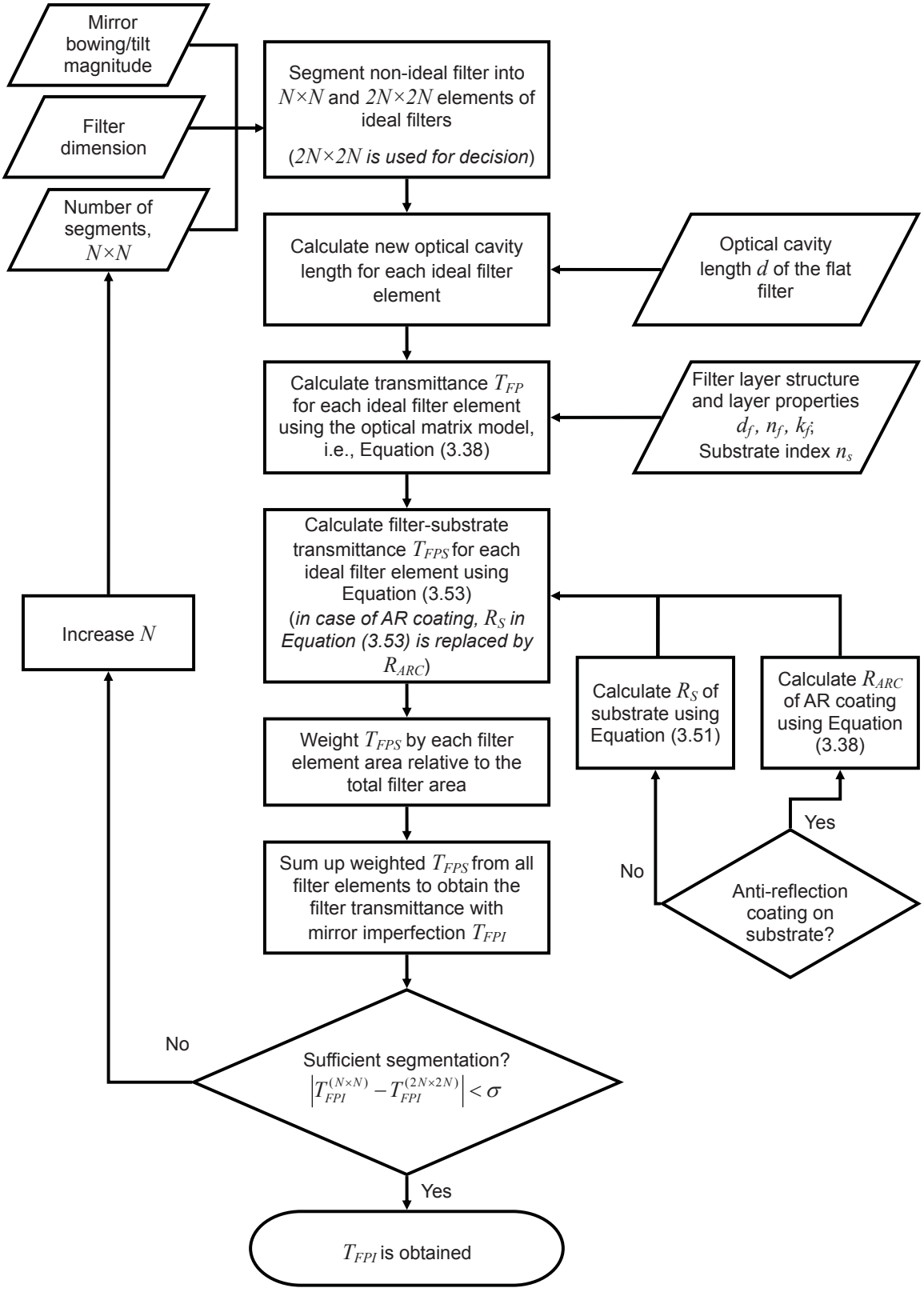

Figure 3.16: Flow chart describing the algorithm for the optical modelling approach ("*StackSim*" program) used in this thesis for calculating the transmittance of a Fabry-Perot filter with mirror imperfections.

Bowing is particularly common in thin-film dielectric mirrors due to vertical mirror stress gradients, and is also the type of mirror imperfection encountered in the devices presented in this thesis. In order to evaluate the LWIR Fabry-Perot filter design, "*StackSim*" was employed to model the total-area transmittance of a 200-µm dimension filter for various mirror bowing magnitudes ranging from $\delta d = 0$ nm to 500 nm, and the results are shown in Figure 3.17. It can be seen that as the mirror bowing magnitude increases, the peak transmittance and FWHM of the filter are significantly degraded, consistent with the general discussions at the beginning of this section.

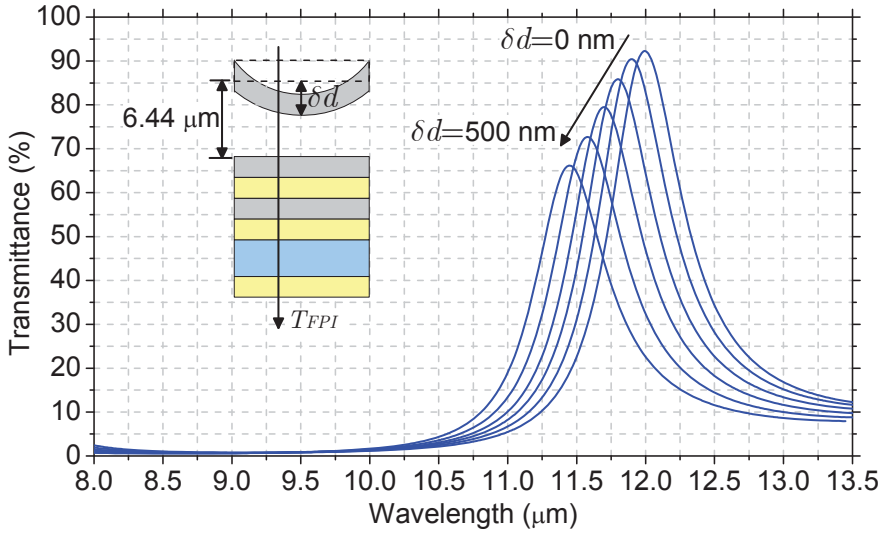

Figure 3.17: Total-area transmittance of the designed LWIR Fabry-Perot filter for various mirror bowing magnitudes, calculated using the "*StackSim*" program.

As described in the introduction chapter, the MEMS-based LWIR Fabry-Perot filters presented in this thesis will eventually be hybridized with a 2-D imaging focal plane array to form a multispectral thermal imaging system. Under this application scenario, the influence of mirror bowing on the filter's on-pixel spectral performance becomes a critical concern. "*StackSim*" was used to model the on-pixel transmittance of the designed LWIR Fabry-Perot filter using a 20 µm × 20 µm pixel area at the filter center and edge for various mirror bowing magnitudes, and the results are shown in Figure 3.18. It can be seen that the on-pixel transmittance characteristics are ideal regardless of the magnitude of top mirror bowing, including a peak transmittance higher than 80%, a FWHM of approximately 500 nm, and an out-of-band rejection better than 40:1. This is because the individual pixels only "see" a very small area of the Fabry-Perot filter, and any large-area mirror bowing will not result in a transmission peak decrease or FWHM broadening on the pixel

level. However, large-area mirror bowing can cause a variability of the optical cavity length across the filter, which will translate into a pixel-to-pixel variation of transmission peak wavelength across the imaging array. It can be seen in Figure 3.18 that for the proposed LWIR Fabry-Perot filter design, the maximum tolerable mirror bowing magnitude is 300 nm in order to achieve the required <4% peak wavelength uniformity specification. Realizing this fact is very important for the successful development of MEMS-based LWIR Fabry-Perot filters: if the bowing magnitude of the released top suspended mirror in a fabricated filter is measured to be larger than 300 nm, the filter can be assumed unusable, and necessary stress control mechanisms will need to be incorporated into the fabrication process to reduce the bowing; or if such a bowing magnitude is developed on the suspended top mirror during filter actuation, it should be recognized that the filter has a limited usable tuning range.

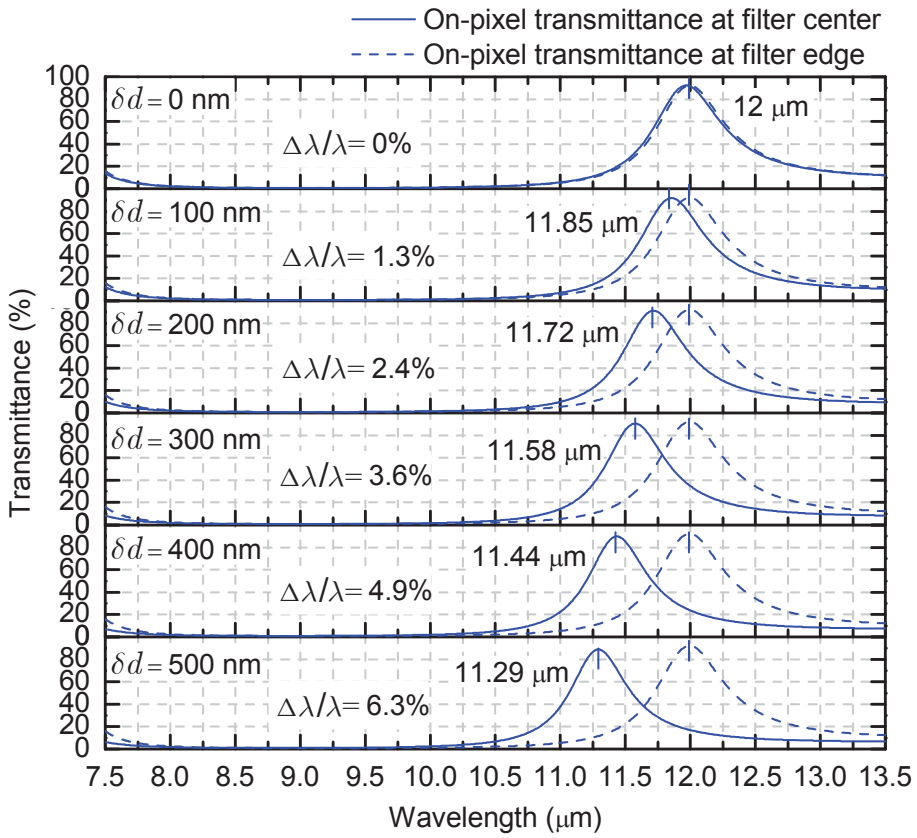

Figure 3.18: On-pixel transmittance of the designed LWIR Fabry-Perot filter over a 20 μm × 20 μm pixel area at the filter center and edge for various mirror bowing magnitudes, calculated using the "*StackSim*" program. $\Delta\lambda/\lambda$ represents the relative change of the transmission peak wavelength across the filter, where λ is the transmission peak wavelength for the pixel at the filter center and $\Delta\lambda$ is the difference between the peak wavelengths for the pixels at the filter center and edge.

Summary

This chapter has discussed fundamental Fabry-Perot theory, and has employed the theory for the optical design of MEMS-based tunable LWIR Fabry-Perot filters. The transmittance of an ideal Fabry-Perot filter was derived using a multiple beam interference concept, and mirror reflectivity requirements for achieving the filter spectral characteristics that can meet the specifications of multispectral thermal imaging applications were established. The theory of quarter-wave mirrors has been discussed and used in conjunction with the mirror reflectivity requirements to design the Ge/ZnS based quarter-wave mirrors for LWIR Fabry-Perot filters. To avoid stress-gradient induced mirror bowing, the LWIR Fabry-Perot filter was designed to consist of a single quarter-wavelength thick Ge layer as the top suspended mirror and a four-layer quarter-wave Ge/ZnS/Ge/ZnS stack on a silicon substrate as the bottom mirror. Transmission tuning spectra of the designed LWIR Fabry-Perot filter were calculated using the optical matrix model, demonstrating that this filter design can achieve consistent transmittance characteristics over the entire 8-12 µm range, namely a peak transmittance of higher than 80%, a FWHM of approximately 500 nm and an out-of-band rejection of greater than 40:1, all of which exceed the target spectral specifications for multispectral thermal imaging applications. Subsequently, filter transmittance degradation as a result of multiple reflections within the thick silicon substrate was studied. In order to reduce the transmission loss caused by reflections within the substrate, a ZnS single-layer anti-reflection coating was designed. Lastly, an optical modelling approach for calculating the transmittance of a Fabry-Perot filter with top mirror imperfections was developed. To evaluate the LWIR Fabry-Perot filter design, this approach was used to model the on-pixel filter transmittance for various mirror bowing magnitudes. It was shown that the maximum acceptable top mirror bowing for the proposed LWIR Fabry-Perot filter design is 300 nm in order to achieve the <4% pixel-to-pixel transmission peak wavelength uniformity specification required for multispectral thermal imaging applications.

Chapter 4

Deposition and characterization of Ge and ZnS thin films

This chapter firstly describes the preparation of durable Ge and ZnS thin films used for the construction of MEMS-based LWIR Fabry-Perot filters, and subsequently presents the experimental procedures used for characterization of Ge and ZnS thin film optical properties. Techniques for evaluation of thin film stress properties are then briefly reviewed, followed by the application of these techniques to characterize the residual stress in Ge and ZnS thin films.

4.1 Ge and ZnS thin film deposition

There are a number of techniques that can be used for the deposition of solid thin films [26]. The most commonly used approach is physical vapor deposition (PVD). The main principle of the PVD technique is the creation of a vapor phase from a solid source material, which condenses on a surface and results in the creation of a solid thin film. Because there is no chemical reactions taking place during film formation in the PVD process, the created film is composed of the same chemical species as the source material. Electron-beam evaporation and thermal evaporation are two of the most widely used PVD processes because of their simplicity and relatively low cost. Figure 4.1 schematically shows thin film deposition via electron-beam evaporation, where the source material is contained in a crucible and is bombarded with a beam of electrons to cause heating and evaporation (boiling off or sublimating) within a vacuum enclosure. Thermal evaporation is a process similar to electron-beam evaporation, but during thermal evaporation the source material is evaporated by resistive heating of a source containing boat. In both methods, the deposition of the evaporated material proceeds via line-of-sight impingement on the substrate.

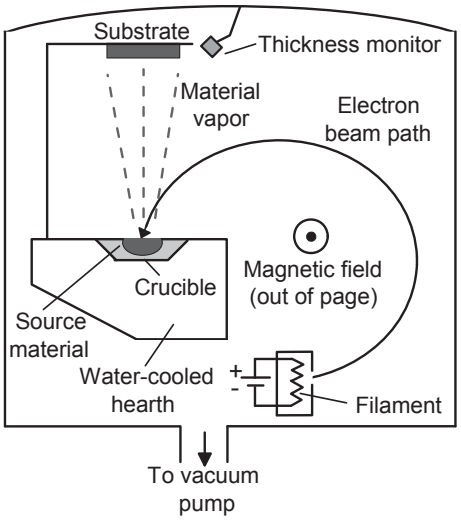

Figure 4.1: Schematic diagram of an electron-beam evaporation system.

In previous studies, we had used thermal evaporation to deposit Ge films. It was found that Ge films could be easily contaminated by the evaporation boat and exhibited a low refractive index in the short-wavelength infrared range [33, 34]. The influence of this contamination was not explicitly examined in the long-wavelength infrared range, but high optical absorption can be reasonably assumed. In this thesis, electron-beam evaporation (BOC Edwards Auto 500 Systems) was used as an alternative to thermal evaporation to deposit Ge thin films, since this technique has the advantage that an inert graphite crucible can be used. In addition, the electron beam only heats a small central portion of the exposed source material and not the entire crucible, preventing any contamination from the crucible.

Deposition of ZnS thin films was performed in a separate dedicated thermal evaporator to avoid cross-contamination of Ge films with sulfur. The boat used for ZnS evaporation was a baffled box made of Tantalum [35], which is especially designed to eliminate the possibility of material spitting and streaming that can cause pinhole type film defects.

High purity Ge (99.999 wt% purity) and ZnS (99.99 wt% purity) sources were used for evaporation. Deposition was initiated at a base pressure of 10^{-7} Torr, and during deposition the chamber pressure was maintained on the order of 10^{-6} Torr. For quality coatings, low deposition rates of 0.5 nm/s and 0.2 nm/s were used for Ge and ZnS, respectively.

Material durability of both electron-beam evaporated Ge films and thermally evaporated ZnS films is a concern for both the filter fabrication process and the long-term stability and operation of the fabricated device. In order to successfully fabricate fully functional devices, the films need to withstand multiple exposures

to both de-ionized (DI) water and the alkaline-based photoresist developer used in photolithography. Initially, Ge and ZnS films were deposited onto Si substrates at room temperature (20 °C). Whereas Ge films deposited at room temperature showed excellent durability under exposure to DI water and alkaline developer, the ZnS films deposited at room temperature were found to delaminate immediately upon contact with these chemicals.

In this work, we have examined the effect of substrate heating during thin film deposition on the adhesion of ZnS films to Si and Ge substrates. Si and Ge substrates were chosen because they are the materials on which ZnS deposition takes place for LWIR bottom mirror formation (see Section 3.2.5). Prior to deposition, the substrates underwent a series of solvent washes followed by ultrasonic cleaning. ZnS layers of 1 µm thickness were deposited onto the substrates with the substrate temperature during deposition maintained at either 50 °C, 100 °C, 150 °C, 200 °C or 300 °C. To test the durability of these ZnS films, the samples were submerged in DI water and AZ400K developer, and the time taken to observe any evidence of delamination or cracking was recorded. The entire experimental procedure was repeated twice, and the same results were obtained, as shown in Table 4.1.

Table 4.1: Durability of 1 µm thick ZnS films prepared at different substrate deposition temperatures.

Substrate temperature (°C)	The time taken to observe any delamination	
	In DI water	In AZ400K
50	immediately	immediately
100	5 mins	2 mins
$\geq$ 150	$>$ 2 days	$>$ 2 days

As evident from Table 4.1, the durability of ZnS films deposited at substrate temperatures of 150 °C or higher is significantly improved in comparison to films deposited at 100 °C and below. Such a dramatic improvement can be attributed to the higher surface mobility of adatoms during deposition at higher substrate temperatures, which improves the packing density and overall quality of the films [36, 37]. In addition, thermal cycling experiments were conducted for the ZnS films deposited at 150 °C or higher by dipping these films into 77 K liquid nitrogen and 60 °C DI water repeatedly, and these films exhibited excellent durability and no delamination was observed up to 400 cycles. In this work, a substrate temperature of 150 °C was used for ZnS film deposition, and higher temperatures were avoided in order to minimize the thermal load imposed on the fabricated devices. Table 4.2 summarizes the optimized deposition conditions for Ge and ZnS films.

Table 4.2: Optimized deposition conditions for Ge and ZnS films.

	Deposition method	Chamber pressure	Deposition rate	Substrate temperature during deposition
Ge	Electron-beam evaporation	$\sim 10^{-6}$ Torr	0.5 nm/s	Room temperature (20 °C)
ZnS	Thermal evaporation	$\sim 10^{-6}$ Torr	0.2 nm/s	150 °C

4.2 Measurement of Ge and ZnS thin film optical properties

In order to establish that the deposited films have appropriate LWIR properties, the optical constants of the Ge films deposited at room temperature and the ZnS films deposited at 150 °C were measured in the LWIR band of 8-12 µm. Although a variety of methods are available in our lab for determining the optical constants of thin films, such as ellipsometry [38] and film reflectance/transmittance measurements (Filmetrics) [39], they are not able to do LWIR measurement. We have chosen to investigate approaches that are compatible with our existing LWIR measurement capabilities, which rely on LWIR transmittance spectra alone. Swanepoel et al. [40] reported on the use of fringe patterns of the transmittance spectrum to calculate the optical constants of thin films; however, the primary technical challenge that prevents us from adopting this approach is the requirement to deposit very thick films to produce a sufficient number of fringes in the LWIR band. In this work, we have implemented an optical matrix model based iterative fitting of transmittance spectrum to derive the LWIR optical constants of Ge and ZnS thin films.

Two multilayer structures, as depicted in Figure 4.2a, consisting of multiple layers of Ge/ZnS on the front side and a single layer of ZnS on the backside of silicon substrates, were fabricated for the purpose of determining the optical constants of the thin film layers. The substrates used in these structures were LWIR transparent float-zone (FZ) silicon wafers, since conventional Czochralski (CZ) silicon wafers exhibit strong LWIR absorption due to excessive oxygen content [41]. Apart from the middle Ge layer that was either 1700 nm or 1300 nm thick, which forms the optical cavity of the Fabry-Perot filter, all other Ge and ZnS layers that form the top and bottom mirrors were 600 nm and 1100 nm thick, respectively.

Each of these two structures is essentially a Fabry-Perot filter on a thick substrate with a backside anti-reflection coating. The optical modelling approach for calculating the transmittance of such a configuration was previously described in

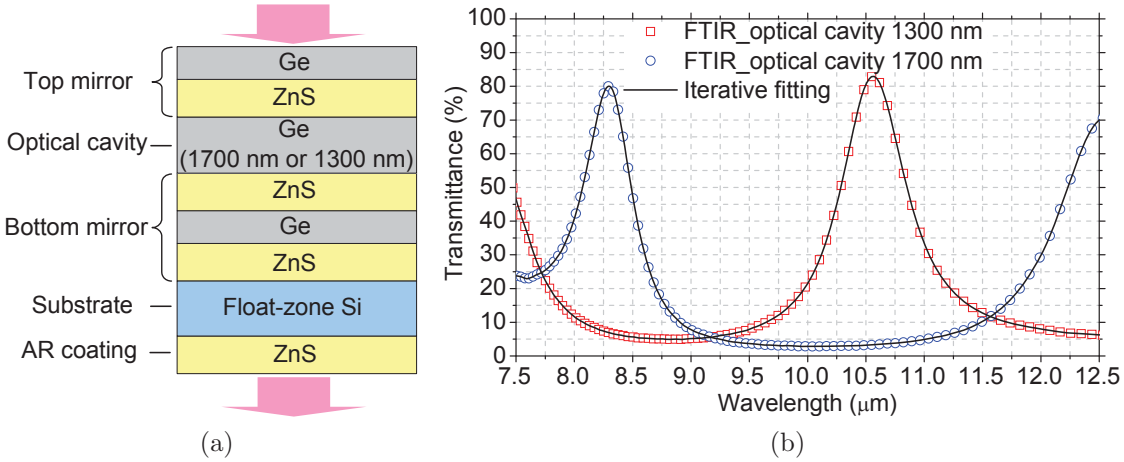

Figure 4.2: (a) Layered structures used for determination of optical constants. The Ge and ZnS layers had thicknesses of 600 nm and 1100 nm, respectively, except for the middle Ge layer which forms the optical cavity and was either 1700 nm or 1300 nm thick. (b) Transmittance measured by FTIR (open data points) and the best fit to the transmittance using an iterative procedure (solid lines).

Section 3.3 of Chapter 3. Knowing the optical constants of all layers, the optical matrix model can be used to calculate the transmittance of the filter thin-film assembly and the reflectance of the anti-reflection back-coated substrate using Equation (3.38) and Equation (3.37), respectively, allowing calculation of the transmittance of the entire filter-substrate system using Equation (3.53). In this work, we carried out a reverse analysis of this approach to extract the unknown optical constants of the Ge and ZnS films based on the experimentally measured transmittance. Using the transmittance of a multilayer structure, rather than that of a single layer, allows the optical constants of Ge and ZnS films to be extracted simultaneously.

Transmittance spectra for these two structures were measured by Fourier transform infrared spectroscopy (PerkinElmer Spectrum One FTIR Spectrometer), and are shown in Figure 4.2b. The multilayer structure with a 1700 nm thick Ge layer as the optical cavity exhibited a second-order peak transmittance of 80% at the peak wavelength of 8.25 μm and a FWHM of 500 nm. In comparison, for the structure with 1300 nm thick Ge layer as the optical cavity, the first-order peak transmittance and the FWHM were measured to be 85% at the peak wavelength of 10.5 μm and 750 nm, respectively. The measured high peak transmittance indicates that both the deposited Ge and ZnS films are highly transparent in the LWIR range.

A least-squares approach was implemented using Matlab code to fit Equation (3.53) to the measured transmittance data of the two fabricated multilayer structures. During the fit, refractive indices and extinction coefficients of Ge and ZnS thin film layers were iteratively varied, and layer thicknesses were fixed. Since both

Ge and ZnS exhibit low dispersion in the LWIR band [42, 43], it was assumed that the refractive indices and extinction coefficients of the investigated materials are constant over the entire LWIR range. When a goodness of fit of 99.9% was achieved, the optical constants of the electron-beam evaporated Ge and thermally evaporated ZnS were determined. Each multilayer structure determined one set of optical constants. The optical constants obtained from the two multilayer structures were in excellent agreement. The refractive indices of the fabricated Ge and ZnS thin films were measured to be 4.0 and 2.2, respectively, showing high refractive index contrast. The extinction coefficients of Ge and ZnS thin films were measured to be 2×10^{-5} and 2×10^{-3}, respectively, showing excellent LWIR transparency. Table 4.3 compares these extracted optical constants with other published data.

Table 4.3: Optical constants of Ge and ZnS thin films at a wavelength of 10 µm. Note that the refractive indices (n) and extinction coefficients (k) of the Ge and ZnS films in this work were assumed constant over the entire 8-12 µm range.

	Ge			ZnS		
	This work	Donovan [44]	Potter [42]	This work	Hall [45]	Addamiano [43]
n	4.0	3.98	4.0	2.2	2.17	2.2
k	2×10^{-5}	0	0	2×10^{-3}	1×10^{-3}	8×10^{-6}

4.3 Measurement of Ge and ZnS thin film stress properties

Thin film stress is of critical importance for the successful development of MEMS-based Fabry-Perot filters. The presence of excessive stress levels, stress gradients, or overall stress imbalance in the suspended structure may lead to tilt, warp, collapse, rupture and/or deformation of the top suspended membrane or mirror, resulting in optical performance degradation. This section presents a brief review of stress measurement techniques, and describes how these techniques were employed to characterize the stress properties of electron-beam evaporated Ge and thermally evaporated ZnS thin films used for the construction of MEMS-based LWIR Fabry-Perot filters presented in this thesis.

4.3.1 Thin film stress measurement techniques

To a first-order approximation, residual stress in a thin film can be considered to comprise the mean stress component, which represents the averaged stress across the thickness of the film, and the gradient stress component, which represents variation

of stress through the thickness of the film. Full examination of thin film stress properties includes precise determination of these two quantities.

The most commonly used technique for measuring the mean stress of a thin film is the substrate bending method. A bi-layer system consisting of a substrate supporting an overlying thin film with a in-built residual stress, as depicted in Figure 4.3, will deform in a concave (bending downwards in the center) or convex (bending upwards in the center) manner as the thin film tends to contract or expand in order to relax its tensile or compressive stress, respectively. Therefore, the substrate bending direction discloses the tensile or compressive state of the thin film mean stress, and the substrate radius of curvature, R_c, can be used to calculate the magnitude of the stress, σ, according to the Stoney formula [46]:

$$\sigma = \frac{E_s}{6R_c\left(1-\upsilon_s\right)}\frac{d_s^2}{d_f}, \tag{4.1}$$

where d_f is the thickness of the film, and E_s, υ_s and d_s are the uniaxial Young's modulus, Poisson ratio and thickness of the substrate, respectively.

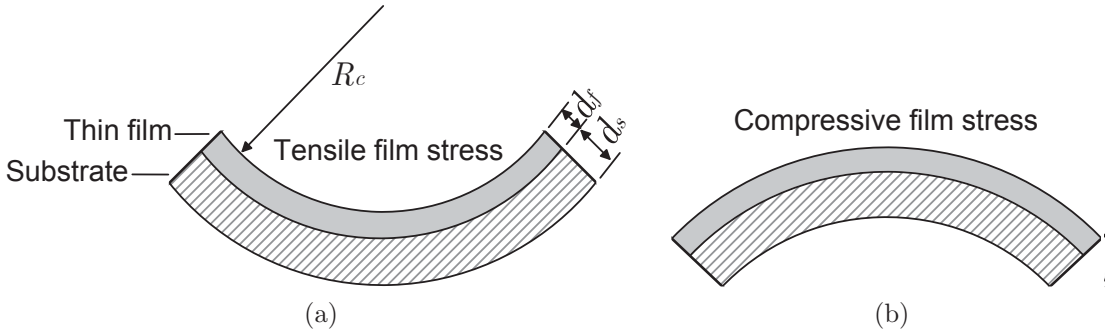

Figure 4.3: Schematic of the bi-layer system consisting of a substrate supporting an overlying thin film, whose vertical deformation is directly related to the mean stress of the film. (a) and (b) show the substrate centrally downward and upward bending resulting from the thin film tensile and compressive stress, respectively.

An alternative approach to determine thin film mean stress is to use diagnostic microstructures. The doubly clamped beam (or microbridge), as depicted in Figure 4.4, is sensitive to compressive stress. When the doubly clamped beam is released from the substrate, relaxation of the thin film compressive stress tends to expand the structure, resulting in buckling of the beam either upwards or downwards. The profile of the vertical displacement, y, of a doubly clamped thin film beam of original length L at a distance, x $(0 \leq x \leq L)$, relative to one of the microbridge support points, can be expressed as [47]

$$y\left(x\right) = \frac{\delta}{2}\left(1 - cos\frac{2\pi x}{L}\right), \tag{4.2}$$

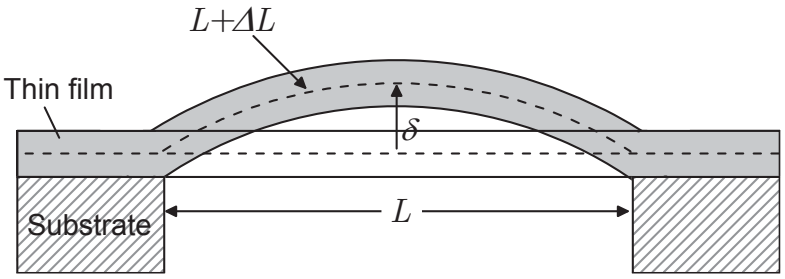

Figure 4.4: Schematic of the doubly clamped beam diagnostic microstructure, whose vertical deformation is directly related to the magnitude of the thin film compressive stress.

where δ is the maximum buckling amplitude at $x = L/2$. Once δ is determined, Equation (4.2) can be used to extract the expanded length of the microbridge, ΔL. The resulting strain in the released thin film, $\Delta L/L$, is related to the magnitude of compressive stress in the unreleased film, σ, via

$$\sigma = E_f \frac{\Delta L}{L}, \tag{4.3}$$

where E_f is the uniaxial Young's modulus of the film.

The microbridge is not suitable for measuring tensile film stress, because the beam will flatten under tension and remain flat irrespective of the magnitude of tensile stress. For the quantitative determination of tensile film stress, a ring-and-crossbeam microstructure should be used, as depicted in Figure 4.5. This structure, once released from the substrate, is free to deform and relieve the tensile stress in the direction perpendicular to the anchors, resulting in elongation of the ring and hence the out-of-plane buckling of the crossbeam. The magnitude of crossbeam contraction, $\Delta L_{contraction}$, is related to the magnitude of ring expansion, $\Delta L_{expansion}$, via

$$\Delta L_{contraction} = \Delta L_{expansion} \cdot g, \tag{4.4}$$

where g is the ratio of contraction to expansion for the ring-and-crossbeam structure, and is given by [48]

$$g = -\frac{2b_r f_2}{2b_r f_1 + b_b f_1^2 - b_b f_2^2}, \tag{4.5}$$

where

$$f_1 = \frac{R}{e}\left(\frac{\pi}{4} - \frac{2}{\pi}\right) - \frac{2e}{\pi R} + \frac{4}{\pi} - \frac{\pi}{4} + \pi k \frac{1+\upsilon_f}{2}, \tag{4.6}$$

$$f_2 = \frac{R}{e}\left(\frac{1}{2} - \frac{2}{\pi}\right) - \frac{2e}{\pi R} - \frac{1}{2} + \frac{4}{\pi} - k\left(1+\upsilon_f\right), \tag{4.7}$$

$$e = R - \frac{b_r}{\ln\left(R_o/R_i\right)}, \tag{4.8}$$

and

$$R = \frac{R_o + R_i}{2}, \tag{4.9}$$

where k is the cross-section form factor, which is equal to 1.2 for a solid rectangle, υ_f is the Poisson ratio of the thin film, b_r and b_b are the widths of the ring and the crossbeam, respectively, and R_o (R_i) is the outer (inner) radius of the ring. Similar to the microbridge case, the vertical displacement profile of the crossbeam can be accurately approximated by a sinusoidal waveform (Equation (4.2)) and then can be translated into crossbeam contraction $\Delta L_{contraction}$, which allows for the determination of ring expansion $\Delta L_{expansion}$ using Equation (4.4). With the knowledge of the uniaxial Young's modulus of the thin film material, E_f, the value of tensile stress in the unreleased film, σ, can then be obtained via

$$\sigma = E_f \frac{\Delta L_{expansion}}{2R}. \tag{4.10}$$

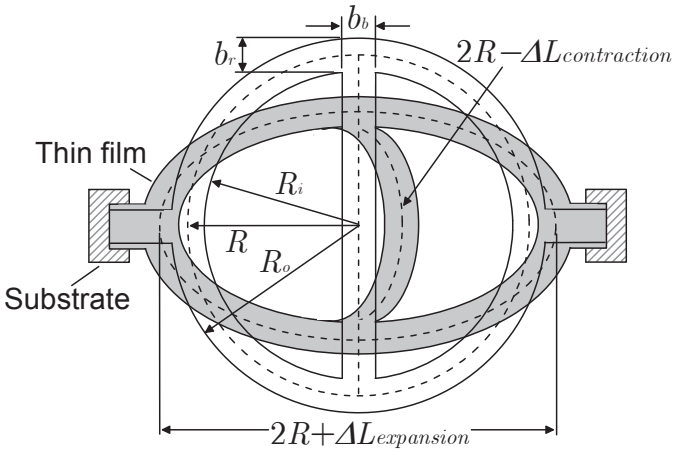

Figure 4.5: Schematic of the ring-and-crossbeam diagnostic microstructure, where out-of-plane buckling of the crossbeam is directly related to the magnitude of the thin film tensile stress.

The main advantage of using diagnostic microstructures for mean stress measurement is that the probed dimension is of the same scale as the structures used for actual devices, and this provides a means of measuring the local stress. However, quantitative determination of stress requires prior knowledge of the Young's modulus of the thin film material. In addition, fabrication of diagnostic microstructures adds complexity, which is compounded by the requirement to ensure no stress is introduced by the sacrificial layer or any other fabrication process. In comparison, the wafer curvature method is simple, independent of the thin film elastic properties, and also not related to post-deposition processing, but it can only give an average stress value across the entire sample.

The stress gradient across the thickness of the thin film can be determined by considering the deflection of microcantilevers as depicted in Figure 4.6. When the cantilever is released from the substrate, the amount of expansion (or compression) necessary for stress relief varies across the thickness of the cantilever due to the presence of a stress gradient in the deposited film. Depending on whether the residual stress of the unreleased film is more tensile (positive stress gradient) or more compressive (negative stress gradient) with increasing film thickness, the released structure curls upwards or downwards, respectively. While the cantilever bending direction discloses the positive or negative state of the thin film stress gradient, the cantilever deflection magnitude can be utilized for quantitative determination of the stress gradient via [49]

$$\sigma' = \frac{E_f}{R_c} \tag{4.11}$$

or

$$\sigma' = \frac{E_f h d_f}{L^2}, \tag{4.12}$$

where E_f is the uniaxial Young's modulus of the film, R_c is the radius of curvature of the cantilever, d_f and L are the thickness and length of the cantilever, respectively, and h is the vertical deflection of the cantilever tip.

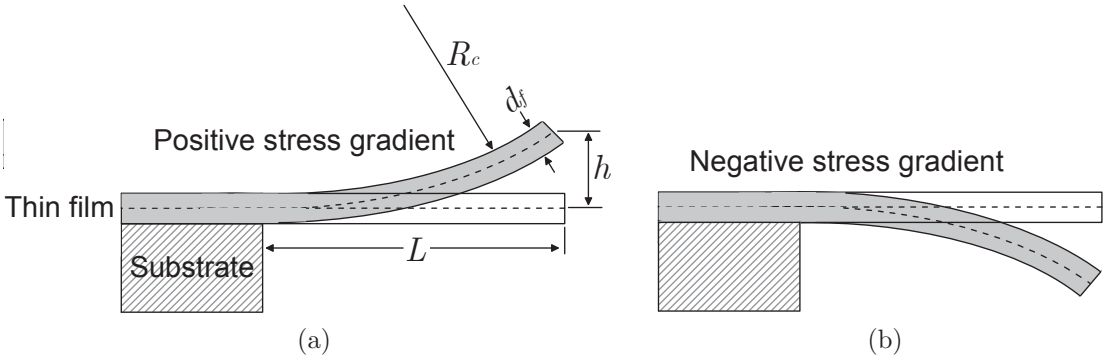

Figure 4.6: Schematic of the cantilever diagnostic microstructure, whose vertical deformation is directly related to the variation of thin film residual stress across the film thickness. (a) and (b) show the upward and downward curl resulting from a positive stress gradient (i.e., residual stress is more tensile with increasing film thickness) and a negative stress gradient (i.e., residual stress is more compressive with increasing film thickness) in the unreleased thin film, respectively.

4.3.2 Thin film stress of fabricated Ge and ZnS layers

The thin film stress induced substrate bending technique was used to characterize the mean stress of the fabricated Ge and ZnS layers. For each material, a series of five films from different deposition runs were fabricated on 1 cm × 1 cm square

100-µm thick silicon <100> wafers. Ge and ZnS films were deposited using the deposition conditions established in Section 4.1 (see Table 4.2), with the target quarter-wave thicknesses of 606 nm for Ge and of 1102 nm for ZnS, respectively. After deposition the achieved thickness of each film was measured using a stylus profilometer with a ±5% measurement accuracy (Dektak 150). The radius of curvature of the investigated thin silicon substrate pieces was measured using an optical surface profilometer with sub-nanometer precision (Zygo NewView 6K) and the mean stress of the films was quantified using the Stoney formula given in Equation (4.1). To ensure an accurate measurement, the curvature of bare silicon wafers was measured prior to deposition confirming that the uncoated substrate bending was negligible. The stress measurement results are tabulated in Table 4.4, where it is shown that the fabricated Ge and ZnS films had a tensile stress of 110 ± 8 MPa and a compressive stress of 240 ± 10 MPa, respectively. The small standard deviations obtained from the stress measurements on five different samples indicate high consistency in the film stress.

Residual stress gradients of Ge and ZnS thin films were investigated with the aid of diagnostic microcantilevers. For each material, a series of five films from different deposition runs were prepared under identical deposition conditions as the films used for mean stress measurements. However, in this case the film deposition took place on a sacrificial layer, and freestanding cantilever structures were fabricated and released from the substrate (see Appendix B). During fabrication, a fully cured low-stress polyimide (PI2610 [50], HD Microsystems) was used as the sacrificial layer to ensure that no additional stress was incurred by the introduction of the sacrificial layer. The microcantilevers were fabricated of three different lengths of 50 µm, 100 µm and 200 µm. Figure 4.7 shows the top view obtained using an optical microscope (Figure 4.7a) and a 3D topographical image obtained using an optical surface profilometer (Figure 4.7b) for the fabricated Ge cantilevers. The cantilevers were observed to curl downwards, indicating that our electron-beam deposited Ge films had a negative stress gradient, i.e., the residual stress of the unreleased film was more compressive in the film growth direction (top of film), such that the tips of the as-released 100-µm and 200-µm long cantilevers made contact with the substrate. Using the Young's modulus of $E_{Ge} = 91$ GPa measured by nanoindentation for the electron-beam evaporated Ge thin films and the measured radius of curvature of $R_c = 0.5 \pm 0.03$ mm for the 50-µm long cantilevers, the value of stress gradient of our electron-beam deposited Ge thin films was determined according to Equation (4.11), yielding $\sigma' = -210 \pm 6$ MPa/µm. Unfortunately, we were unable to successfully fabricate cantilever structures for ZnS due to its poor

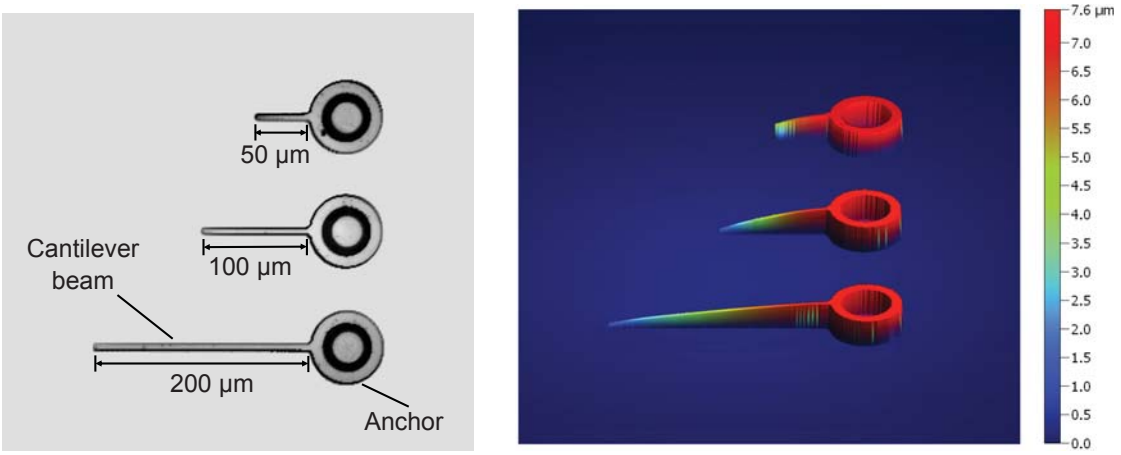

(a) (b)

Figure 4.7: Images of freestanding Ge microcantilevers obtained using (a) an optical microscope and (b) an optical surface profilometer. 3D topography image shows that as-released cantilevers exhibited downward curling, indicating the residual stress in the unreleased Ge thin films was more compressive in the film growth direction. For our cantilever geometry, the stress gradient resulted in the tips of the 100-µm and 200-µm long cantilevers contacting the substrate.

adhesion to the polyimide sacrificial layer, and therefore the stress gradient of ZnS thin films was not determined. Instead, ZnS cantilevers can be fabricated with the aid of an inorganic SiO_2 sacrificial layer and a wet release process. This approach was not attempted in this work, since ZnS will only be deposited as part of the fixed bottom mirror of the designed MEMS-based LWIR Fabry-Perot filter (see Section 3.2.5 in Chapter 3) and its residual stress gradient is not a major concern for filter fabrication.

Table 4.4 summarizes the measured stress properties for electron-beam evaporated Ge and thermally evaporated ZnS thin films. Since Ge forms the movable top mirror of the designed MEMS-based LWIR Fabry-Perot filter, Ge thin film residual stress requires careful consideration in order to realize flat suspended mirrors.

Table 4.4: Mean residual stress of Ge and ZnS thin films. Positive and negative stress values correspond to tensile and compressive stress, respectively. A negative stress gradient value corresponds to stress becoming more compressive in the film growth direction (i.e., top of film).

	Ge	ZnS
Mean stress	$+(110 \pm 8)$ MPa	$-(240 \pm 10)$ MPa
Stress gradient	$-(210 \pm 6)$ MPa/µm	Not determined

Summary

This chapter has presented the preparation of electron-beam evaporated Ge and thermally evaporated ZnS thin films for LWIR mirror formation. It has been shown that while durable Ge films could be deposited at room temperature, high quality ZnS films need to be deposited at substrate temperature high than 150 °C. Subsequently, an iterative least-squares approach has been applied to extract the LWIR optical constants of Ge films deposited at room temperature and ZnS films deposited at 150 °C, with the refractive indices of Ge and ZnS determined to be 4.0 and 2.0 and the extinction coefficients determined to be 2×10^{-5} and 2×10^{-3}, respectively. After a brief review of thin film stress measurement techniques, the substrate bending method and the stress-induced deformation of diagnostic microcantilevers method have been investigated to characterize both the mean stress and the stress gradients of Ge and ZnS thin films, respectively. The mean stress of Ge films was determined to be 110 MPa tensile with a negative stress gradient of 210 MPa/µm. The mean stress of ZnS films was determined to be 240 MPa compressive, while the residual stress gradient of ZnS films has not been measured due to delamination of the ZnS films from the polyimide sacrificial layer.

Chapter 5

MEMS-based LWIR Fabry-Perot filters with tether supported top mirrors

This chapter presents a first iteration towards a MEMS-based LWIR Fabry-Perot filter, which is based on a mature SWIR Fabry-Perot filter technology. Firstly, a discussion of the material and MEMS structural changes required for extending this SWIR technology into LWIR implementation is presented. Then, the key process development steps as well as the complete fabrication process flow for MEMS-based LWIR Fabry-Perot filters are described, including a method of controlling the curvature of the suspended top mirrors. Subsequently, static mechanical and optical characterization of the fabricated filters is presented as an empirical investigation into the effectiveness of the mirror curvature correction approach. In addition, this chapter presents the actuation measurement of doubly clamped beam actuators, which is used to predict the ideal wavelength tuning range of the fabricated filters.

5.1 Previous research on MEMS-based shortwave infrared Fabry-Perot filters

At the initial stage of device development, the fabrication path for MEMS-based LWIR Fabry-Perot filters was adapted from a mature MEMS filter technology previously demonstrated for the short-wavelength infrared (SWIR: 1.6-2.5 µm) range. The details of the MEMS-based SWIR Fabry-Perot filters have been presented by Milne et al. in several publications [34, 51, 52, 53]. Here, we only give a brief description of the most critical aspects of the SWIR filter, including its MEMS structure and the approaches employed to control the curvature in the suspended top mirror of the filter.

The SWIR filter, as shown in Figure 5.1, is composed of two quarter-wave mirrors realized using alternating layers of high-index 111 nm thick Ge and low-index 253 nm thick SiO. A 200 nm thick low-stress SiN_x layer supports the top movable mirror, and extends outwards to form four Au-coated doubly clamped beams, which together with the lower Au electrode are used for electrostatic actuation. The angled tethers that connect the mirror and the beams are used to relieve any transverse force on the beams arising from net tensile stress in the mirror, and hence ensure low-voltage actuation. This filter is fabricated using the surface-micromachining technique and the selective wet etching of a polyimide sacrificial layer.

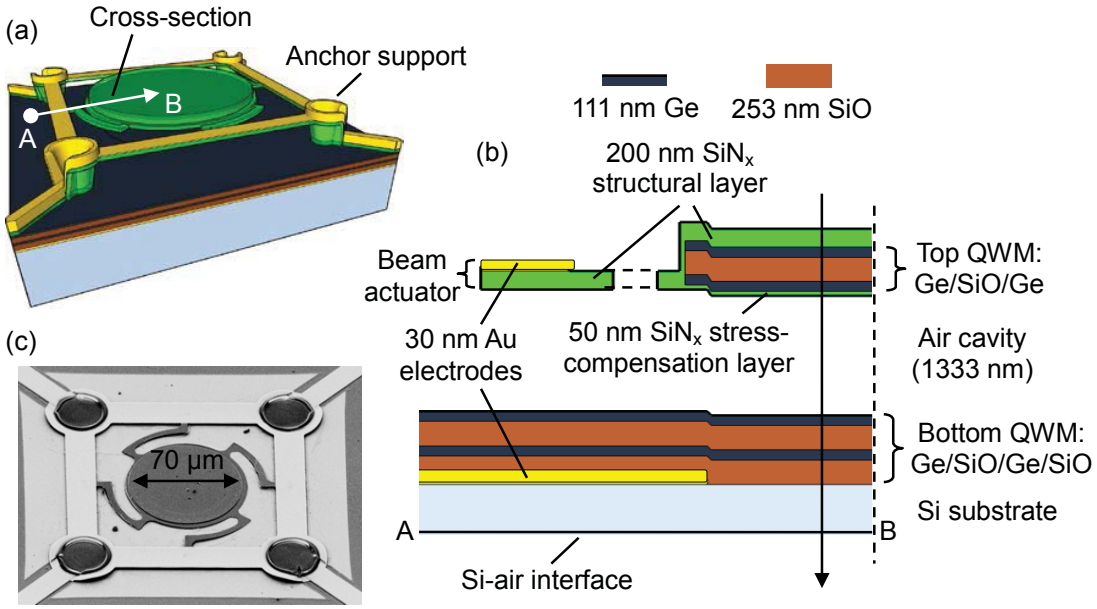

Figure 5.1: (a) 3D graphical depiction of the MEMS-based SWIR Fabry-Perot filter [34, 52], (b) schematic cross-section of the filter along the line AB as indicated in (a), and (c) SEM image of a fabricated filter with a 70-µm diameter mirror. The images are taken from Reference [34].

The suspended top mirror of the SWIR filter, which had initially been deposited with a negative stress gradient (i.e., the residual stress is more compressive with increasing mirror thickness), exhibited a significant convex curvature (bowing up in the center) after release. To eliminate mirror curvature, the mirror stress gradient was compensated in the first place by the use of a 50 nm thick compressively stressed SiN_x layer on the underside of the mirror, and further balanced by developing a tensile stress gradient in the top SiN_x structural layer using post-fabrication O_2 plasma treatment. After curvature correction, the suspended top mirror exhibited a negligible bowing of 15 nm across a diameter of 70 µm. This filter demonstrated

a continuous wavelength tuning range of 1.6-2.5 µm using a control voltage of 22.4 V, with a peak transmittance of 40-60% and a FWHM of 52 nm.

This MEMS filter technology has demonstrated itself as a versatile technology in moving from short-wavelength infrared to mid-wavelength infrared (MWIR: 3-5 µm) by simply increasing the sacrificial layer thickness (cavity length) to 2100 nm and the thicknesses of Ge and SiO mirror layers to 187 nm and 431 nm, respectively, without introducing any changes in patterning geometry or materials [34]. The remainder of this chapter will explore extending this MEMS filter technology into a LWIR implementation.

5.2 Fabrication process development for MEMS-based LWIR Fabry-Perot filters

The MEMS-based SWIR Fabry-Perot filter technology that was described in Section 5.1 can not be simply transitioned into the LWIR range in the same fashion as for the MWIR case, since the fabrication process and thin film materials used for the SWIR filters are not suitable for LWIR implementation. For the fabrication of MEMS-based LWIR Fabry-Perot filters, a number of critical material and structural changes were made:

- Based on the LWIR optical filter design established in Section 3.2.5 of Chapter 3, ZnS was used as the low-index mirror material to replace LWIR absorbing SiO in the bottom mirror. The suspended top mirror was fabricated of a single Ge layer, rather than of a Ge/ZnS/Ge multilayer stack, in order to avoid mirror bowing caused by stress mismatch;

- A ZnS single-layer anti-reflection coating was deposited on the backside of the substrate to suppress the multiple reflections within the substrate, and hence improve the optical transmission of the filter;

- The LWIR filters were fabricated on a LWIR-transparent float-zone (FZ) silicon substrate instead of a conventional Czochralski (CZ) substrate, since Czochralski silicon wafers have strong LWIR absorption due to excessive oxygen content [41];

- No LWIR absorbing SiN_x structural layer was deposited in the optical path. Instead, the same Ge layer that forms the top mirror extends from the perimeter of the mirror to form the tethers and actuator beams, and then down onto the substrate to serve as the structural support;

- The SiN_x stress-compensation layer underneath the Ge top mirror was deposited with a relatively large compressive stress, allowing the negative stress gradient inherent in the Ge mirror (refer to Section 4.3.2 in Chapter 4) to be compensated using a very thin SiN_x layer without introducing considerable optical absorption;

- Flexible angled tethers were replaced by short straight tethers, which renders the freestanding top mirror more resistance to any stress-induced curvature;

- A polyimide spin-coating process was developed to produce the thick, large-area uniform sacrificial layer required for LWIR operation.

The remainder of this section will discuss the two most critical steps in developing the fabrication process for MEMS-based LWIR Fabry-Perot filters , i.e., spin-coating of the thick, large-area uniform polyimide sacrificial layer required for creation of the LWIR optical filter cavity, and the deposition and characterization of ultra-thin SiN_x films used for compensating the stress gradient in the suspended Ge top mirror.

5.2.1 Thick polyimide sacrificial layer with large-area thickness uniformity

According to the LWIR optical design presented in Section 3.2.5 of Chapter 3, the MEMS-based LWIR Fabry-Perot filters in this thesis feature a large optical air cavity of 6.4 µm in length, and therefore require coating of an equally thick sacrificial layer. Moreover, the surface flatness specification for the suspended top mirror (see Section 3.4 in Chapter 3) imposes challenging thickness uniformity requirement for such a thick sacrificial layer.

At the early stage of fabrication process development, polyimide PI2611 (HD microsystems [50], thickness range of 3-9 µm with spin speed of 2000-5000 rpm and 350 °C bake for 30 mins) and ProLIFT 100-24 (Brewer Science [54], thickness range of 4-12 µm with spin speed of 1000-3000 rpm and 245 °C bake for 1 min) were investigated as potential sacrificial materials for the LWIR filters in this thesis. It was found that the films produced from these two materials exhibited extremely dense optical interference fringes under white light illumination, indicating a high degree of thickness non-uniformity. Stylus profilometry showed that the maximum relative thickness variation between distinct color fringes was up to 400 nm, which is significantly larger than the maximum mirror bowing requirement of 300 nm (see Section 3.4 in Chapter 3). Such a significant non-uniformity in coating thickness is

primarily caused by a large difference in surface tension between the high-viscosity PI2611/ProLIFT solutions and the wafer. In other words, the high viscosity of PI2611/ProLIFT makes it difficult to dispense the materials uniformly. For this reason, these two materials were found not to be suitable for fabricating LWIR filters.

PI2610 is a spin-on sacrificial material developed by HD microsystems which has the same chemical compositions and properties to PI2611, but is significantly less viscous in comparison to PI2611. Our practical experience with PI2610 is that it is capable of producing very uniform coatings. Therefore, this material was identified as a possible replacement for PI2611 and ProLIFT. However, PI2610 is a relatively thin sacrificial material that has been designed for < 3 µm thick applications (thickness range of 1-2.5 µm with spin speed of 2000-5000 rpm and 350 °C bake for 30 mins [50]). In order to achieve a coating thickness of 6.4 µm, a multiple coating technique was used according to the following sequence:

- Spin polyimide on the substrate at 2000 rpm for 40 seconds;
- Soft-bake polyimide at 130 °C for 5 minutes on a hotplate in laboratory ambient;
- Slowly ramp up the hotplate temperature to 300 °C at a rate of 4 °C/minute and then hard-bake the polyimide at 300 °C for 30 minutes;
- After the hard bake, cool down the polyimide layer gradually to room temperature by slowly decreasing the hotplate temperature;
- Repeat the above procedure one more time.

The produced film exhibited a uniform color under white light illumination over a 2 inch wafer area, representing a large-area coating with high thickness uniformity. The degree of uniformity was confirmed quantitatively by film thickness measurements at different positions across the wafer, revealing that the average coating thickness was 6.4 µm with a thickness variation of less than 50 nm.

In addition to the establishment of the multiple coating process for the PI2610 sacrificial layer, a dry etch procedure was developed to ensure that positive-angle, gently sloping sidewalls were attained, which are of importance for creating strong and continuous anchor supports. The mechanism is illustrated in Figure 5.2a. PI2610 is masked by a thick positive-tone photoresist (AZ4562, MicroChemicals) that is patterned with an overcut profile, and an O_2/CF_4 plasma dry etch is used

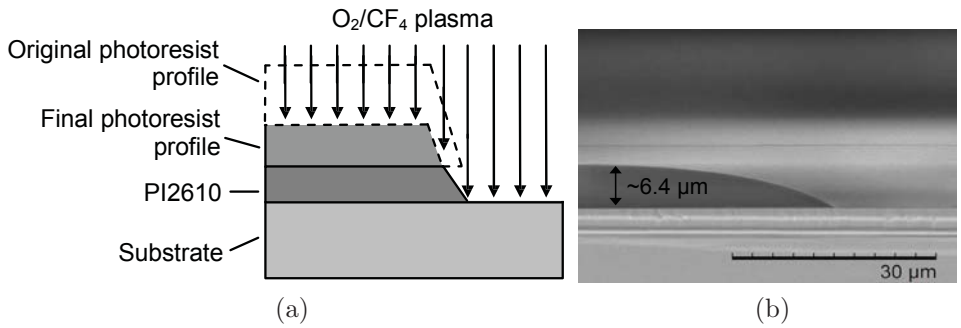

Figure 5.2: Positive-angle, gently sloping sidewalls in the PI2610 sacrificial layer required for building strong and continuous anchor supports can be realized by masking the polyimide layer by a thick photoresist with an overcut profile and subsequent O_2/CF_4 plasma dry etching. The mechanism is illustrated in (a) and the side-view SEM image of a sample profile is shown in (b).

to produce a patterned PI2610 layer with a positive sidewall slope. This positive slope arises from the simultaneous etching of the photoresist and the polyimide. As the photoresist is etched, the overcut recedes, exposing more of the polyimide and over time producing a positive slope. Figure 5.2b shows the side-view SEM image of a sample profile prepared using this technique.

5.2.2 Compressively stressed SiN_x stress-compensation layer

Because the Ge thin film material that forms the top mirror of the LWIR filters had a negative stress gradient (i.e., residual stress is more compressive with increasing film thickness, see Section 4.3.2), the suspended Ge top mirror exhibited a convex curvature after release. In principle, this mirror curvature can be controlled by modifying the Ge layer stress during deposition. However, this approach is not feasible due to the tightly constrained deposition conditions in our electron-beam system. Post-fabrication oxygen plasma treatment approach initially used for the SWIR filters [34, 52] was also attempted. The same process is not suitable for controlling the stress of Ge material, as the plasma resulted in severe damage to the Ge layer. In the fabrication process for MEMS-based LWIR Fabry-Perot filters, the curvature of the suspended top mirror was controlled by depositing a compressively stressed SiN_x layer on the underside of the Ge top mirror to balance the stress gradient in the mirror, as illustrated in Figure 5.3.

Because SiN_x is highly absorbing in the LWIR band, the presence of the SiN_x layer can degrade filter transmission performance. It is therefore essential that the SiN_x layer be thin, and hence the compressive stress in the layer needs to be large.

The SiN_x stress-compensation layers used for the devices in this thesis were deposited using an inductively coupled plasma chemical vapour deposition (ICPCVD)

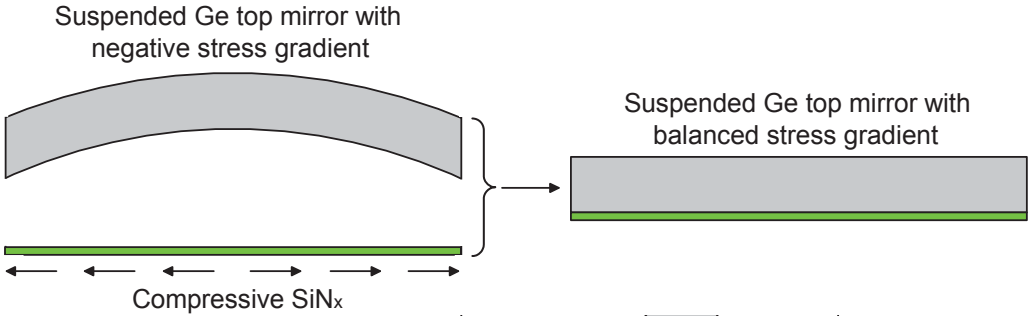

Figure 5.3: Illustration of mirror curvature correction procedure for MEMS-based LWIR Fabry-Perot filters.

system (Sentech SI500D) utilizing SiH_4/He/Ar/NH_3 chemistry. The SiN_x was deposited at an ICP power of 350 W, a pressure of 7×10^{-2} Torr, a substrate temperature of 80 °C, and SiH_4:He:Ar flow rates of 6.9:131.1:120 sccm, with NH_3 flow rate altered from 9.5 sccm to 10.7 sccm to target a compressively stressed film.

The SiN_x stress was initially measured using the substrate curvature method on 500 nm thick films deposited onto 100 µm thick silicon substrates. Since stress can continuously develop during film deposition [55], the overall film stress is dependent on film thickness. As such, the SiN_x stress determined using 500 nm thick films may not accurately represent the stress of SiN_x films for very thin layers (in the neighbourhood of 15 nm thick) as used in the actual LWIR filters. For characterization of the residual stress in very thin SiN_x films, the substrate bending method can be troublesome because the curvature may be too small to be measured experimentally or reliably attributed to the thin film stress. As an alternative approach, doubly clamped beams and ring-and-crossbeam microstructures were used. Fundamental mechanisms of these stress diagnostic microstructures have been previously described in Section 4.3.1. The fabrication process used for the SiN_x diagnostic microstructures was adapted from the process used for fabricating Ge microcantilevers, which were previously described in Section 4.3.2 for characterization of the stress gradient in electron-beam evaporated Ge mirror layers, with the detailed process flow given in Appendix B. The fabricated doubly clamped beam structures had a length of 220 µm and a width of 50 µm; and the ring-and-crossbeam structures had an outer (inner) ring diameter of 220 (180) µm and a beam width of 20 µm. The SiN_x films used for the construction of the diagnostic microstructures were deposited at a nominal thickness of 50 nm.

The vertical deformation of the doubly clamped beams and the crossbeams in the ring-and-crossbeam structures was measured for the quantitative determination of SiN_x thin film stress. For transparent SiN_x films, this quantity could not

be simply measured using white light optical profilometry as was performed for the Ge microcantilevers. Instead, an interferometric technique was used, and its mechanism is illustrated in Figure 5.4. Monochromatic light (wavelength λ) that is incident on a transparent freestanding beam will reflect off the suspended thin film as well as off the underlying substrate surface. As a result, an interference pattern will be produced on the suspended thin film with constructive interference fringes periodically formed wherever the separation between the suspended thin film and the substrate surface is an integer multiple of $\lambda/2$; in other words, two consecutive bright fringes on the suspended thin film represent a relative height of $\lambda/2$. Therefore, the vertical deformation of the beam can be determined by counting the number of bright interference fringes on the suspended thin film and multiplying half of this number by $\lambda/2$.

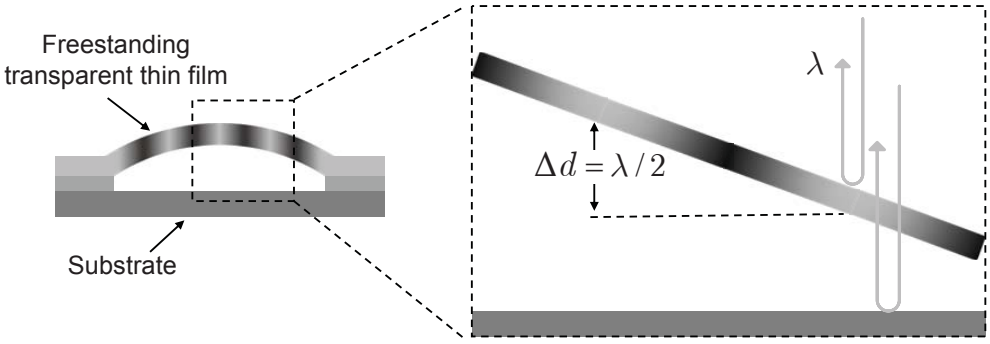

Figure 5.4: Illustration of the interferometric technique used to determine the vertical deformation of transparent, freestanding diagnostic microstructures. Constructive interference fringes form every time the separation between the film and the substrate changes by $\lambda/2$, and therefore the number of interference fringes provides a measure of beam deformation amplitude.

Interferometric images of the fabricated SiN_x diagnostic microstructures were acquired using an optical microscope (Olympus BX60) fitted with a green filter (λ = 532 nm), and are presented in Figure 5.5. As shown in Figure 5.5 (a)-(c), when NH_3 flow rate is below 10.7 sccm, the interference fringes on the doubly clamped beams are clearly visible, indicating a compressive stress in the unreleased SiN_x films. Moreover, the number of interference fringes decreases for the same beam length as the NH_3 gas flow increases, indicating a decrease in the magnitude of the beam vertical deformation and a corresponding decrease in the film compressive stress. As the NH_3 flow rate further increases to 10.7 sccm, the doubly clamped beam becomes flat and the fringes disappear in the field of view, as shown in Figure 5.5 (d), indicating a tensile stress in the deposited SiN_x film, which results in buckling of the crossbeam in the ring-and-crossbeam structure. In addition, it

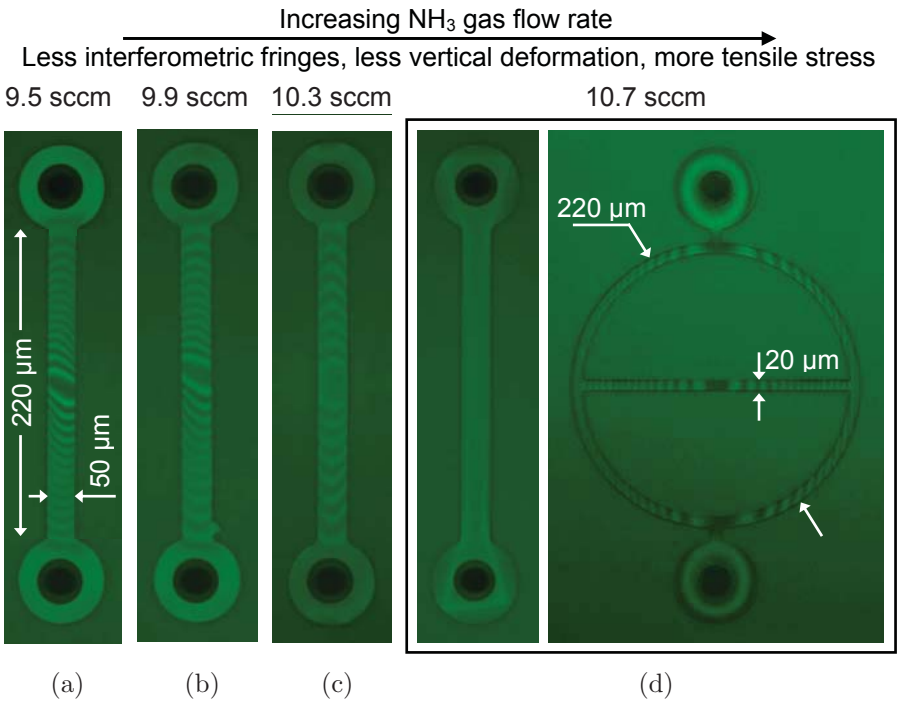

Figure 5.5: Optical microscope images of the released SiN_x diagnostic microstructures obtained under green light illumination ($\lambda = 532$ nm).

was observed under the optical microscope that for all cases, as the objective lens was moved closer to the sample, the beam centre was first brought into focus and then the beam anchors. This observation indicates that the suspended microbeams exhibited upward bending and thereby eliminates any concern that the structures were bending downwards in contact with the substrates.

Figure 5.6 depicts the SiN_x thin film stress as a function of NH_3 gas flow rate, comparing the results obtained for 50 nm thick films via the diagnostic microstructures, and the results obtained for 500 nm thick films via the stress-induced substrate curvature method. It can be clearly seen in Figure 5.6 that the stress values reported by the diagnostic microstructure method are on-average 100 MPa less tensile than the values reported by the substrate curvature method. By considering the results obtained from the 50 nm thick diagnostic microstructures, the SiN_x thin film stress changes from 150 MPa compressive to 100 MPa tensile as the NH_3 flow rate is increased from 9.5 to 11.7 sccm. In this work, a low NH_3 flow rate of 9.5 sccm was used for the ICPCVD SiN_x deposition to ensure a relatively large compressive stress of 150 MPa in the SiN_x stress-compensation layer. Table 5.1 summarizes the ICPCVD deposition conditions of the SiN_x stress-compensation layers. The required thickness of the SiN_x stress-compensation layer was determined experimentally, as will be described in Section 5.3.

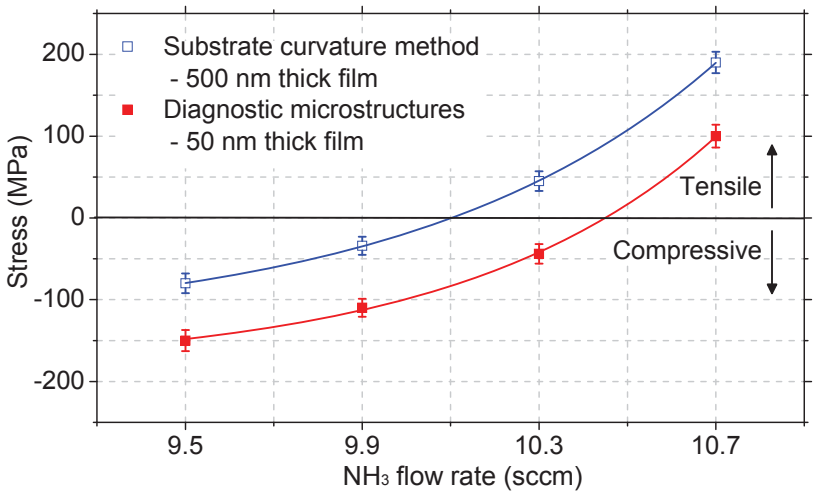

Figure 5.6: SiN_x thin film stress as a function of NH_3 flow rate. The open and solid squares represent the results obtained for 500 nm thick films using the substrate curvature method, and for 50 nm thick films using the diagnostic microstructure method, respectively. The error bars show the standard deviation of the stress measurements on five samples from different deposition runs. The lines joining the data points are simply a guide for the eye.

Table 5.1: Deposition conditions for the SiN_x stress-compensation layer.

ICP power	Chamber pressure	Substrate temperature	Gas flow rate (sccm)			
			SiH_4	He	Ar	NH_3
350 W	7×10^{-2} Torr	80 °C	6.9	131.1	120	9.5

5.3 Filter fabrication and characterization

Following the discussion of process development steps in the previous section, this section presents the fabrication as well as the mechanical and optical characterization of MEMS-based LWIR Fabry-Perot filters. The main focus of this section is to investigate the reduction in top mirror curvature and the improvement in optical performance of the fabricated filters arising from the use of SiN_x stress-compensation layers.

5.3.1 Filter fabrication

A comprehensive fabrication process flow for the MEMS-based LWIR Fabry-Perot filters incorporating the major changes described in Section 5.2 is illustrated in Figure 5.7 (a)-(k). Figure 5.8 depicts the cross section of the filters. Figure 5.9 shows the structural layout and dimensions of the filters and a scanning electron microscope (SEM) image of the fabricated filter with a 150-µm diameter mirror.

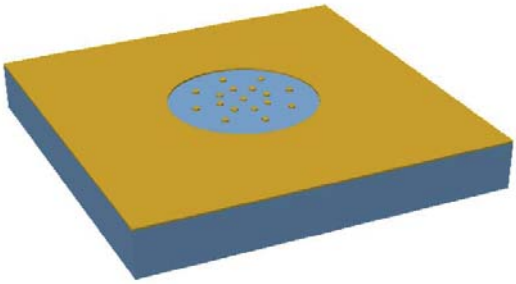

(a) A 200 nm thick Au layer is deposited on a float-zone silicon wafer using thermal evaporation and lift-off. This Au layer acts as the bottom electrode and as an optical shield to block stray light from leaking around the filter onto the detector. This layer also includes an array of circular micropatterns that are aligned with the etch hole array perforated in the top mirror (see subfigure (j)), to block stray light transmitted through the etch holes.

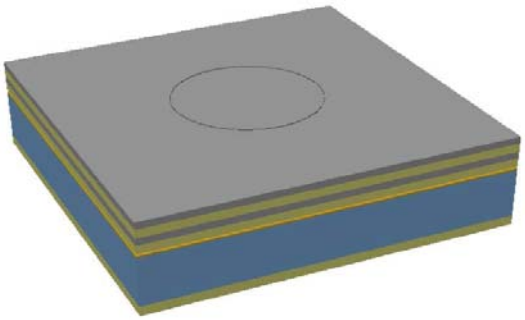

(b) Under the previously established deposition conditions for Ge and ZnS thin films (see Section 4.1), a Ge/ZnS/Ge/ZnS quarter-wave bottom mirror is deposited, followed by deposition of another quarter-wave ZnS anti-reflection coating layer on the backside of the substrate. Bottom electrode bond pad access (not shown) is achieved by dry etching the bottom mirror in a CF_4/H_2 plasma. Ge and ZnS layers have a target thickness of 606 nm and 1102 nm, respectively.

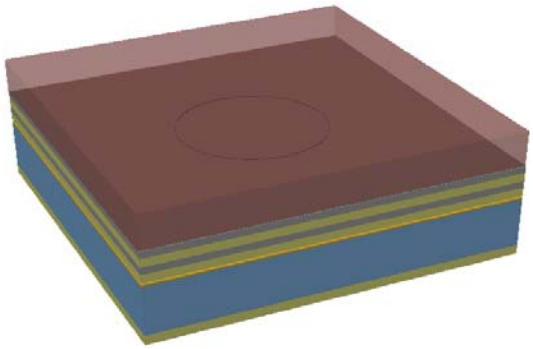

(c) A PI2610 polyimide sacrificial layer is spin-coated onto the sample using the multiple coating technique previously described in Section 5.2.1, with a target thickness of 6.4 µm required for the operating wavelength range of the MEMS-based LWIR Fabry-Perot filters.

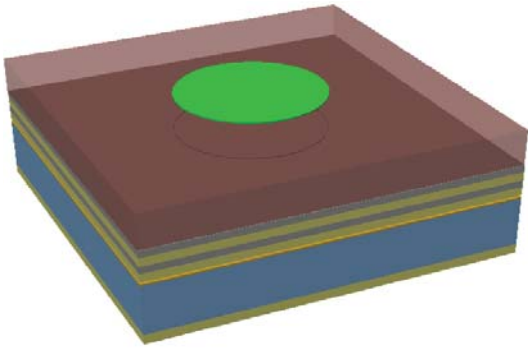

(d) A compressively stressed SiN_x layer is deposited using ICPCVD, under the deposition conditions previously described in Section 5.2.2. This SiN_x layer is selectively removed using CF_4/O_2 plasma from everywhere except below the mirror, to balance the stress gradient in the top mirror.

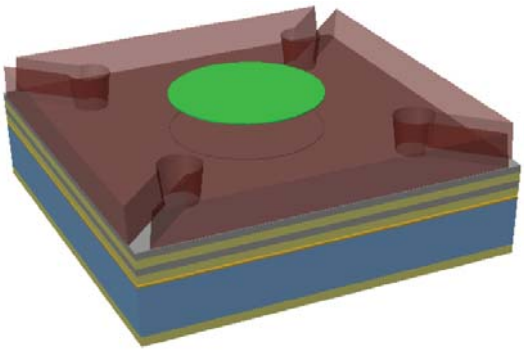

(e) The polyimide sacrificial layer is patterned using the technique previously described in Section 5.2.1, to create step-down, gently sloping sidewalls required for strong and continuous anchor supports.

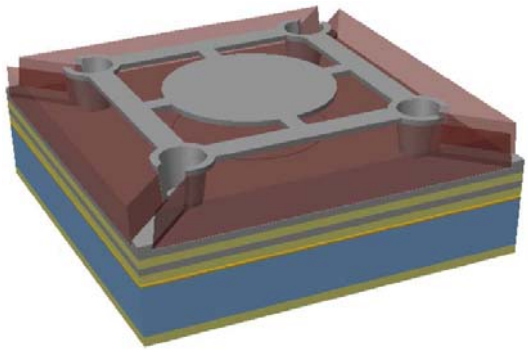

(f) A 250 nm thick Ge layer is deposited using electron-beam evaporation and lift-off. This layer forms part of the top mirror, the tethers and actuator beams, and the structural supports for the suspended top mirror.

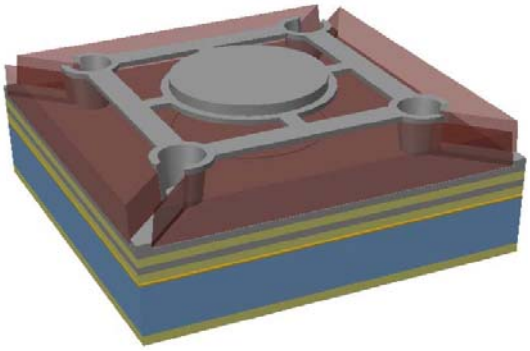

(g) Another 356 nm Ge layer is deposited in the mirror area via electron-beam evaporation and lift-off, which, in combination with the previous 250 nm Ge layer, forms a complete quarter-wave top mirror. This two-step mirror deposition approach results in thin actuator beams for low actuation voltage applications.

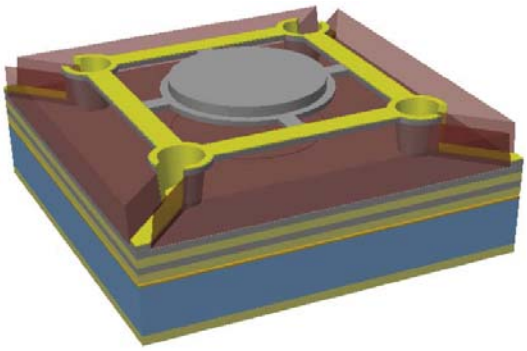

(h) A 50 nm thick Au layer is deposited onto the Ge beams using thermal evaporation and lift-off. This Au layer serves as the top electrode for the MEMS actuators.

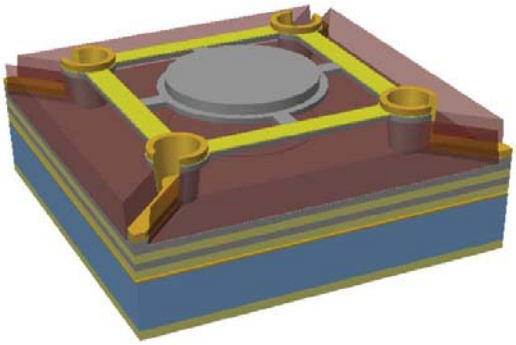

(i) A 300 nm thick Au layer is deposited over the support anchors using thermal evaporation and lift-off. This layer strengthens the supports, provides reliable electrical contact to the top electrodes, and is also used for bonding pads (not shown).

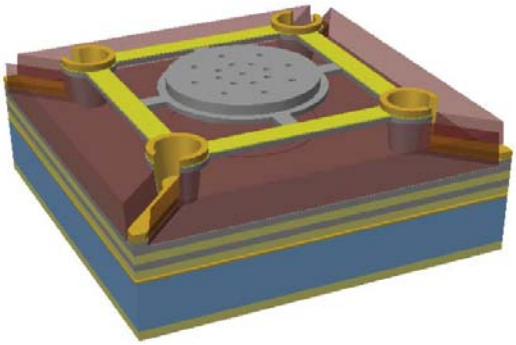

(j) 4-µm diameter holes are etched through the top mirror using a CF_4/O_2 plasma. These holes facilitate the subsequent polyimide removal in an O_2 plasma, allowing the suspended top mirror to be released within a short time, and therefore preventing cracks forming in the Ge top mirror due to overheating from long-time exposure to the O_2 plasma.

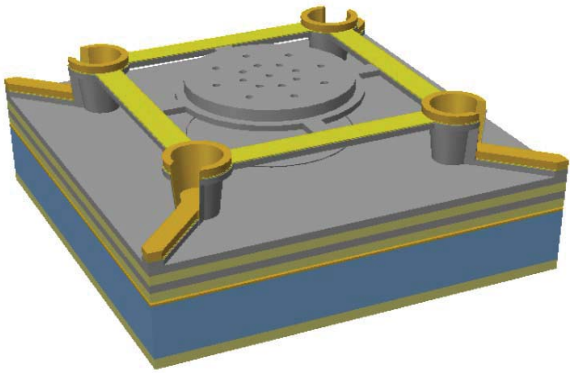

(k) The polyimide sacrificial layer is removed in an O_2 plasma, and freestanding top mirror is released.

Figure 5.7: Fabrication process flow for MEMS-based LWIR Fabry-Perot filters. Note that the layer thicknesses described in the text are the design values.

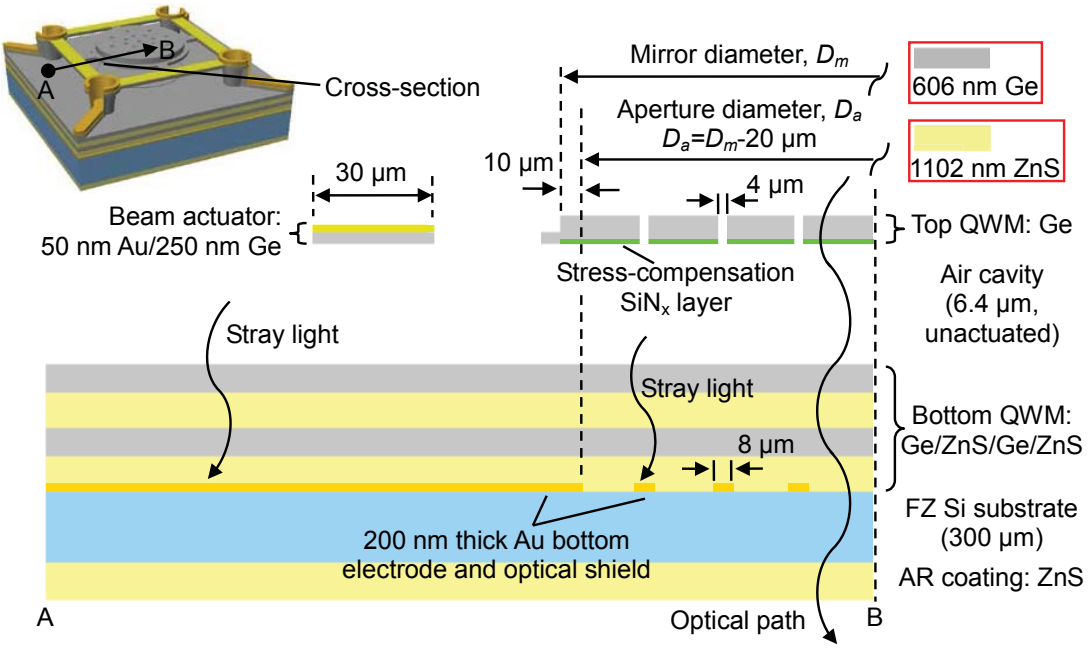

Figure 5.8: Schematic cross-section (A-B) of the MEMS-based LWIR Fabry-Perot filters, showing the MEMS actuator structure, the mirror profile, the mirror stress gradient compensation layer, the optical shield and the optical path of the filters. The figure also defines the mirror and optical aperture diameter. The optical aperture size is 20 μm laterally smaller in diameter than the mirror size and the diameter of Au optical shielding micropatterns is 4 μm larger than the etching hole diameter to prevent any stray light due to pattern misalignment. Note that the layer thicknesses shown in the figure are the design values.

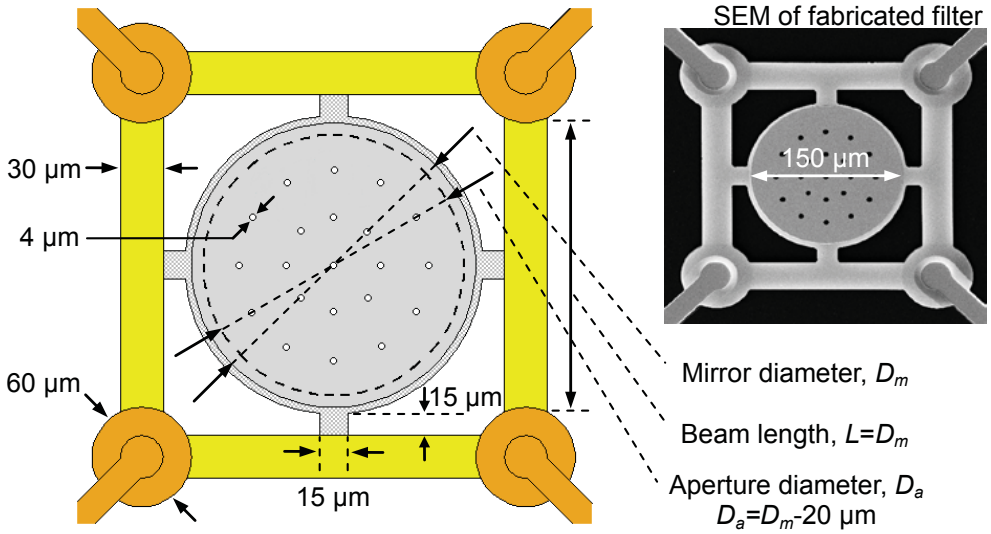

Figure 5.9: Structural layout and dimensions of the MEMS-based LWIR Fabry-Perot filters, and a scanning electron microscope (SEM) image of the fabricated filter with a 150-μm diameter mirror.

The photolithography mask used to fabricate the MEMS-based LWIR Fabry-Perot filters is shown in Figure 5.10a. The mask is divided into 4 identical quadrants, and each quadrant consists of 2 sets of 8 identical filters with mirror diameters of either $D_m = 150$ µm or 200 µm. The mask patterns of the left and right quadrants are flipped vertically with respect to each other. Due to the relatively large optical beam width (approximately 3 mm) of our transmission measurement system, the distance between adjacent filters in the mask is designed to be 4 mm so that only one filter is illuminated at a time and no unwanted transmission signal from adjacent filters is coupled into the detector. Figure 5.10b shows an image of the fabricated sample before release. In this sample, filters in the upper-left quadrant were fabricated without SiN_x stress-compensation layers, while filters in the other three quadrants were fabricated with different SiN_x layer thicknesses of 12 nm, 18 nm and 24 nm, by simply using a shadow mask during subsequent SiN_x depositions. This sample was used to experimentally determine the optimal thickness of the SiN_x stress-compensation layer, and is designated as S1 in this chapter.

Once the optimal thickness of the SiN_x stress-compensation layer was estimated using sample S1, MEMS-based LWIR Fabry-Perot filters with the optimum SiN_x stress-compensation layer were fabricated using the mask shown in Figure 5.10a. In order to examine the batch-to-batch reproducibility of the stress compensation, four samples were prepared from different fabrication runs, which are designated

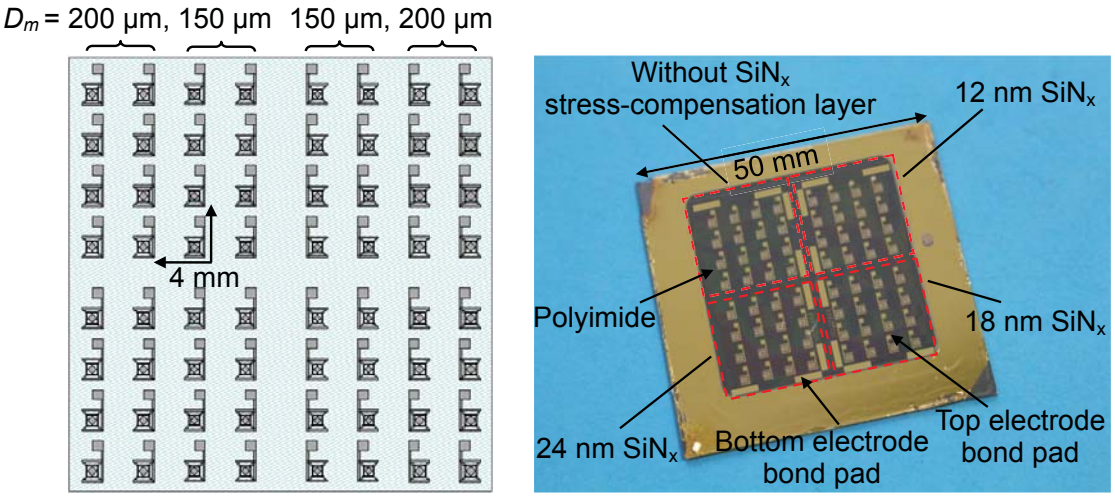

(a) (b)

Figure 5.10: (a) Layout of the photolithography mask for MEMS-based LWIR Fabry-Perot filters. (b) An image of the fabricated sample (50 mm × 50 mm) before release, where filters in the 4 quadrants were fabricated with various SiN_x thicknesses in order to experimentally determine the optimal thickness of the SiN_x stress-compensation layer. The Au top and bottom electrode bond pads, which were not previously shown in Figure 5.7, can also be seen in this image.

Table 5.2: Comparison between the target layer thickness and the actual thickness of the optical layers in the fabricated samples S1-S5, measured using a stylus profilometer.

	Material	Target thickness (nm)	Actual thickness (nm)				
			S1	S2	S3	S4	S5
Top mirror	Ge	606	613	707	530	655	684
Optical cavity	Air	6.4*	5.8*	6.3*	7.0*	5.6*	6.7*
Bottom mirror	Ge	606	565	652	620	695	570
	ZnS	1102	1030	1165	1075	1200	1045
	Ge	606	675	550	720	510	640
	ZnS	1102	1180	1010	1157	1210	1136
Substrate	FZ-Si	300*	300*	300*	300*	300*	300*
AR coating	ZnS	1102	1128	1190	1060	1145	1055

Note: thickness values with * are measured in micrometers, µm .

respectively as S2-S5 in this chapter. Table 5.2 shows the actual layer thicknesses in the fabricated samples S1-S5 measured using a stylus profilometer with a ±5% measurement accuracy (Dektak 150), in comparison to the target layer thicknesses.

5.3.2 Top mirror bowing characterization

Figure 5.11a shows the centre-to-edge mirror bowing of the fabricated 150-µm and 200-µm diameter filters as a function of SiN_x stress-compensation layer thickness, measured using sample S1 with an optical profilometer with sub-nanometer precision (Zygo NewView 6K). As can be seen in Figure 5.11a, mirrors without the SiN_x stress-compensation layers exhibited convex bending, with centre-to-edge bowing amplitudes being 1.5 µm and 2.4 µm for the 150-µm diameter mirrors and 200-µm diameter mirrors, respectively. The results are consistent with the previous argument that a single-layer Ge top mirror would deform in a convex shape under the inherent negative stress gradient (i.e., film stress is more compressive with increasing mirror thickness). For a SiN_x stress-compensation layer thickness of 12 nm, mirror bowing amplitudes can be seen to be significantly reduced, and an abrupt change in mirror bowing direction from convex to concave takes place as the SiN_x thickness changes from 12 nm to 18 nm. According to Figure 5.11a, a compensation layer thickness of approximately 15 nm was expected to be optimal to achieve close to zero curvature for both 150-µm and 200-µm diameter mirrors.

Figure 5.11b presents the measurement results of top mirror bowing of the fabricated filters with 15 nm thick SiN_x stress-compensation layers for four different batches of samples S2-S5. Contrary to the anticipated zero mirror curvature, significantly large mirror bowing was still present in the fabricated filters and, moreover,

mirror bowing varied considerably from batch to batch. In this experiment, the variation is likely to be due to run-to-run variations in the deposition thicknesses of the Ge top mirror layer (see Table 5.2) as well as the SiN_x stress-compensation layer. This comment is based on the fact that the data in Figure 5.11b shows a significantly large run-to-run mirror bowing variation between samples, whereas only a small standard deviation (approximately ± 50 nm) was observed in the mirror bowing amplitude for nominally identical filters on the same wafer.

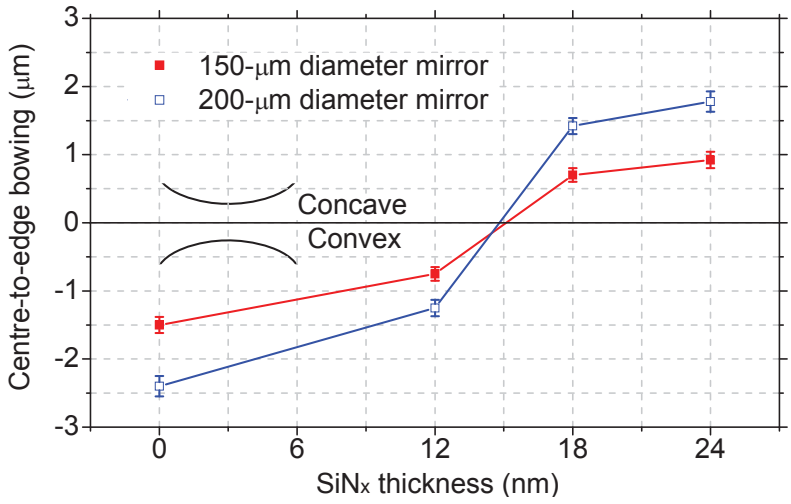

(a)

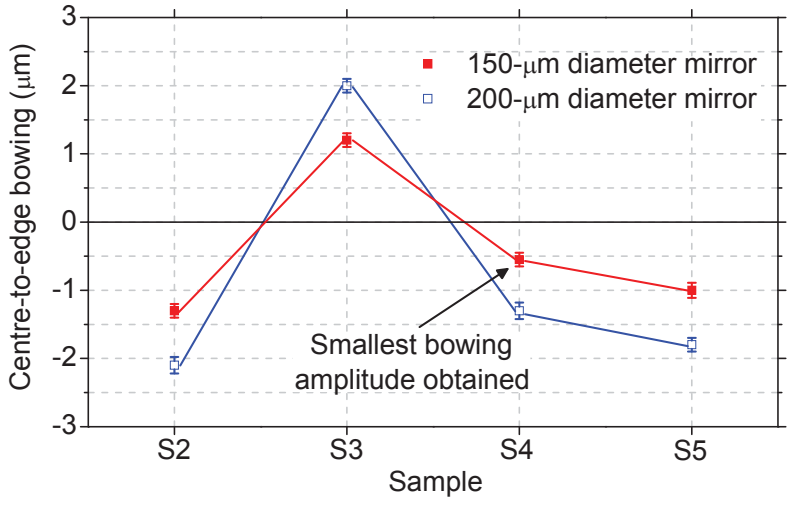

(b)

Figure 5.11: (a) Top mirror bowing as a function of SiN_x stress-compensation layer thickness for the fabricated 150-µm and 200-µm diameter filters, measured using sample S1. (b) Top mirror bowing of the fabricated filters with optimum 15 nm thick SiN_x stress-compensation layers for different batches of samples S2-S5. The lines joining the data points are simply a guide for the eye. The error bars indicate the standard deviations of the mirror bowing measurements for all the nominally identical filters on each sample.

In this work, the smallest mirror bowing amplitude was obtained for the 150-µm diameter filters on sample S4 with a 15 nm thick SiN_x stress-compensation layer, as can be seen in Figure 5.11b. The top mirror surface profile through one of these filters (S4-MD150-SN15) was measured using an optical profilometer with sub-nanometer precision, and is presented in Figure 5.12 in comparison with the mirror surface profile of one of the 150-µm diameter filters on sample S1 that had not been subjected to mirror stress compensation (S1-MD150-SN0). The mirror bowing can be seen to become significantly less convex by the use of a 15 nm thick SiN_x stress-compensation layer, with the centre-to-edge bowing amplitude reduced from 1.5 µm to 550 nm. In addition, it can be seen in Figure 5.12 that both fabricated filters exhibited no mirror tilt.

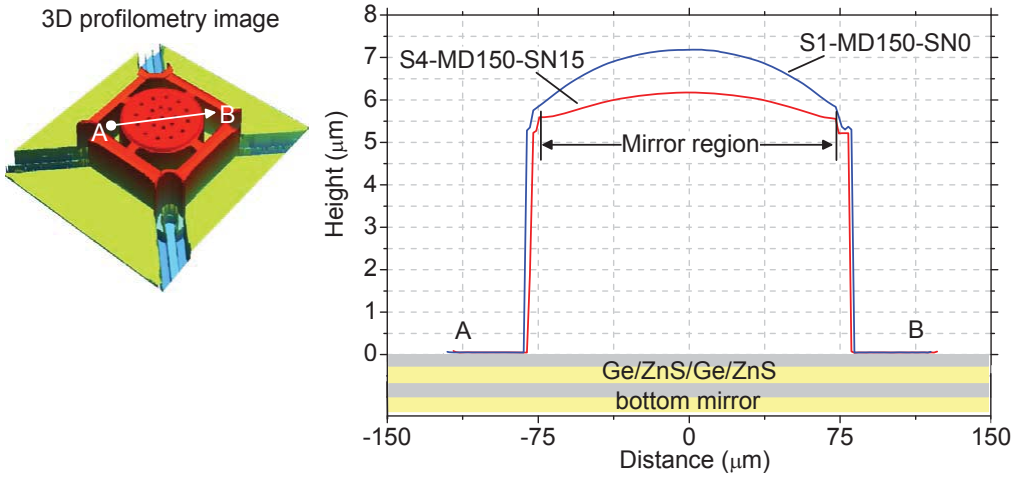

Figure 5.12: Comparison of the top mirror surface profiles (A-B) between a 150-µm diameter filter on sample S4 with a 15 nm thick SiN_x stress-compensation layer (S4-MD150-SN15) and a 150-µm diameter filter on sample S1 without a SiN_x stress-compensation layer (S1-MD150-SN0).

5.3.3 Filter optical transmittance characterization

Total transmittance of the S1-MD150-SN0 and S4-MD150-SN15 filters was measured using Fourier transform infrared spectroscopy (PerkinElmer Spectrum One FTIR Spectrometer). For calibration purposes, a reference sample consisting of a through-wafer 130-µm diameter circular hole (identical to the optical apertures of the filters) was fabricated by deep reactive-ion etching a Si substrate using a SF_6 plasma and 200 nm thick Al as the etching mask. This sample, along with the Al optical masking layer, acted as the light shield for optical reference measurement. The intensity of light transmitted through the fabricated hole opening was measured and multiplied by a correction factor to account for the area of the Au optical

shielding micropatterns on the bottom mirror, thereby yielding the optical reference spectrum for the filters. This correction factor was derived by subtracting the total area of the Au micropattern array from the optical aperture area, and then dividing this value by the optical aperture area. The transmitted light intensity through the filters was subsequently measured and normalized by the optical reference spectrum to yield the total transmittance spectra for the filters.

The experimentally measured total transmittance spectra are shown in Figure 5.13a using data points, in comparison with the ideal filter transmittance spectrum calculated using the optical matrix model (the dashed line). The solid lines in Figure 5.13a represent the transmittance spectra calculated using the "*StackSim*" program described in Section 3.4 based on the measured 3D top mirror bowing profiles for the S1-MD150-SN0 and S4-MD150-SN15 filters. In this calculation, the experimentally measured film thicknesses (Table 5.2) and optical constants (Table 4.3) of Ge and ZnS layers were used. As can be seen in Figure 5.13a, a strong agreement is demonstrated between the measured and modelled spectra, validating that "*StackSim*" is an effective tool for modelling the transmittance spectrum of Fabry-Perot filters in the presence of mirror bowing. In this work, "*StackSim*" was also employed to calculate the filter transmittance spectra over a 20 µm × 20 µm pixel area at different mirror positions in order to examine the on-pixel optical performance of the filters, and the results are shown in Figure 5.13b.

It can be clearly seen in Figure 5.13a that the overall transmittance characteristics of the S1-MD150-SN0 filter are severely degraded due to significant mirror bowing, showing a poor peak transmittance of only 20%, a wide FWHM of 1.3 µm, and a small out-of-band rejection of 8:1. In comparison, the transmission curve of the S4-MD150-SN15 filter shifts to shorter wavelengths, exhibiting a higher peak transmittance of 60%, a narrower FWHM of 700 nm and a larger out-of-band rejection of 24:1. Such a dramatic improvement in filter transmittance characteristics and the observed blue shift in peak transmission wavelength can be attributed to the top mirror bowing reduction and the accompanying decrease in mirror separation arising from the use of a 15-nm SiN_x stress-compensation layer (Figure 5.12).

In contrast to the significant degradation of the transmission peak and FWHM observed in the total transmittance spectra of the S1-MD150-SN0 and S4-MD150-SN15 filters, Figure 5.13b shows that these two filters can achieve ideal on-pixel transmittance characteristics regardless of the amplitude of top mirror bowing; namely, a peak transmittance higher than 80%, a FWHM of 0.5-1 µm, and an out-of-band rejection better than 40:1, all of which exceed the target specifications

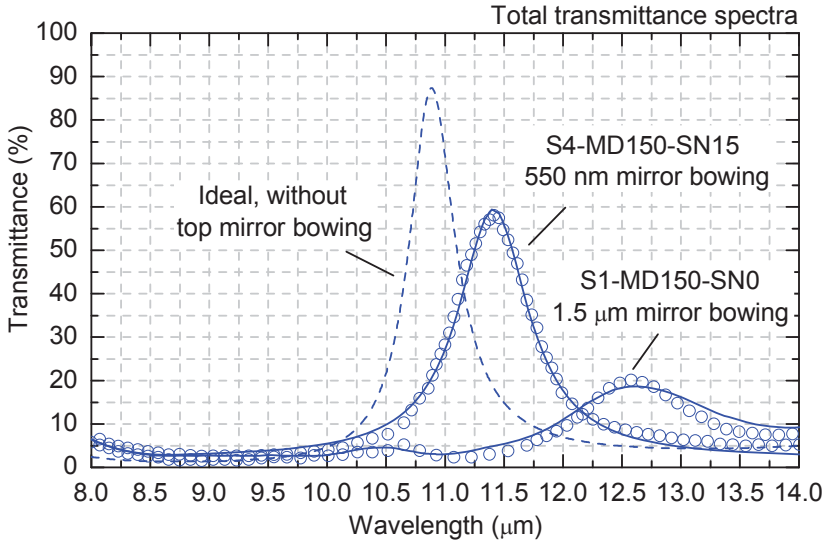

(a)

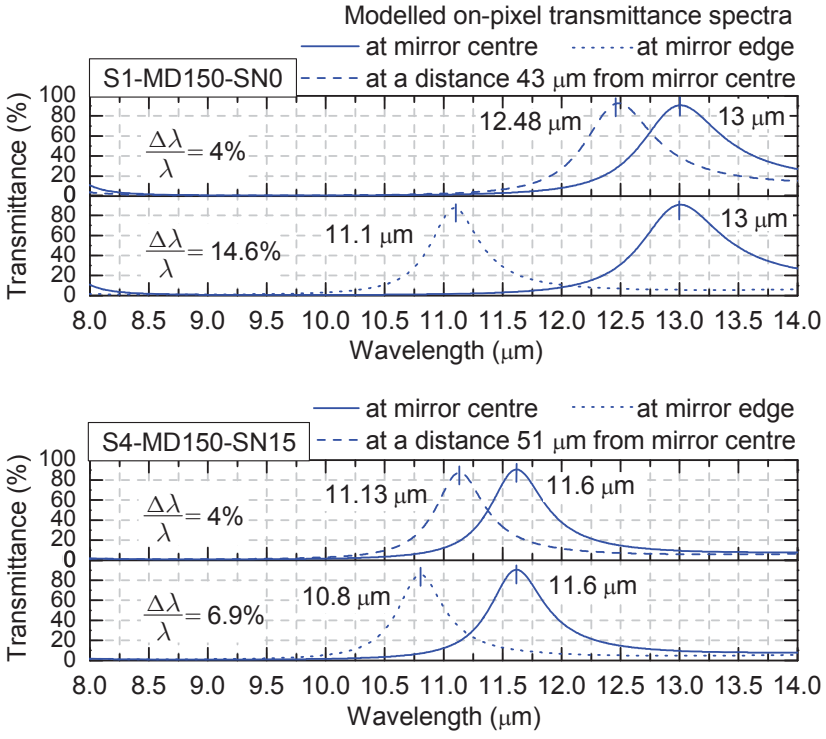

(b)

Figure 5.13: (a) Total transmittance spectra of the S1-MD150-SN0 and S4-MD150-SN15 filters. The dashed line corresponds to the ideal transmittance spectrum calculated using the optical matrix model, while the data points and the solid lines correspond respectively to the spectra measured using FTIR and the spectra calculated using the "*StackSim*" program including the effects of top mirror bowing. (b) Modelled on-pixel filter transmittance spectra over a 20 μm × 20 μm pixel area at different mirror positions. λ is the peak wavelength at the centre of the mirror, and $\Delta\lambda$ is the separation between the peak wavelengths at different mirror positions.

for multispectral thermal imaging applications as listed in Table 1.1. This performance is achieved because individual pixels only 'see' a very small portion of the Fabry-Perot filter (in our case, an area of 20 µm × 20 µm). Thus, any large-area top mirror bowing will not result in a transmission peak decrease or FWHM broadening on the pixel level. However, it will cause a variability of the optical cavity length, which translates into a pixel-to-pixel variation of transmission peak wavelength across the imaging array. As can be seen in Figure 5.13b, for the S1-MD150-SN0 filter, pixel-to-pixel transmission peak wavelength variation across the entire 150-µm diameter optical mirror area is 14.6%, more than triple the maximal specified value of 4% as listed in Table 1.1. In comparison, as a result of the use of a 15 nm thick SiN_x stress-compensation layer and the consequent top mirror bowing reduction, the S4-MD150-SN15 filter shows a significantly lower pixel-to-pixel transmission peak wavelength variation of 6.9% across the entire 150-µm diameter optical mirror area, although this value still can not meet the <4% peak wavelength uniformity specification for multispectral thermal imaging applications. These results are consistent with the optical modelling results presented in Section 3.4 that top mirror bowing needs to be limited to within 300 nm over the entire mirror area in order to achieve the required peak wavelength uniformity specification. Mirror bowing beyond this level will result in >4% pixel-to-pixel transmission peak wavelength non-uniformity, rendering the filters with a smaller usable optical mirror area. As can be seen in Figure 5.13b, for the S1-MD150-SN0 filter, the required <4% pixel-to-pixel peak wavelength variability can only be achieved over the central 86-µm diameter mirror area, which only accounts for 32% of the total mirror area. In comparison, for the S4-MD150-SN15 filter, the required peak wavelength uniformity can be achieved over a larger central mirror area of 102 µm in diameter, which accounts for 46% of the total mirror area. Table 5.3 summarizes the centre-to-edge bowing amplitudes of the suspended top mirrors, the pixel-to-pixel transmission peak wavelength variations across the entire 150-µm diameter mirrors, and the percentage usable mirror areas with <4% peak wavelength variability for the S1-MD150-SN0 and S4-MD150-SN15 filters.

Table 5.3: Top mirror bowing amplitudes, pixel-to-pixel transmission peak wavelength variations across the entire 150-µm diameter mirrors, and percentage usable optical mirror areas with <4% peak wavelength variability for the S1-MD150-SN0 and S4-MD150-SN15 filters.

	S1-MD150-SN0	S4-MD150-SN15
Mirror bowing	1.5 µm	550 nm
Peak wavelength variation	14.6%	6.9%
Percentage usable mirror area (%)	32%	46%

Optical transmission tuning spectra of the filters were not measured since the required top mirror flatness was not achieved throughout the work presented in this chapter. This was not deemed necessary, since the transmission peak wavelength tuning range of the filters can be predicted from the experimentally measured voltage-displacement characteristics of the doubly clamped beam actuators, as will be discussed in the following section.

5.4 Doubly clamped beam actuator fabrication and characterization

5.4.1 Actuator fabrication

The MEMS actuators employed in the LWIR Fabry-Perot filters presented in this chapter were four doubly clamped beam actuators. The actuators were composed of a bilayer of thin Au top electrode and Ge structural layer, with Au bottom electrode deposited below the bottom mirror, as illustrated in Figure 5.14. The beam anchors were fabricated in an inverted top-hat geometry in order to produce strong mechanical support. To further strengthen the supports and to ensure reliable electrical contact to the top electrodes, the anchors were reinforced with a thick Au layer.

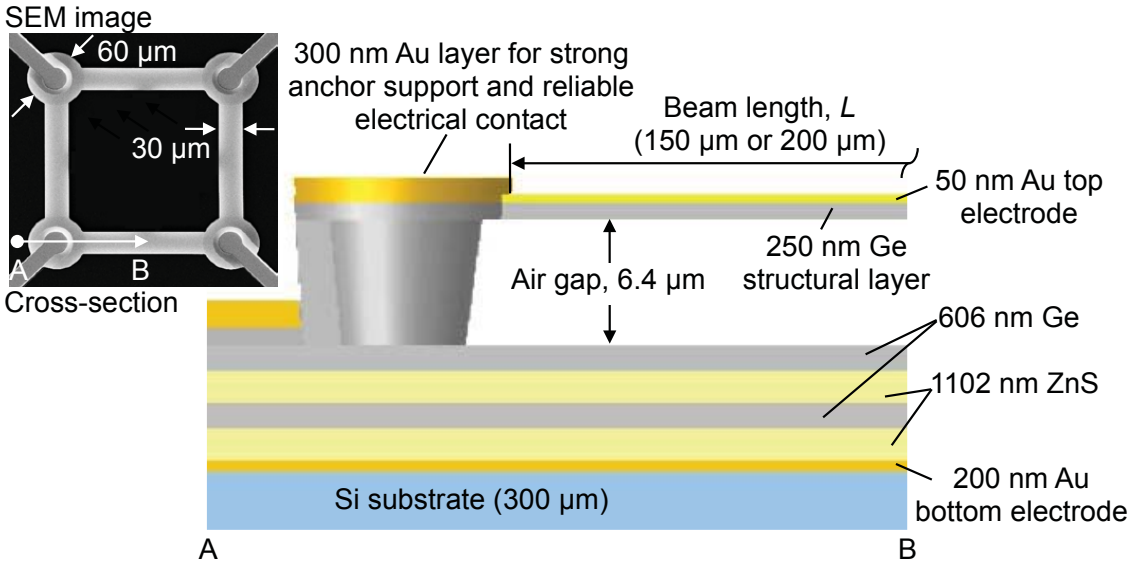

Figure 5.14: Schematic cross-section (A-B) of the doubly clamped beam actuators used in the MEMS-based LWIR Fabry-Perot filters presented in this chapter, and a SEM image of the fabricated actuators without a top mirror. Note that the layer thicknesses shown in the figure are the design values.

Because the fabricated MEMS-based LWIR Fabry-Perot filters exhibited significant top mirror bowing, this can cause out-of-plane structural deformation in the doubly clamped beam actuators, and therefore severely degrade the voltage-displacement characteristics of the actuators. In order to examine the ideal actuation behaviour of the doubly clamped beam actuators, a separate sample was fabricated (denoted as S6 in this chapter) consisting of the doubly clamped beam actuators without a top mirror using the mask depicted in Figure 5.10a. Two actuator structures with beam lengths of $L = 150$ µm and 200 µm were produced, and a SEM image of the fabricated actuators is presented in Figure 5.14. Table 5.4 shows the actual thicknesses of the deposited layers measured using a stylus profilometer with a ±5% measurement accuracy, in comparison with the target layer thicknesses.

Table 5.4: Comparison between the target layer thicknesses and the actual thicknesses of the deposited layers in the fabricated sample S6 measured using a stylus profilometer.

	Material	Target thickness (nm)	Actual thickness (nm)
Top electrode	Au	50	50
Structural layer	Ge	250	230
Actuation gap	Air	6.4*	6.5*
Bottom mirror	Ge	606	550
	ZnS	1102	1153
	Ge	606	675
	ZnS	1102	1200
Bottom electrode	Au	200	190
Substrate	Si	300*	300*

Note: thickness values with * are measured in micrometers, µm .

5.4.2 Actuation of doubly clamped beams

The voltage-displacement characteristics of the fabricated 150 µm and 200 µm long doubly clamped beam actuators were measured by applying a set of DC voltages to the actuators and measuring the beam centre displacements from their initial positions using an optical profilometer with sub-nanometer precision. Figure 5.15 presents the measurement results for two beam lengths using data points, showing a clear decrease in actuation voltage for an increase in beam length. The largest measured displacement for the 150-µm long beam was 2 µm using an actuation voltage of 150 V. In comparison, to achieve the same displacement amplitude, the 200-µm long beam required a lower actuation voltage of 120 V. Upon further increasing the actuation voltage, both beams were observed to undergo mechanical fracture.

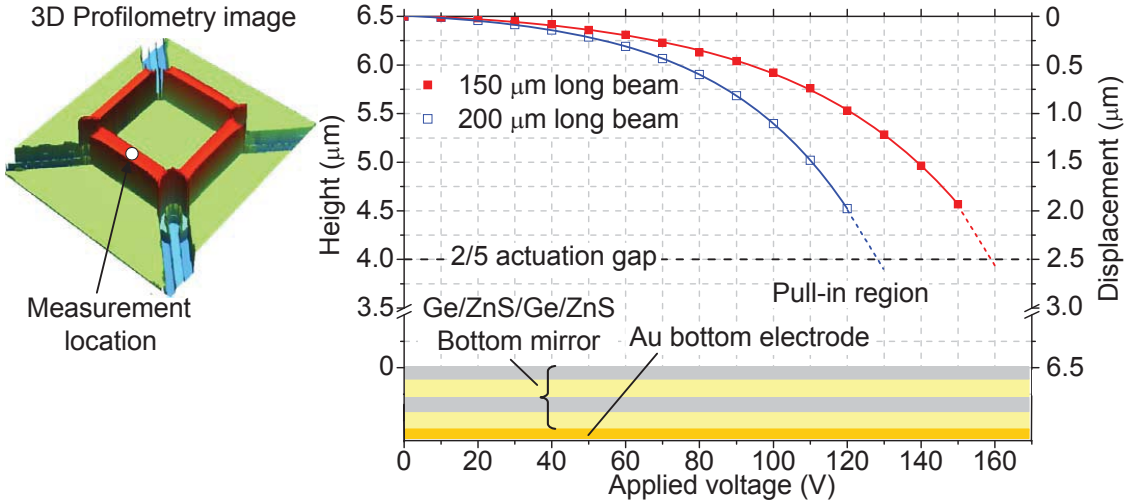

Figure 5.15: Beam displacement as a function of actuation voltage for the fabricated 150 µm and 200 µm long doubly clamped beams.

The mechanical fracture is most likely due to severe deformation of the Ge beams arising from electrostatic pull-in, which is a commonly encountered phenomenon in electrostatic actuators [56, 57]. In general, when parallel-plate actuator travels more than approximately one-third of the initial distance between electrodes, the electrostatic force overcomes the mechanical restoring force, causing the actuator to abruptly snap down onto the substrate. For doubly-clamped beam actuators, electrostatic pull-in occurs at approximately 2/5 of electrode gap [34]. In order to verify that electrostatic pull-in is the cause of the mechanical fracture observed in the doubly clamped beam actuators, the voltage-displacement curves for the 150 µm and 200 µm long beam actuators were extrapolated using the measured displacement data, as shown in Figure 5.15. As indicated in Figure 5.15, when the applied actuation voltage was 160 V for the 150 µm long beam and 130 V for the 200 µm long beam, the beam displacements were expected to exceed 2/5 of the initial actuation gap. This resulted in electrostatic pull-in, forcing the beams to undergo a significant deflection across the entire 6.5 µm gap and subsequently causing the Ge beams to fracture.

Based on the measured voltage-displacement data presented in Figure 5.15 and the modelled filter transmission tuning behaviour presented in Figure 3.8, it can be inferred that the MEMS-based LWIR Fabry-Perot filters based on the doubly clamped beam actuators presented in this chapter can achieve a controllable wavelength tuning range of approximately 9–12 µm. This expected wavelength tuning range is 1 µm less than the target tuning range of 8–12 µm and is limited by electrostatic pull-in and mechanical fracture of the doubly clamped beam actuators.

Summary

This chapter has presented our first attempt to fabricate MEMS-based LWIR Fabry-Perot filters based on a mature MEMS filter structure that had previously been demonstrated in the SWIR region, with a top movable mirror centrally supported by four flexible tethers connected to doubly clamped beam actuators. Material changes as well as MEMS structural modifications required for extending this SWIR filter technology into the LWIR wavelength range were discussed. Subsequently, key steps in the development of the fabrication process and a comprehensive fabrication process flow for the MEMS-based LWIR Fabry-Perot filters were described. The main focus of this chapter was to investigate the use of a SiN_x stress-compensation layer to balance the stress gradient in the suspended top mirror, and thus control mirror bowing. An experimental procedure to determine the optimal thickness of the SiN_x stress-compensation layer was described, and mirror bowing characterization of the filters fabricated from different runs was presented. It was shown that the run-to-run variations in the deposition thicknesses of the Ge top mirror layer as well as the SiN_x stress-compensation layer resulted in uncontrollable stress compensation and thus variable mirror bowing. Throughout this work, the smallest mirror bowing achieved after stress compensation was 550 nm across a 150-µm diameter mirror, which is a significant reduction in comparison to the original mirror bowing of 1.5 µm prior to stress compensation. The on-pixel optical performance of the filters showing the smallest mirror bowing of 550 nm was examined. Optical modelling showed that although these filters can achieve ideal on-pixel transmittance characteristics that exceed the target specifications for multispectral thermal imaging applications, namely a peak transmittance higher than 80%, a FWHM of approximately 500 nm, and an out-of-band rejection better than 40:1, they suffer from a significant pixel-to-pixel transmission peak wavelength variation of 6.9% across the 150-µm diameter mirror area, and the required <4% peak wavelength variability can only be achieved within the central 46% of the total optical mirror area. Lastly, this chapter described actuation measurements of doubly clamped beams, and these measurements predict the maximum wavelength tuning range of the filters is 9–12 µm. Overall, MEMS-based LWIR Fabry-Perot filters presented in this chapter show promise for use in multispectral thermal imaging applications. However, the filters only demonstrated partial correction of mirror bowing, and peak performance was not achieved. It would require significantly more effort for this filter technology to be capable of realizing the large-area tunable filters necessary for hybridizing with FPAs. In particular, processing variations need to be under better control before such a filter technology can be fully realized.

Chapter 6

MEMS-based LWIR Fabry-Perot filters with stretched-membrane based top mirrors

For the MEMS-based LWIR Fabry-Perot filters presented in the previous chapter, top mirror bowing is caused by relief of the in-built stress gradient in the Ge mirror layer, which is difficult to suppress using a stress-compensation approach due to run-to-run processing variations. In order to fabricate flat suspended top mirrors, a mirror structure that is insensitive to stress gradients and independent on process instabilities is required. Considering that our electron-beam evaporated Ge mirror layer has a tensile stress (see Section 4.3.2), if the top mirror was to be fabricated such that it is part of a self-supporting membrane anchored at its periphery (like a drum-skin), then tensile stress inherent in the Ge mirror layer will tend to stretch the whole suspended membrane and reinforce the mechanical stiffness of the membrane to resist any stress-gradient induced bending, thus aiding in flattening the top mirror and eliminating the need for any stress management.

This chapter presents the fabrication of stretched-membrane based LWIR Fabry-Perot filters as well as the mechanical and optical characterization of the actuated filters, demonstrating that this filter design can achieve near-perfect as-released mirror flatness over a square millimeter size mirror area, as well as superior on-pixel optical tuning characteristics that exceed the target spectral specifications for multispectral thermal imaging applications. This chapter also presents the cryogenic cooling tests for the fabricated filters, showing that the filters can maintain excellent mirror flatness after cooling to an operating temperature of 77 K, as required by LWIR thermal imaging FPAs.

6.1 Filter fabrication

A comprehensive fabrication process flow for the MEMS-based LWIR Fabry-Perot filters employing a stretched Ge membrane as the suspended top mirror is illustrated in Figure 6.1 (a)-(f). Figure 6.2 depicts the cross section of the filters. Figure 6.3 shows the structural layout and dimensions of the filters, and a SEM image of the fabricated filter with a 500-µm dimension mirror. In this filter design, the electrodes have a relatively small width of 20 µm and a small suspension length of 120 µm. At this stage, such electrode configuration is just a try-and-see for the initial prototype devices to investigate whether it can result in desirable low actuation voltages for LWIR operation, which otherwise would be improved for the future design.

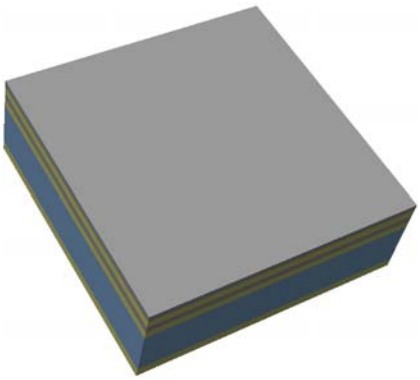

(a) Under the previously established deposition conditions for Ge and ZnS thin films (see Section 4.1), a Ge/ZnS/Ge/ZnS quarter-wave bottom mirror is deposited on a float-zone silicon wafer, followed by deposition of another quarter-wave ZnS anti-reflection coating layer on the backside of the substrate. Ge and ZnS layers have the target thicknesses of 606 nm and 1102 nm, respectively.

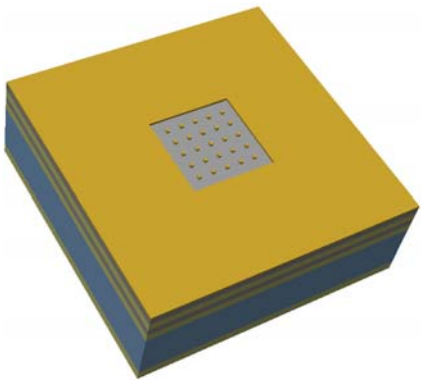

(b) A 200 nm thick Au layer is deposited on the bottom mirror using thermal evaporation, and patterned using lift-off. This Au layer acts as the bottom electrode and as an optical shield to eliminate stray light leakage around the filter. This layer also includes an array of square micropatterns which are aligned with the etch hole array perforated at a later processing step in the top mirror (see subfigure (e)), to shield stray light transmitted through the etch holes.

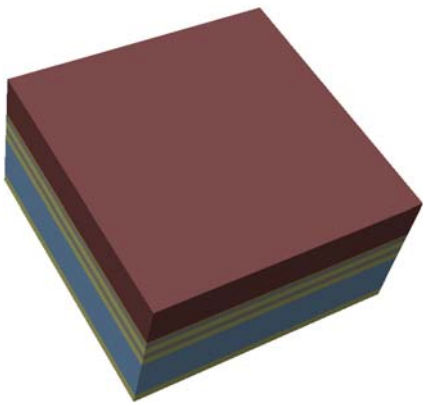

(c) A PI2610 polyimide sacrificial layer is spin-coated onto the sample using the multiple coating technique previously described in Section 5.2.1, with a target thickness of 6.4 µm, as required for the operating wavelength range of the MEMS-based LWIR Fabry-Perot filters.

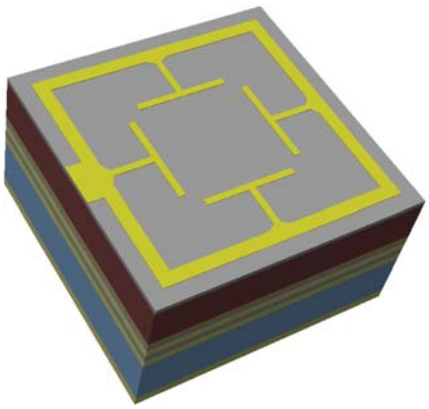

(d) A 606 nm thick Ge layer is deposited onto the sample using electron-beam evaporation, forming the suspended top mirror membrane of the filter. A 50 nm thick Au layer is then deposited using thermal evaporation and lift-off. This Au layer serves as the top electrode for MEMS actuation, and also forms the electrode bond pad (not shown).

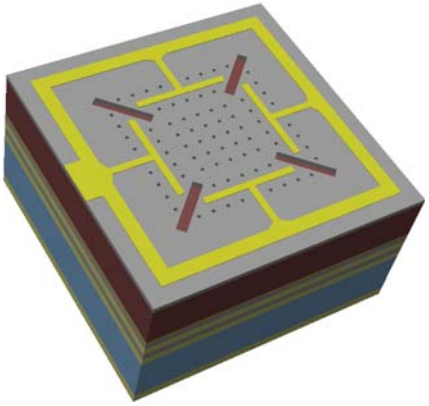

(e) An array of 4-µm sized square holes, four diagonal cut-outs, and a window for the bottom electrode bond pad (not shown) are etched in the top Ge membrane using a CF_4/O_2 plasma. The hole array defines the suspended membrane area, and also facilitates the subsequent sacrificial layer etching process in an O_2 plasma, preventing any deterioration of the Ge membrane due to over-exposure to the O_2 plasma. The diagonal cut-outs serve to release the convergence of film stress from two orthogonal directions and to reduce the spring stiffness of the Ge membrane, allowing low-voltage actuation.

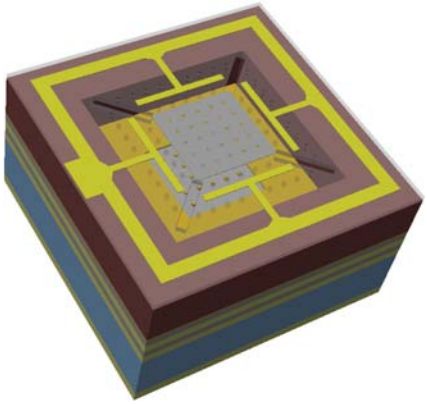

(f) The top mirror membrane is released by selectively etching the central portion of the polyimide sacrificial layer through the etch hole array and cut-outs using an O_2 plasma. The remaining polyimide around the filter perimeter serves as a structural support for the suspended top membrane and also as an electrical insulation for the top and bottom electrodes. Moreover, the polyimide below the etched window in the Ge membrane layer is also removed to expose the bottom electrode bond pad (not shown). In this figure, the top membrane, except for the central mirror, is drawn semi-transparent for illustration purposes.

Figure 6.1: Fabrication process flow for MEMS-based LWIR stretched-membrane Fabry-Perot filters. Note that the layer thicknesses described in the text are the design values.

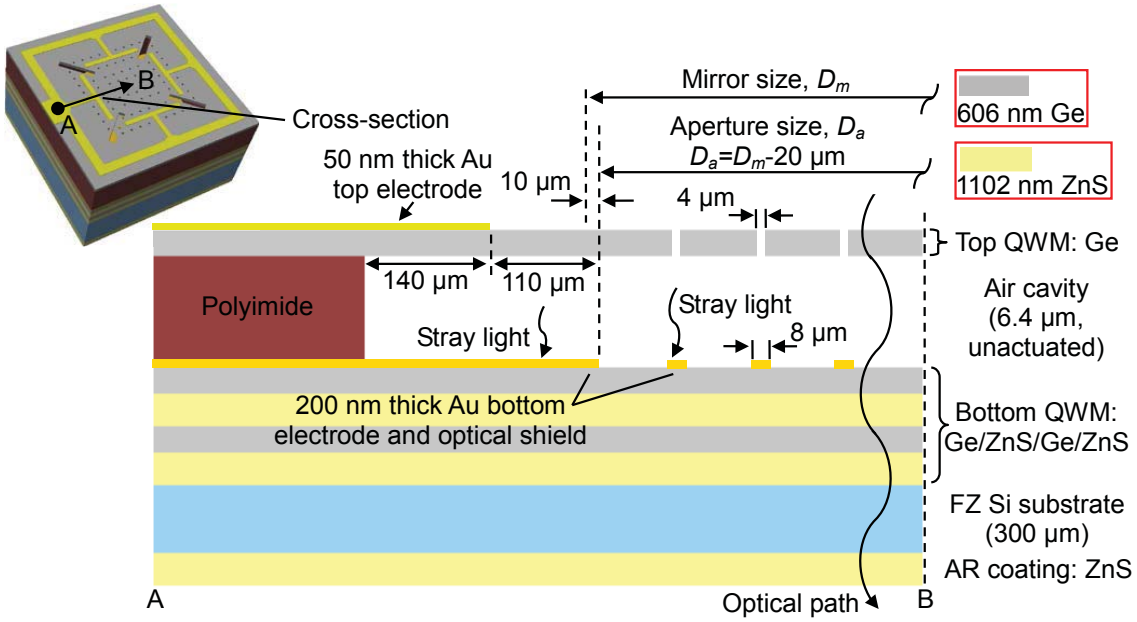

Figure 6.2: Schematic cross-section (A-B) of the MEMS-based LWIR Fabry-Perot filters, showing the mirror profile, the MEMS actuator structure, the optical shield, the optical path of the filters, and the use of polyimide for the MEMS structural support and the electrical insulation between the top and bottom electrodes. The opening in the Au bottom electrode layer defines the optical aperture of the filters. The optical aperture size is 20 μm laterally smaller than the mirror size and the size of the Au optical shielding micropatterns is 4 μm larger than that of the etch holes to prevent unintended stray light due to any misalignment errors.

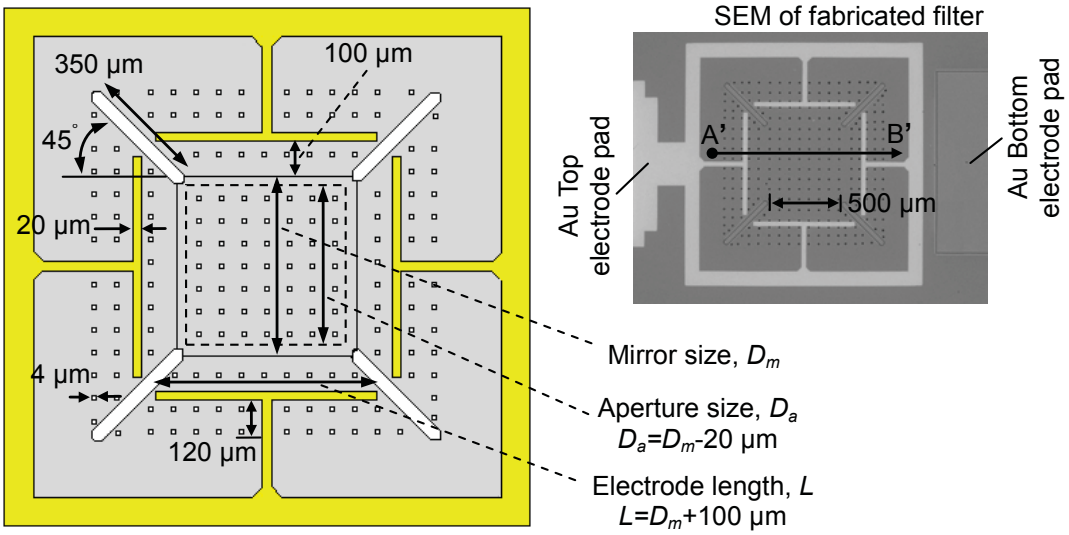

Figure 6.3: Structural layout and dimensions of the MEMS-based LWIR Fabry-Perot filters, and a scanning electron microscope (SEM) image of the fabricated filter with a 500-μm sized mirror. The Au top and bottom electrode bond pads, which were not previously shown in Figure 6.1, can be seen in the SEM image. The line A'B' indicates the location of the mirror surface line profiles presented in Figures 6.5 and 6.7.

The photolithography mask used to fabricate the filters is shown in Figure 6.4a. The mask consists of 37 filters with different mirror sizes of D_m = 200 µm, 500 µm, 1000 µm, 2 mm, 5 mm and 1 cm. Considering the relatively large optical beam width (approximately 3 mm) of our transmission measurement system, the distance between adjacent filters in the mask is larger than 3 mm to ensure that only one filter is illuminated at a time and no unwanted transmission signal from adjacent filters will be detected. Three samples were fabricated from different runs, which are designated respectively as S1-S3 in this chapter. Figure 6.4b shows an image of the fabricated sample. Table 6.1 shows the actual thicknesses of the deposited layers in the fabricated samples S1-S3, in comparison with the target layer thicknesses.

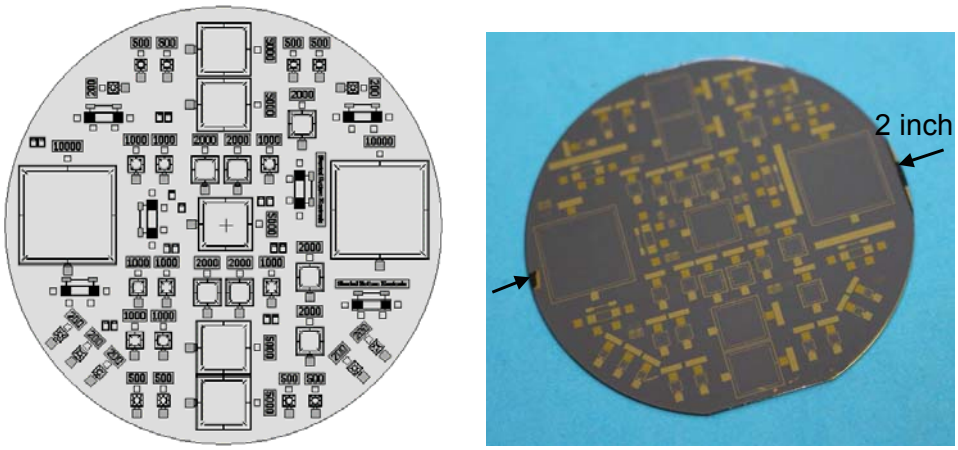

(a) (b)

Figure 6.4: (a) Photolithography mask layout. (b) An image of the fabricated sample.

Table 6.1: Comparison between the target and actual thicknesses of the deposited layers in the fabricated samples S1-S3 as measured using a stylus profilometer with a ±5% measurement accuracy (Dektak 150).

	Material	Target thickness (nm)	Actual thickness (nm)		
			S1	S2	S3
Top electrode	Au	50	46	55	52
Top mirror	Ge	606	565	670	630
Optical cavity	Air	6.4*	5.93*	5.89*	5.82*
Bottom electrode	Au	200	190	205	209
Bottom mirror	Ge	606	690	572	622
	ZnS	1102	1170	1175	1062
	Ge	606	535	640	700
	ZnS	1102	1010	1040	1033
Substrate	FZ-Si	300*	300*	300*	300*
AR coating	ZnS	1102	1035	1140	1200

Note: thickness values with * are measured in micrometers, µm .

6.2 Filter characterization

All the filters with a mirror area larger than 1000 µm underwent mechanical fracture during release. This section presents the characterization of the successfully released 200-µm, 500-µm and 1000-µm dimension filters from different fabrication runs.

6.2.1 Electromechanical characterization

Filter electromechanical behaviour was studied by applying a set of DC actuation voltages to the filters and measuring top membrane deflection using an optical profilometer with sub-nanometer precision. The deflection profiles of the freestanding membranes for the 200-µm, 500-µm and 1000-µm dimension filters were extracted along the line A'B' as indicated in Figure 6.3, and are presented in Figure 6.5.

As evident from the insets of Figure 6.5, the central mirrors of the three unactuated filters exhibited near-perfect flatness, with bowing and roughness on the nanometer scale across the entire optical area. This finding is consistent with the argument presented at the beginning of this chapter that tensile thin film stress can stretch the suspended membrane flat. Indeed, this nanoscale mirror flatness was not only obtained for these three filters, but also observed for all the filters on samples S1-S3 fabricated from different processing runs, indicating that the stretched-membrane based filter design is insensitive to mirror stress gradient and fabrication process variations.

As the actuation voltage increases, top mirror bowing is developed. We observed the largest bowing amplitudes of 100 nm at 160 V for the 200-µm filter; 400 nm at 135 V for the 500-µm filter; and 550 nm at 85 V for the 1000-µm filter. This mirror bowing is due to the electrical conductivity of Ge layers, which applies the actuation voltage over the whole top and bottom Ge mirror layers and thus causes the entire Ge top membrane to be actuated and bend during actuation. This issue can be addressed by depositing electrical insulation layers between the Au electrodes and Ge layers, which is a direction of future work. Any additional increase in the actuation voltage above these values resulted in mechanical failure of the membrane, which occurred before the expected electrical snap-down at one-third of the unactuated electrode separation. We believe that this phenomenon is most likely due to severe overall tensile forces developed in the Ge membrane during actuation. This observation gives a strong implication that mechanical robustness of the Ge membrane material needs to be significantly improved in order to prevent any mechanical failure from occurring during device implementation.

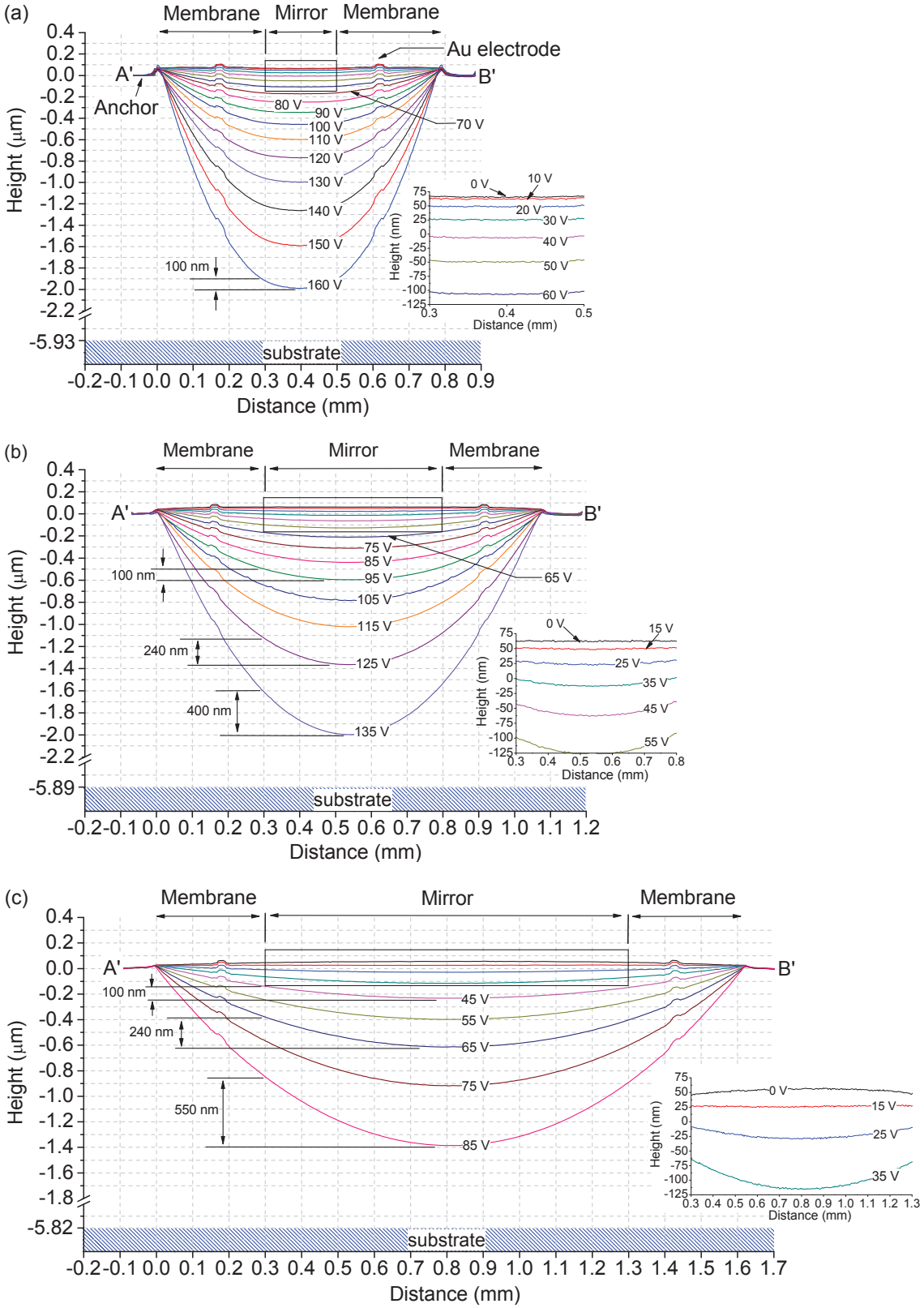

Figure 6.5: Top membrane deflection profiles measured by an optical profilometer along the line A'B' as indicated in Figure 6.3 during actuation of (a) 200-µm, (b) 500-µm and (c) 1000-µm dimension filters. Insets show profiles of the mirror optical area on an expanded scale at low actuation voltages.

6.2.2 Optical characterization

Fourier transform infrared spectroscopy (PerkinElmer Spectrum One FTIR Spectrometer) was used to measure the total transmittance of the 200-µm, 500-µm and 1000-µm dimension filters as a function of actuating voltage. For calibration purposes, a set of reference samples consisting of 180-µm, 480-µm and 980-µm dimension through-wafer square holes (identical in area to the optical apertures of the three filters) were fabricated by deep reactive-ion etching of Si substrates using a SF_6 plasma and 200 nm thick Al as the etching mask. These samples, along with the Al optical masking layers, acted as the light shield for optical reference measurements. The intensity of light transmitted through the fabricated openings was measured and multiplied by a correction factor to account for the area of the Au optical shielding micropatterns on the bottom mirror, thereby yielding the reference spectrum for each filter size. This correction factor was derived by subtracting the total area of the Au micropattern array from the optical aperture area, and then dividing it by the optical aperture area. The transmitted light intensity through the filters was then recorded for the same actuating voltages used for the electromechanical characterization (Figure 6.5) and normalized by the respective reference spectrum to yield the total transmission tuning spectra for each filter.

The experimentally measured tuning spectra for the three different filters are presented in Figure 6.6a using data points. The solid lines in Figure 6.6a represent the transmittance spectra calculated using the "*StackSim*" program described in Section 3.4 based on the measured 3D top mirror bowing profiles of the three filters, showing excellent agreement with the measured spectra. In this work, "*StackSim*" was also employed to calculate the filter transmittance over a 20 µm × 20 µm pixel area at the centre and edge of the mirror area, in order to examine the on-pixel optical performance of the three filters, and the results are shown in Figure 6.6b.

As can be seen in Figure 6.6a for the 200-µm dimension filter, the measured wavelength tuning range was observed to be 8.47–11.46 µm and was obtained using a maximum voltage of 160 V. This wavelength tuning range is comparable with the tuning range of 9–12 µm predicted for the 200-µm dimension filters with doubly-clamped beam actuators (Section 5.4.2), but was achieved with a significantly higher actuation voltage in comparison with the 120 V expected for the filters with beam actuators. This wavelength tuning range accounts for 75% of the complete thermal imaging band of 8–12 µm. The 200-µm filter exhibited consistent near-ideal transmittance characteristics over the entire tuning range, including a high peak transmittance in the range of 80–87%, a FWHM value of approximately

500 nm, and an out-of-band rejection better than 40:1. Moreover, the modelling results in Figure 6.6b show that this 200-µm dimension filter is capable of achieving a pixel-to-pixel transmission peak wavelength uniformity of better than 1.2% across a 200 µm × 200 µm optical imaging area over the entire wavelength tuning range. These transmittance characteristics show a significant improvement in comparison with the results achieved for the filters with doubly-clamped beam actuators (a peak transmittance of 60%, a FWHM of 700 nm, an out-of-band rejection of 24:1, and a pixel-to-pixel wavelength uniformity of 6.9%, see Section 5.3.3). Such high performance is a direct consequence of the achieved level of suspended top mirror flatness (see Figure 6.5a), and exceed the optical specifications listed in Table 1.1, resulting in the 200-µm dimension tunable filters being highly suitable for use in multispectral thermal imaging applications.

The significant degradation of the overall filter transmission peak and FWHM observed in the tuning spectra of the 500-µm and 1000-µm dimension filters correlates well with the mirror bowing trends observed in Figure 6.5 for these two filters. In contrast, it is noted that in a 2-D imaging array the individual pixels only 'see' a very small part of the Fabry-Perot filter (in our case, an area of 20 µm × 20 µm). Thus, any large-area mirror bowing will not result in a transmission peak decrease or FWHM broadening on the pixel level. However, it will cause a variability of the optical cavity length, which will translate into a pixel-to-pixel variation of transmission peak wavelength across the imaging array. As can be seen in Figure 6.6b, the larger 500-µm and 1000-µm dimension filters can achieve ideal on-pixel transmittance characteristics over the entire tuning range regardless of the amplitude of top mirror bowing; namely, a peak transmittance higher than 80%, a FWHM of approximately 500 nm, and an out-of-band rejection better than 40:1, which exceed the target specifications for multispectral thermal imaging applications. However, for both filters, the required pixel-to-pixel peak wavelength variability ($\Delta\lambda/\lambda < 4\%$) can only be achieved over a limited actuation range; namely, 9.3–11.4 µm (wavelength tuning range at mirror centre) for the 500-µm dimension filter with an actuation voltage of less than 125 V, which accounts for 52% of the complete thermal imaging band, and 10.3–11.3 µm for the 1000-µm dimension filter with an actuation voltage of less than 65 V, which accounts for 25% of the thermal imaging band. These wavelength ranges represent the usable spectral tuning ranges for these two filters in order to meet the performance specifications listed in Table 1.1. By correlating these observations with the mirror bowing measurements in Figure 6.5, it can be concluded that in order to achieve the required peak wavelength uniformity specification, top mirror bowing of the filters developed during actuation needs to

be limited to within 240 nm over the entire optical area. Mirror bowing beyond this level will result in considerable pixel-to-pixel peak wavelength non-uniformity, rendering the filters unusable for multispectral thermal imaging applications. For the 500-µm dimension filter, as the actuation voltage is increased to 135 V and the bowing of the mirror over the optical area is correspondingly increased to 400 nm, pixel-to-pixel transmission peak wavelength variation across the filter increases to 6.5%. For the 1000-µm dimension filter, at the maximum actuation voltage of 85 V and the corresponding mirror bowing of 550 nm, this value reaches 8.6%, which is more than double the maximal specified value. Table 6.2 summarizes the centre-

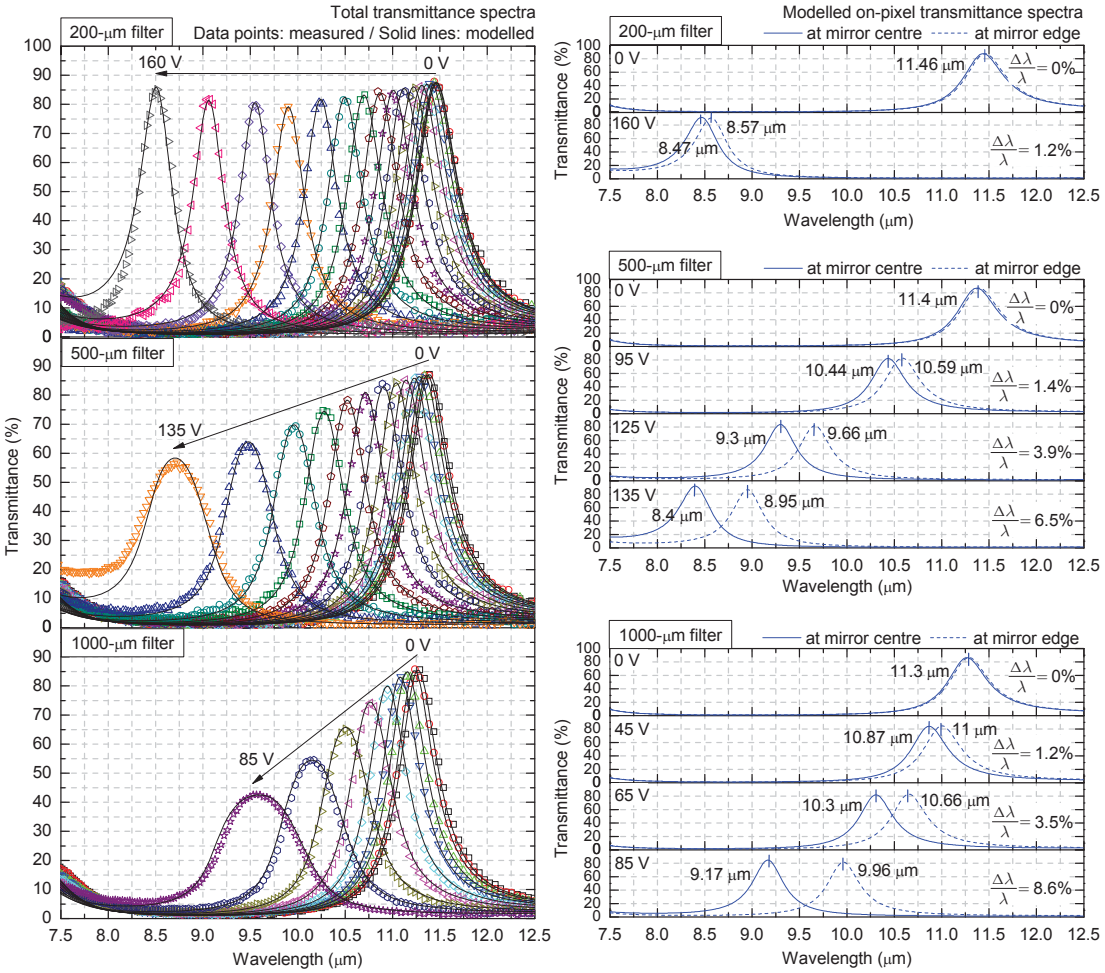

Figure 6.6: (a) Total transmittance spectra measured by FTIR (data points) during actuation of 200-µm, 500-µm and 1000-µm dimension filters, and the transmittance calculated using the "*StackSim*" program including the effects of top mirror bowing (solid lines). (b) Modelled on-pixel filter transmittance over a 20 µm × 20 µm pixel area at the centre and edge of the mirror for various actuation voltages. λ is the peak wavelength at the centre of the mirror, and $\Delta\lambda$ is the separation between the peak wavelengths at the centre and edge of the mirror.

Table 6.2: Top mirror bowing amplitudes, wavelength tuning ranges (at mirror centre) and pixel-to-pixel peak wavelength variations of the 200-µm, 500-µm and 1000-µm dimension filters for different actuation voltage ranges.

	Actuation voltage (V)	Mirror bowing (nm)	Wavelength tuning range (µm)	Peak wavelength variation
200-µm filter	0-160	0–100	11.46–8.47	0–1.2%
500-µm filter	0-95	0–100	11.4–10.44	0–1.4%
	95-125	100–240	10.44–9.3	1.4–3.9%
	125-135	240–400	9.3–8.4	3.9–6.5%
1000-µm filter	0-45	0–100	11.3–10.87	0–1.2%
	45-65	100–240	10.87–10.3	1.2–3.5%
	65-85	240–550	10.3–9.17	3.5–8.6%

to-edge bowing amplitudes of the suspended top mirrors, the wavelength tuning ranges, and the pixel-to-pixel transmission peak wavelength variations of the three filters for different actuation voltage ranges.

In addition, by comparing the performance of these three filters with the results published by other research groups (Table 2.1), it can be seen that while our filter technology shows relatively higher peak transmittance than those previously reported filters, it requires 3 to 5 times higher actuation voltage and exhibits much wider FWHM that is more than double of the FWHM of those filters.

6.2.3 Cryogenic cooling test

The previous sections have shown that the stretched-membrane based LWIR Fabry-Perot filters can achieve nanometer-scale as-released mirror flatness, as well as meet the target spectral specifications for multispectral thermal imaging. However, all these characteristics were achieved at room temperature. Because state-of-the-art HgCdTe-based LWIR photodetector FPAs are generally cooled to 77 K for low dark current operation, the filters must be suitable for use in a cryogenic environment. Upon cooling to cryogenic temperatures, filters may suffer from significant mirror deformation due to thermal expansion mismatch between the Ge mirror layer and underlying structural layers (polyimide support and silicon substrate), which can severely degrade the optical performance of the filters. As an initial investigation into the low-temperature mechanical behaviour of the stretched-membrane based LWIR Fabry-Perot filter design, the fabricated 200-µm, 500-µm and 1000-µm di-

mension filters were cryogenically cooled and the surface flatness of the suspended top mirrors was examined.

Cryogenic cooling tests were performed with the use of a cryostat that was cooled using liquid nitrogen. The sample stage of the cryostat was connected to a liquid nitrogen reservoir via a copper cold-finger, and cooled by thermal conduction. Temperature control of the sample stage was achieved using a silicon-diode temperature sensor and a resistive heater with the aid of a PID temperature controller. The three tested samples were mounted onto the sample stage using thermally conductive vacuum grease, and thermocouples were attached to the samples with silver epoxy for monitoring the temperatures of the samples. The cryostat was mounted onto an optical profilometer (Zygo NewView 6K), which was equipped with a dispersion-compensated objective [58] to measure filter surface profiles through the optical window of the cryostat. In order to calibrate the dispersion-compensated objective, filter surface profiles were first measured at room temperature with and without the optical window of the cryostat in the path. This confirmed that the surface profile measurement error introduced by the cryostat window was negligible when using the dispersion-compensated objective. Before filling liquid nitrogen into the reservoir, the cryostat chamber was evacuated to $\sim 10^{-6}$ Torr in order to prevent any condensation forming on the samples during the cryogenic cooling process. Profilometry measurements were taken when the sample temperatures stabilized at 77 K; and during measurements, the cryostat vacuum chamber was sealed and the vacuum pump was turned off to minimize any vibration effects on the optical profilometer.

Figure 6.7 shows the top membrane surface profiles measured at a liquid nitrogen temperature of 77 K (solid lines) for the 200-µm, 500-µm and 1000-µm dimension filters, in comparison with the profiles measured at room temperature (dashed lines). It can be seen in Figure 6.7 that the freestanding membranes of the three filters consistently exhibited 50-60 nm up-lifting relative to the anchor plane regardless of cryogenic cooling. This is likely to be caused by the stress gradient in the Au/Ge bi-layer structure. In addition, the top electrode step profiles measured at 77 K were observed to be inverted in comparison to the room temperature case. This is likely due to the significant optical reflection phase change arising from a change in the refractive indices of the Au and Ge thin film layers caused by cryogenic cooling, and further investigation is required to clarify the reason. More critically, it can be seen in Figure 6.7 that after cooling to liquid nitrogen temperature, in spite of showing some surface roughness, the central mirrors of all three filters maintained excellent flatness, with overall bowing and roughness on the order of tens of nanometers. The achieved mirror flatness at 77 K can be attributed to the tension forces developed in

the freestanding membrane, which arose as a result of the Si substrate experiencing less contraction than the Ge mirror layer upon exposure to cryogenic cooling [49].

At the time of writing, our cryogenic testing setup was not capable of measuring electrical actuation and optical transmission. Thus, the electromechanical and optical tuning characterization of the cooled filters was not conducted as part of this thesis, but will be undertaken as part of future research. Nevertheless, based on the preliminary cryogenic cooling test results shown in Figure 6.7, it can be foreseen that the stretched-membrane based LWIR Fabry-Perot filters presented in this chapter can achieve the target spectral tuning characteristics for multispectral thermal imaging applications while operating at liquid nitrogen temperature.

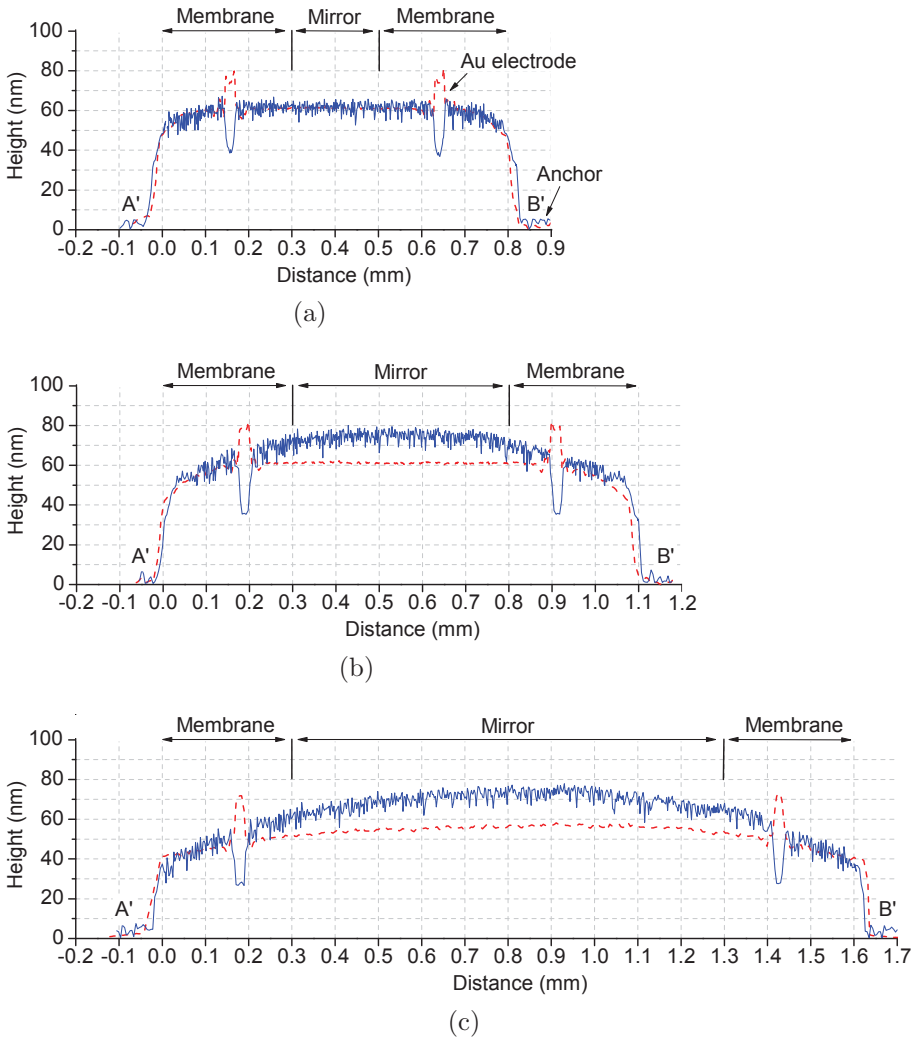

Figure 6.7: Comparison of the top membrane surface profiles measured at a liquid nitrogen temperature of 77 K (solid lines) and at room temperature (dashed lines) for (a) 200-µm, (b) 500-µm and (c) 1000-µm dimension filters. A'B' is the measurement location of the top membrane surface profiles as indicated in Figure 6.3.

Summary

This chapter has reported the fabrication of a MEMS-based tunable LWIR Fabry-Perot filter, employing a single-layer tensile-strained Ge membrane as both the suspended top mirror and the MEMS actuator support. Mechanical and optical characterization of the tunable filters of various sizes were presented and compared. It has been shown that this stretched-membrane based LWIR Fabry-Perot filter design is not affected by mirror layer stress gradients and run-to-run processing variations, and can achieve nanometer-scale as-released top mirror flatness across large mirror dimensions in the millimeter range without any extraneous stress management techniques. The fabricated filter with a 200-µm dimension mirror demonstrated <100 nm top mirror bowing over the entire actuation range and, as a result, exhibited near-theoretical spectral characteristics across the entire wavelength tuning range of 8.47–11.46 µm under a maximum actuation voltage of 160 V; namely, a peak transmittance above 80%, a FWHM of approximately 500 nm, and an out-of-band rejection greater than 40:1. In addition, optical modelling showed that the 200-µm dimension filter is capable of achieving excellent pixel-to-pixel transmission peak wavelength uniformity over the entire actuation range, with a peak wavelength variation of less than 1.2% across a 200 µm × 200 µm optical area. All of these optical parameters exceed the target spectral specifications for multispectral thermal imaging applications. In comparison, the 500-µm and 1000-µm larger dimension filters were shown to exhibit considerable mirror bowing and total transmittance degradation upon actuation. The effects of top mirror bowing on the on-pixel spectral performance of the 500-µm and 1000-µm dimension filters were examined. It was shown that although these two filters can achieve ideal on-pixel transmittance characteristics over the entire actuation ranges, they suffer from significant pixel-to-pixel transmission peak wavelength variations at high actuation voltages and, thus, for the required <4% peak wavelength variability specification, have narrower usable spectral tuning ranges of 9.3–11.4 µm and 10.3–11.3 µm, respectively. Lastly, this chapter also presented the preliminary results of cryogenic cooling tests on the fabricated filters, demonstrating that the static filters can maintain excellent nanometer-scale mirror flatness even after cooling to 77 K. Overall, the MEMS-based tunable LWIR Fabry-Perot filters with a stretched-membrane based top mirror design presented in this chapter are suitable for hybridizing with a cryogenically cooled 2-D LWIR imaging focal plane array for the realization of miniature multispectral thermal imaging systems.

Chapter 7

Conclusions and future work

7.1 Conclusions

State-of-the-art spectral thermal imaging systems have the capability of capturing completely passive thermal images over multiple discrete wavelength bands in the long-wavelength infrared (LWIR) spectral range of 8–12 µm. The spectral data can be used to extract compositional information of objects, thus allowing discrimination and identification of targets in applications such as night vision for defence applications, mineral mapping, and volatile organic compounds detection. In conventional multispectral thermal imagers, wavelength band selection is realized using a series of band-pass interference filters mounted on a mechanically-switched wheel, whose significant size and cost prevent wide adoption of the technology in many desirable applications. On the other hand, micro-electromechanical systems (MEMS) based Fabry-Perot filters can be small and lightweight, and far less costly in comparison to filter wheels. MEMS-based Fabry-Perot filters consist of two mirrors separated by an optical cavity, and optical resonance within the cavity enables the transmission of a narrow wavelength band from a broadband incident spectrum. Electrostatic actuators are employed in such devices to alter the length of the optical cavity and hence tune the transmitted wavelength band. A large-area MEMS-based LWIR Fabry-Perot filter can be hybridized with an HgCdTe-based 2-D LWIR imaging focal plane array to realize next-generation miniature, low-cost multispectral thermal imaging sensors.

This thesis has conducted a comprehensive review of the literature on MEMS-based LWIR Fabry-Perot filters. It has found that the reported filters feature high spectral resolution by incorporating highly reflective multilayer Bragg mirrors. Any suspended mirror deformation arising from stress mismatch between different mirror layers and thermal expansion mismatch during cryogenic cooling of LWIR

photodetectors will degrade filter transmission performance and, in particular, cause pixel-to-pixel transmission peak wavelength non-uniformity across the imaging focal plane arrays. Complicated stress-control mechanisms were employed to overcome this challenge. For example, mirror stress gradients can be balanced by tailoring the layer stress conditions, but this requires extensive material characterization and stringent process control to minimize run-to-run material stress variations. To control stress induced mirror deformation, very thick, mechanically stiff carrier wafers have also been used. However, this increases the chip size considerably and renders the filters susceptible to gravity effects and external vibrations. The aim of this thesis was to demonstrate MEMS-based LWIR Fabry-Perot filters based on a single-layer top mirror approach that could meet the target spectral specifications for multispectral thermal imaging applications, namely a peak transmittance higher than 50%, a FWHM of 0.5–1 µm, an out-of-band rejection better than 10:1, and a pixel-to-pixel transmission peak wavelength variability of less than 4%. The work presented in this thesis and the key results achieved are summarized as follows:

Firstly, a detailed discussion of fundamental Fabry-Perot theory was presented, and the existing theory was used to guide the optical design of MEMS-based tunable LWIR Fabry-Perot filters presented in this thesis. A first-order Fabry-Perot cavity was identified as being the only suitable configuration for producing a wide free spectral range covering the entire LWIR spectral range of 8–12 µm and, therefore, was chosen as the cavity mode for the LWIR filters presented in this thesis. The LWIR mirror design criteria were developed, which indicated that both mirrors need to exhibit >75% reflectivity in order to achieve the targeted <1 µm spectral resolution, and that the difference in reflectivity between the two mirrors needs to be less than 20% in order to achieve the targeted >50% filter transmittance. The fundamental theory of quarter-wave mirrors was then briefly reviewed and applied to the LWIR quarter-wave mirror design based on the established criteria. The LWIR Fabry-Perot filter was ultimately designed to consist of a single-layer quarter-wavelength thick Ge top mirror and a four-layer quarter-wave Ge/ZnS/Ge/ZnS bottom mirror on a silicon substrate, with an additional single-layer quarter-wavelength thick ZnS on the backside of the substrate to serve as an anti-reflection coating. Transmission tuning spectra of the proposed LWIR Fabry-Perot filter were calculated using the optical matrix model, showing that this filter design can achieve a peak transmittance higher than 80%, a FWHM spectral width of approximately 500 nm, and an out-of-band rejection greater than 40:1 over the entire 8–12 µm wavelength range, all of which exceed the target specifications for multispectral thermal imaging applications. Based on the optical matrix model, an optical modelling approach for

calculating the transmittance of a Fabry-Perot filter with mirror imperfections was developed. Subsequently, this approach was employed to evaluate the on-pixel optical performance of the LWIR filter design in the presence of top mirror bowing, showing that while the filter can always achieve ideal on-pixel transmittance characteristics irrespective of mirror bowing, the maximum tolerable top mirror bowing amplitude is 300 nm in order to meet the <4% pixel-to-pixel transmission peak wavelength variation requirement.

Prior to discussion of filter fabrication, experimental preparation and optical and mechanical characterization of Ge and ZnS thin film mirror materials were presented. While electron-beam evaporated Ge films deposited at room temperature exhibited excellent durability under exposure to DI water and AZ400K developer, thermally-evaporated ZnS films deposited at room temperature delaminated immediately upon contact with these chemicals. Substrate temperature during film deposition was found to have a significant impact on the adhesion properties of ZnS layers, and it was shown that a film growth temperature higher than 150 °C is key to depositing durable ZnS films. An iterative least-squares approach was implemented to fit the optical matrix model to the experimentally measured transmittance spectra of Ge/ZnS multilayer structures in order to extract the optical constants of Ge and ZnS thin films, with the refractive indices of Ge and ZnS measured to be 4.0 and 2.2 with extinction coefficients of 2×10^{-5} and 2×10^{-3}, respectively. These results indicated that the electron-beam evaporated Ge and thermally-evaporated ZnS thin films were of high refractive index contrast and excellent LWIR transparency. For the characterization of thin film mechanical stress properties, the substrate curvature method was used to measure thin film residual mean stress, and this was complemented by the stress-induced deformation of diagnostic microcantilever structures to measure thin film stress gradients. Measurement revealed that the top mirror Ge film layer had a tensile stress of 110 MPa and a negative stress gradient of 210 MPa/μm in the film growth direction.

In terms of the experimental realization of LWIR filters, this thesis first presented the fabrication of a MEMS-based LWIR Fabry-Perot filter, whose MEMS structure was adapted from a mature Fabry-Perot filter technology previously demonstrated in the short-wavelength infrared (SWIR) region, consisting of a circular Ge top mirror suspended in the center of four doubly clamped beam actuators by flexible tethers. MEMS structural modifications required for extending the SWIR filter technology into the LWIR range were discussed, and key steps in the development of the fabrication process for LWIR filters were described, including the coating of a thick, large-area uniform sacrificial layer, a sacrificial layer dry etching procedure to

create gently sloping positive sidewalls for strong anchor support, and the deposition and stress characterization of ICPCVD SiN_x thin films, which were used to balance the stress gradients in the Ge top mirror for mirror bowing control. Subsequently, a comprehensive fabrication process flow for LWIR filters was presented, and the experimental procedure for the determination of the optimal thickness of the SiN_x stress-compensation layer was described. A 15 nm thick 150 MPa compressively stressed SiN_x layer was found to be optimal to achieve a nominally zero mirror curvature. Filters with 15 nm thick SiN_x stress-compensation layers were fabricated from different runs, and profilometry measurements indicated that significant top mirror bowing was still present in these filters and varied considerably from run to run due to uncontrolled variations in the deposition thicknesses and/or stress of the Ge top mirror layer and the SiN_x stress-compensation layer. Throughout this work, the smallest mirror bowing achieved after stress compensation was 550 nm across a 150-µm diameter mirror area, which was significantly less in comparison to the mirror bowing of 1.5 µm prior to stress compensation. The on-pixel optical performance of the filter showing the smallest mirror bowing of 550 nm was examined. Optical modelling showed that although this filter can achieve ideal on-pixel transmittance characteristics that exceed the target specifications for multispectral thermal imaging applications, namely a peak transmittance higher than 80%, a FWHM of approximately 500 nm, and an out-of-band rejection better than 40:1, it suffers from significant pixel-to-pixel transmission peak wavelength variation of 6.9% across the entire 150-µm diameter mirror area and the required <4% peak wavelength variability can only be achieved within the central 46% of the total optical filter area. Overall, these results led to the conclusion that MEMS LWIR Fabry-Perot filter designs based on a tether-supported top mirror are vulnerable to mirror layer stress gradients, which lead to uncontrollable mirror bowing due to run-to-run processing variations. As such, without significant additional effort, it would be difficult to fabricate filters with large-area optically flat mirrors, as required for multispectral imaging using FPAs.

This thesis then presented the demonstration of a MEMS-based LWIR Fabry-Perot filter with an improved structural design, which employs a self-supporting tensile-strained Ge membrane as both the top movable mirror and the MEMS actuator support. The complete fabrication process flow was described, and the mechanical and optical characterization of the fabricated filters of various membrane sizes were presented and compared. This filter design demonstrated strong robustness against stress-gradient induced mirror bowing and run-to-run processing variations, achieving nanometre-scale as-released mirror flatness across a large mirror area of

millimeter-scale dimensions without any additional stress management procedure. The fabricated filter with a 200-µm dimension mirror demonstrated less than 100 nm of top mirror bowing with actuation and exhibited close-to-design transmittance characteristics (including peak transmittance between 80–87%, FWHM of approximately 500 nm, and out-of-band rejection between 40:1–43.5:1) over the entire wavelength tuning range of 8.5–11.46 µm. Moreover, optical modelling showed that this filter can achieve a pixel-to-pixel transmission peak wavelength variation of less than 1.2% across the entire 200 µm × 200 µm optical mirror area. All these results exceed the target spectral specifications for multispectral thermal imaging applications. In comparison, the 500-µm and 1000-µm dimension filters developed significant top mirror bowing with actuation and, as a result, despite showing ideal on-pixel transmittance over the entire actuation range, have narrower usable spectral tuning ranges of 9.3-11.4 µm and 10.3-11.3 µm, respectively, for a <4% pixel-to-pixel transmission peak wavelength non-uniformity. Lastly, cryogenic cooling tests were conducted, and preliminary results were presented, indicating that the static filters can maintain excellent mirror flatness even after cooling to 77 K.

The content of this thesis is a substantial contribution to the subject of MEMS-based tunable LWIR Fabry-Perot filters, and the successful development of the prototype devices (membrane-based filters) in this thesis is a firm stepping stone for the future development of next-generation miniature multispectral thermal imaging systems based on a hybridized technology incorporating a large-area MEMS tunable LWIR Fabry-Perot filter and a cryogenically cooled 2-D LWIR imaging FPA.

7.2 Future work

As a proof-of-concept demonstration, the stretched-membrane based MEMS tunable LWIR Fabry-Perot filters presented in this thesis employed polyimide as the structural support for the suspended top mirror. Future research will need to proceed towards the realization of self-supported filter structures without incorporating polyimide, which will significantly improve the long-term reliability and overall integrity of the devices. In addition, an array of etch holes were included in the top mirror in order to facilitate the filter release process and, thus, prevent cracks forming in the Ge top mirror due to over-exposure to the O_2 release plasma. These etch holes are highly undesirable for imaging, and future work will need to be directed towards developing a wet release process in order to avoid the use of etch holes.

It has been shown that the MEMS-based LWIR Fabry-Perot filters demonstrated in this thesis had a high actuation voltage beyond 100 V. Since the hybrid integra-

tion approach allows filter and detector arrays to use separate voltage sources, the observed high actuation voltage level is indeed not a major concern. Nevertheless, minimizing actuation voltage is highly advantageous for filter operation, and therefore needs to be investigated as part of future research. There are many design parameters that can be engineered to reduce the actuation voltage, such as increasing the effective electrode area, reducing the mechanical stiffness and thickness of the MEMS actuators, and increasing the effective actuator length by increasing the distance between the mirror edge and the actuator pedestal/support structure.

Because state-of-the-art HgCdTe-based LWIR photodetector arrays need to be cooled to liquid nitrogen temperature for operation, filter performance at cryogenic temperatures is a key research topic that needs to be investigated. Preliminary cryogenic cooling tests were performed in this thesis, showing that the stretched-membrane based filters can maintain excellent top mirror flatness even after cooling to 77 K. However, at present, our cryogenic testing setup is not capable of measuring electrical actuation and optical transmission at 77 K. Thus, the optical tuning characterization of the cooled filters was not carried out as part of this thesis, and is deferred to future research. Another important task in future work is to improve mechanical strength of the Ge membrane material and to characterize MEMS structural robustness during periodic actuation both at room temperature and in cryogenic conditions in order to prevent any mechanical failure from occurring during device implementation. Moreover, we are currently investigating the mechanisms for minimizing suspended membrane bowing during actuation for the realization of multi-millimeter scale tunable filters for hybridizing with 2-D FPAs. Top mirror bowing during actuation is likely due to the electrical conductivity of Ge layers, which causes the entire Ge top membrane to be actuated and bend during actuation. This issue will be addressed by depositing electrical insulation layers between Au electrodes and Ge layers, which is a direction of future work.

In addition to all the aspects discussed above, there are many other considerations that need to be addressed in the realization of practical MEMS-based tunable LWIR Fabry-Perot filters, including filter transient behaviour and long-term stability of the filter characteristics. Detailed investigations into these research topics need to be the subject of future work. Non-MEMS work required for the full realization of a miniature multispectral thermal imaging system includes development of a filter/detector alignment and bonding process, miniaturization of actuation and sensing circuitry, and system vacuum packaging. Since the complete development of a multispectral thermal imaging system is beyond the scope of this thesis, these tasks also remain as future work to be undertaken.

Appendix A

Publications arising from this thesis

A.1 Journal articles

[1] **H. Mao**, K. K. M. B. D. Silva, M. Martyniuk, J. Antoszewski, J. Bumgarner, J. M. Dell, and L. Faraone, "Ge/ZnS-based micromachined Fabry-Perot filters for optical MEMS in the longwave infrared," *Journal of Microelectromechanical Systems*, vol. 24, no. 6, pp. 2109–2116, Dec. 2015.

[2] **H. Mao**, K. K. M. B. D. Silva, M. Martyniuk, J. Antoszewski, J. Bumgarner, B. D. Nener, J. M. Dell, and L. Faraone, "MEMS-based tunable Fabry-Perot filters for adaptive multispectral thermal imaging," *Journal of Microelectromechanical Systems*, vol. 25, no. 1, pp. 227–235, Feb. 2016.

[3] D. K. Tripathi, **H. Mao**, K. K. M. B. D. Silva, J. Bumgarner, M. Martyniuk, J. M. Dell, and L. Faraone, "Large-area MEMS-based distributed Bragg reflectors for short-wave and mid-wave infrared hyperspectral imaging applications," *Journal of Microelectromechanical Systems*, vol. 24, no. 6, pp. 2136–2144, Dec. 2015.

A.2 Conference proceedings

[1] D. K. Tripathi, **H. Mao**, K. K. M. B. D. Silva, and L. Faraone, "Compositional and mechanical properties of PECVD silicon for thin-film optical applications," in *Proceedings of 2012 IEEE Conference on Optoelectronic and Microelectronic Materials and Devices (COMMAD 2012)*, Melbourne, Australia, Dec. 2012, pp. 185–186.

[2] **H. Mao**, A. J. Keating, K. K. M. B. D. Silva, J. M. Dell, and L. Faraone, "Long-wavelength infrared Fabry-Perot etalon for multi-spectral thermal imaging," in *Proceedings of SPIE Micro/Nano Materials, Devices, and Systems*, Melbourne, Australia, Dec. 2013, vol. 8923, pp. 89234P: 1–6.

[3] **H. Mao**, M. Martyniuk, K. K. M. B. D. Silva, J. Antoszewski, J. Bumgarner, and L. Faraone, "Towards MEMS-based long-wavelength infrared tuneable Fabry-Perot filters," in *Proceedings of 2014 IEEE Conference on Optoelectronic and Microelectronic Materials and Devices (COMMAD 2014)*, Perth, Australia, Dec. 2014, pp. 149–152.

A.3 Conference presentations

[1] **H. Mao**, A. J. Keating, J. Antoszewski, M. Martyniuk, J. M. Dell, and L. Faraone, "Preliminary investigation on MEMS-based cooled long-wave infrared Fabry-Perot filters for multi-spectral imaging," presented at *the 10th Asia-Pacific Microscopy Conference (APMC-10), 2012 International Conference on Nanoscience and Nanotechnology (ICONN 2012), and 22nd Australian Conference on Microscopy and Microanalysis (ACMM-22)*, Perth, Australia, Feb. 2012.

[2] **H. Mao**, K. K. M. B. D. Silva, M. Martyniuk, J. Antoszewski, J. Bumgarner, and L. Faraone, "Towards longwave infrared tuneable filters for multispectral thermal imaging applications," presented at *the 12th International Conference on Quantitative InfraRed Thermography (QIRT 2014)*, Bordeaux, France, Jul. 2014.

[3] K. K. M. B. D. Silva, **H. Mao**, J. Antoszewski, M. Martyniuk, J. Bumgarner, J. M. Dell, and L. Faraone, "MEMS for multispectral imaging in the longwave infrared," presented at *the 2015 U.S. Workshop on the Physics and Chemistry of II-VI Materials*, Chicago, USA, Oct. 2015.

[4] **H. Mao**, M. Martyniuk, K. K. M. B. D. Silva, J. Antoszewski, J. Bumgarner, J. M. Dell, and L. Faraone, "MEMS-based tuneable longwave infrared Fabry-Perot filters for multispectral thermal imaging," presented at *the 2016 International Conference on Nanoscience and Nanotechnology (ICONN 2016)*, Canberra, Australia, Feb. 2016.

Appendix B

Fabrication process for diagnostic microstructures

In this work, microcantilevers were fabricated for the determination of stress gradients in electron-beam evaporated Ge mirror layers (see Section 4.3.2), while doubly clamped beams and ring-and-crossbeam structures were fabricated for determination of the mean compressive stress and mean tensile stress of the ICPCVD SiN_x stress-compensation layers, respectively (see Section 5.2.2). The microcantilevers had three lengths of 50 µm, 100 µm and 200 µm. All cantilevers were fabricated with a width of 10 µm and the Ge structural layers had a thickness of 606 nm. The doubly clamped beams had a length of 220 µm and a width of 50 µm, and the ring-and-crossbeam structures had a ring diameter of 220 µm and a beam width of 20 µm. The SiN_x thin films used for the construction of the doubly clamped beams and ring-and-crossbeam structures had a thickness of 50 nm.

The process for fabricating the diagnostic microstructures is presented in Figure B.1. An HD Microsystems product, PI2610 low stress polyimide, was chosen to serve as the sacrificial layer due to minimal stress introduced and its suitability for producing large-area uniform coatings. The polyimide was spun onto a silicon substrate at a spin speed of 1500 rpm for 40 seconds. Curing of the polyimide was performed according to the manufacturer-recommended process: firstly, the polyimide was soft-baked at 130 °C on a hotplate for 5 minutes in laboratory ambient; then the hotplate temperature was gradually increased to 300 °C and the polyimide was hard-baked at 300 °C for 30 minutes; finally, the polyimide along with the hotplate was gradually cooled down to ambient temperature. In order to create a sufficiently thick air gap between the freestanding microstructures and the substrate to prevent the buckled microstructures from contacting the substrate after release, the above spin coating procedure was repeated again, producing a final polyimide thickness of 7.6 µm. Subsequently, the polyimide sacrificial layer

was patterned in an O_2/CF_4 plasma to create step-down, gently sloping sidewalls required for strong and continuous anchor supports. Next, the structural layer was deposited and subsequently patterned photolithographically and selectively etched using an O_2/CF_4 plasma to create the diagnostic microstructures. The freestanding diagnostic microstructures were released by removing the polyimide sacrificial layer in an O_2 plasma.

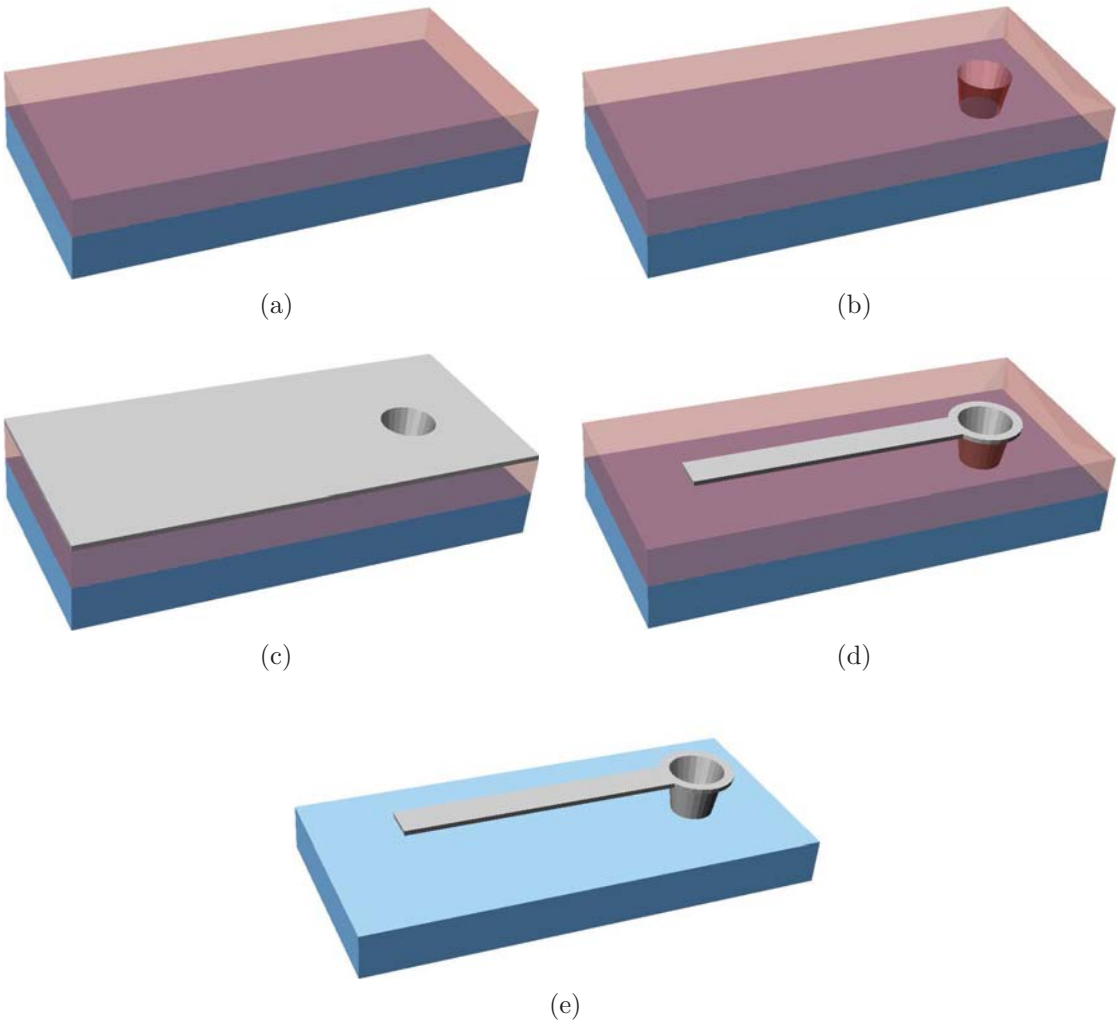

Figure B.1: The fabrication process for diagnostic microstructures. (a) Polyimide spin coating onto a silicon substrate to serve as the sacrificial layer. (b) Patterning of the polyimide layer in an O_2/CF_4 plasma to create the support anchors. (c) Structural layer deposition. (d) Patterning of the structural layer in an O_2/CF_4 plasma to the desired microstructure geometry. (e) Removal of the polyimide sacrificial layer in an O_2 plasma to produce the freestanding diagnostic microstructures.

References

[1] A. B. Kahle and A. F. H. Goetz, "Mineralogic information from a new airborne thermal infrared multispectral scanner," *Science*, vol. 222, no. 4619, pp. 24–27, Oct. 1983.

[2] R. G. Vaughan, S. J. Hook, W. M. Calvin, and J. V. Taranik, "Surface mineral mapping at Steamboat Springs, Nevada, USA, with multi-wavelength thermal infrared images," *Remote Sensing of Environment*, vol. 99, no. 1–2, pp. 140–158, Nov. 2005.

[3] M. J. Wabomba, Y. Sulub, and G. W. Small, "Remote detection of volatile organic compounds by passive multispectral infrared imaging measurements," *Applied Spectroscopy*, vol. 61, no. 4, pp. 349–358, Apr. 2007.

[4] L. Zhang and G. W. Small, "Automated detection of chemical vapors by pattern recognition analysis of passive multispectral infrared remote sensing imaging data," *Applied Spectroscopy*, vol. 56, no. 8, pp. 1082–1093, Feb. 2002.

[5] S. Teggi, M. P. Bogliolo, M. F. Buongiorno, S. Pugnaghi, and A. Sterni, "Evaluation of SiO_2 emission from Mount Etna using diurnal and nocturnal multispectral IR and visible imaging spectrometer thermal IR remote sensing images and radiative transfer models," *Journal of Geophysical Research: Solid Earth*, vol. 104, no. B9, pp. 20069–20079, Sep. 1999.

[6] W. B. Clodius, C. Borel, L. Balick, and S. J. Hook, "Validation of the MTI water surface temperature retrieval algorithms," in *Proceedings of 2002 IEEE International Geoscience and Remote Sensing Symposium (IGARSS'02)*, Toronto, Canada, Jun. 2002, vol. 1, pp. 30–32.

[7] A. P. Rodger, L. K. Balick, and W. B. Clodius, "The performance of the multispectral thermal imager (MTI) surface temperature retrieval algorithm at three sites," *IEEE Transaction on Geoscience and Remote Sensing*, vol. 43, no. 3, pp. 658–665, Mar. 2005.

[8] A. C. Goldberg, K. K. Choi, M. Jhabvala, A. La, P. N. Uppal, and M. L. Winn, "Large-format and multispectral QWIP infrared focal plane arrays," in *Proceedings of SPIE Infrared Technology and Applications XXIX*, Orlando, FL, Oct. 2003, vol. 5074, pp. 83–94.

[9] F. Vagni, "Survey of hyperspectral and multispectral imaging technologies," RTO NATO, Neuilly, France, Tech. Rep. TR-SET-065-P3, May 2007.

[10] J. L. Miller, "Weather and environmental monitoring sensors," in *Principles of Infrared Technology: A Practical Guide to the State of the Art*. New York: Van Nostrand Reinhold, 1994, ch. 12, p. 522.

[11] H. Xie and G. K. Fedder, "Integrated microelectromechanical gyroscopes," *Journal of Aerospace Engineering*, vol. 16, no. 2, pp. 65–75, Apr. 2003.

[12] D. S. Eddy and D. R. Sparks, "Application of MEMS technology in automotive sensors and actuators," *Proceedings of the IEEE*, vol. 86, no. 8, pp. 1747–1755, Aug. 1998.

[13] W. P. Eaton and J. H. Smith, "Micromachined pressure sensors: review and recent developments," *Smart Materials and Structures*, vol. 6, no. 5, pp. 530–539, 1997.

[14] J. Miao, R. Lin, L. Chen, Q. Zou, S. Y. Lim, and S. H. Seah, "Design considerations in micromachined silicon microphones," *Journal of Microelectronics*, vol. 33, no. 1–2, pp. 21–28, Jan. 2002.

[15] G. N. Nielson *et al.*, "High-speed, sub-pull-in voltage MEMS switching," Sandia National Laboratories, Albuquerque, New Mexico, Technical Report SAND2008-0211, Jan. 2008.

[16] R. R. A. Syms and D. F. Moore, "Optical MEMS for telecoms," *Materials Today*, vol. 5, no. 7-8, pp. 26–35, Aug. 2002.

[17] Vaisala Corporation. (2012). *Vaisala CARBOCAP sensor for measuring carbon dioxide* [online]. Available: http://www.vaisala.com/Vaisala%20Documents/Technology%20Descriptions/CEN-TIA-G-Carbocap-Technology-description-B210780EN-C.pdf

[18] R. A. Crocombe, "MEMS technology moves process spectroscopy into a new dimension," *Spectroscopy Europe*, vol. 16, no. 3, pp. 16–19, 2004.

[19] A. Rogalski, "Infrared detectors for the future," *Acta Physica Polonica A*, vol. 116, no. 3, pp. 389–406, 2009.

[20] M. Tuohiniemi, A. Nasila, and J. Makynen, "Characterization of the tuning performance of a micro-machined Fabry-Perot interferometer for thermal infrared," *Journal of Micromechanics and Microengineering*, vol. 23, no. 7, pp. 1–7, Jul. 2013.

[21] M. Tuohiniemi, M. Blomberg, A. Akujarvi, J. Antila, and H. Saari, "Optical transmission performance of a surface-micromachined Fabry-Perot interferometer for thermal infrared," *Journal of Micromechanics and Microengineering*, vol. 22, no. 11, pp. 1–7, Sep. 2012.

[22] P. A. Stupar, R. L. Borwick, J. F. DeNatale, P. H. Kobrin, and W. J. Gunning, "MEMS tunable Fabry-Perot filters with thick, two sided optical coatings," in *Proceedings of 15th IEEE International Conference on Solid-State Sensors, Actuators and Microsystems (TRANSDUCERS'09)*, Denver, CO, Jun. 2009, pp. 1357–1360.

[23] M. Ebermann, M. Meinig, S. Kurth, K. Hiller, E. Gittler, and N. Neumann, "Tiny mid- and long-wave infrared spectrometer module with a MEMS dual-band Fabry-Perot filter," in *Proceedings IRS^2 of Sensor+Test Conferences*, Nürnberg, Germany, Jun. 2011, pp. 94–99.

[24] N. Neumann, M. Ebermann, E. Gittler, M. Meinig, S. Kurth, and K. Hiller, "Uncooled IR sensors with tunable MEMS Fabry-Perot filters for the long-wave infrared range," in *Proceedings of 2010 IEEE Sensors Conference*, Kona, Hawaii, Nov. 2010, pp. 2383–2387.

[25] M. Meinig, M. Ebermann, N. Neumann, S. Kurth, K. Hiller, and T. Gessner, "Dual-band MEMS Fabry-Perot filter with two movable reflectors for mid- and long-wave infrared microspectrometers," in *Proceedings of 16th IEEE International Conference on Solid-State Sensors, Actuators and Microsystems (TRANSDUCERS'11)*, Beijing, China, Jun. 2011, pp. 2538–2541.

[26] H. A. Macleod, *Thin-film Optical Filters*, W. T. Welford, Ed., 3rd ed. Bristol and Philadelphia: Institute of Physics Publishing, 2001.

[27] P. D. Atherton, N. K. Reay, J. Ring, and T. R. Hicks, "Tunable Fabry-Perot filters," *Optical Engineering*, vol. 20, no. 6, pp. 806–814, Dec. 1981.

[28] E. Garmire, "Theory of quarter-wave-stack dielectric mirrors used in a thin Fabry-Perot filter," *Applied Optics*, vol. 42, no. 27, pp. 5442–5449, Sep. 2003.

[29] J. Vizgaitis. (2006, Dec. 14). *Selecting infrared optical materials* [online]. Available: http://fp.optics.arizona.edu/optomech/student%20reports/tutorials/VizgaitisTutorial1.doc

[30] J. M. Vaughan, "The plane Fabry-Perot interferometer," in *The Fabry-Perot Interferometer*, E. R. Pike and W. T. Welford, Eds. Bristol and Philadelphia: Adam Hilger, 1989, ch. 3, sec. 6, pp. 123–124.

[31] G. J. Sloggett, "Fringe broadening in Fabry-Perot interferometers," *Applied Optics*, vol. 23, no. 14, pp. 2427–2432, Jul. 1984.

[32] G. Hernandez, "Mathematical development," in *Fabry-Perot Interferometers*, P. L. Knight and S. D. Smith, Eds. Cambridge, UK: Cambridge University Press, 1986, ch. 2, sec. 3, pp. 23–24.

[33] A. J. Keating, K. K. M. B. D. Silva, J. M. Dell, C. A. Musca, and L. Faraone, "Optical characterization of FabryPerot MEMS filters integrated on tunable short-wave IR detectors," *IEEE Photonics Technology Letters*, vol. 18, no. 9, pp. 1079–1081, May 2006.

[34] J. S. Milne, "Micro-electromechanical technologies for next-generation spectroscopic systems," Ph.D. dissertation, School of Electrical, Electronic and Computer Engineering, The University of Western Australia, Perth, Australia, 2009.

[35] R. D. Mathis Company. *Baffled box sources for SiO and ZnS* [online]. Available: https://www.rdmathis.com/storev2/category.asp?cat=Baffled%20Box%20Sources%20for%20SiO,%20ZnS

[36] M. Zhou, D. Liu, T. Yu, and Q. Cai, "The optical properties of different temperature deposited ZnS film in visible to near-infrared region," in *Proceedings of 6th SPIE International Symposium on Advanced Optical Manufacturing and Testing Technologies*, Xiamen, China, Oct. 2012, vol. 8419, pp. 84192W: 1–5.

[37] M. Ashraf, S. M. J. Akhtar, Z. Ali, and A. Qayyum, "The influence of substrate temperature on the structural and optical properties of ZnS thin films," *Semiconductors*, vol. 45, no. 5, pp. 699–702, May 2011.

[38] H. C. Ong and R. P. H. Chang, "Optical constants of wurtzite ZnS thin films determined by spectroscopic ellipsometry," *Applied Physics Letters*, vol. 79, no. 22, pp. 3612–3614, Nov. 2001.

[39] E. Khawaja and S. G. Tomlin, "The optical constants of thin evaporated films of cadmium and zinc sulphides," *Journal of Physics D: Applied Physics*, vol. 8, no. 5, pp. 581–594, Apr. 1975.

[40] R. Swanepoel, "Determination of the thickness and optical constants of amorphous silicon," *Journal of Physics E: Scientific Instruments*, vol. 16, no. 12, pp. 1214–1222, Dec. 1983.

[41] W. S. Lau, "The measurement of oxygen and carbon and other impurities in silicon," in *Infrared Characterization for Microelectronics*. Singapore: World Scientific, 1999, ch. 3, pp. 25–30.

[42] R. F. Potter, "Germanium (Ge)," in *Handbook of Optical Constants of Solids*, vol. 1, E. D. Palik, Ed. Burlington: Elsevier, 2012, ch. 17, pp. 475–476.

[43] E. D. Palik and A. Addamiano, "Zinc sulfide (ZnS)," in *Handbook of Optical Constants of Solids*, vol. 1, E. D. Palik, Ed. Burlington: Elsevier, 2012, ch. 27, pp. 613–614.

[44] T. M. Donovan, W. E. Spicer, J. M. Bennett, and E. J. Ashley, "Optical properties of amorphous germanium films," *Physical Review B*, vol. 2, no. 2, pp. 397–413, Jul. 1970.

[45] J. F. Hall and W. F. C. Ferguson, "Optical properties of cadmium sulfide and zinc sulfide from 0.6 micron to 14 microns," *Journal of the Optical Society of America*, vol. 45, no. 9, pp. 714–717, Sep. 1955.

[46] G. G. Stoney, "The tension of metallic films deposited by electrolysis," *Proceedings of the Royal Society of London Series A-Containing Papers of a Mathematical and Physical Character*, vol. 82, no. 553, pp. 172–175, May 1909.

[47] J. M. Gere and S. P. Timoshenko, "Columns," in *Mechanics of Materials*, 2nd ed. Boston: PWS, 1985, ch. 11, sec. 3, pp. 560–566.

[48] H. Guckel, D. Burns, C. Rutigliano, E. Lovell, and B. Choi, "Diagnostic microstructures for the measurement of intrinsic strain in thin films," *Journal of Micromechanics and Microengineering*, vol. 2, no. 2, pp. 86–95, Apr. 1992.

[49] M. Martyniuk, "Low-temperature micro-opto-electro-mechanical technologies for temperature sensitive substrates," Ph.D. dissertation, School of Electrical, Electronic and Computer Engineering, The University of Western Australia, Perth, Australia, 2006.

[50] HD Microsystems. (2009, September). *Product bulletin PI-2600 series low stress applications* [online]. Available: http://fast.auburn.edu/wiki/images/1/15/PI2600datasheet.pdf

[51] J. S. Milne, A. J. Keating, J. M. Dell, and L. Faraone, "MEMS-based tunable Fabry-Perot filters on silicon substrates," in *Proceedings of 2008 IEEE Conference on Optoelectronic and Microelectronic Materials and Devices (COMMAD 2008)*, Sydney, Australia, Aug. 2008, pp. 174–180.

[52] J. S. Milne, J. M. Dell, A. J. Keating, and L. Faraone, "Widely tunable MEMS-based Fabry-Perot filter," *Journal of Microelectromechanical Systems*, vol. 18, no. 4, pp. 905–913, Jul. 2009.

[53] J. S. Milne, A. J. Keating, J. Antoszewski, J. M. Dell, C. A. Musca, and L. Faraone, "Extending the tuning range of SWIR microspectrometers," in *Proceedings of SPIE Infrared Technology and Applications XXXIII*, Orlando, FL, May 2007, vol. 6542, pp. 65420M: 1–11.

[54] *ProLIFT 100 Product Family Technical Data Sheet*, Brewer Science Incorporation, Rolla, MO, 2005.

[55] J. Vlassak. (2004). *Thin film mechanics* [online]. Available: http://www.mrsec.harvard.edu/education/ap298r2004/Vlassak%20AP298presentation.pdf

[56] E. S. Hung and S. D. Senturia, "Extending the travel range of analog-tuned electrostatic actuators," *Journal of Microelectromechanical Systems*, vol. 8, no. 4, pp. 497–505, Dec. 1999.

[57] Q. Zou, Z. Li, and L. Liu, "New methods for measuring mechanical properties of thin films in micromachining: beam pull-in voltage (V_{PI}) method and long beam deflection (LBD) method," *Sensors and Actuators A: Physical*, vol. 48, no. 2, pp. 137–143, May 1995.

[58] *Using Glass Compensated (GC) Objectives, Operating Manual OMP-0553A*, Zygo Corporation, Middlefield, CT, 2009.